Dynamics of Microfabricated Enzyme Electrodes

Thesis by
Muhammad Musab Jilani

In Partial Fulfillment of the Requirements for the
Degree of
Doctor of Philosophy

Caltech

CALIFORNIA INSTITUTE OF TECHNOLOGY
Pasadena, California

2026
Defended August 14 2025

ACKNOWLEDGEMENTS

I could not have undertaken this journey without the immense support and encouragement of my parents and my sister. Sending me to the other side of the world so that I could follow this dream was truly an act of love, without which none of this work would have been possible. I would like to thank Rita for her invaluable support and encouragement especially in the past few months during some of the most stressful parts of this journey. I would also like to thank Brandon, Mehmet, Rashied, and Tara for their support and encouragement.

I would like to thank Prof. Axel Scherer for this opportunity and express great appreciation for his ability to inspire optimism when the work is tough. Many thanks to Prof. Yu-Chong Tai for chairing my committee, to Prof. Wei Gao for his committee service, and to Dr. Peter Petillo for his committee service, research support, and invaluable advice.

I would like to thank the broader Scherer Group team for their hard work and dedication and for making my time with the lab group enjoyable. Samson Chen, Xiomara Madero, Dvin Adalian, Christin Ahlbrecht, Richard Smith, Geraldine Galindo, and Juan Cardenas, I have enjoyed working with all of you and thank you for your contributions to this project.

I would also like to acknowledge support from the Molecular Materials Research Center in the Beckman Institute at Caltech and The Kavli Nanoscience Institute at Caltech.

ABSTRACT

This work sets out to meet some of the demands created by advancements in glucose oxidase enzyme electrode fabrication techniques. The application of microfabrication techniques to enzyme electrodes has enabled not only greater control over enzyme geometry but also the possibility of monolithic low-power fully wireless implantable biosensors with sensor-on-CMOS construction. Such efforts must be guided by a strong grasp of the theory of diffusion-limited electrochemistry of the products of enzymatically catalyzed reactions. Low power requirements demand a full understanding of sensor turn-on transients and the reduced device size impacts diffusion phenomena and increases the importance of considerations such as oxygen recycling from the reaction at the working electrode. With analytical solutions to the nonlinear differential equations involved not forthcoming, there is a need for sophisticated simulation tools that build upon other efforts in the field and deliver novel capabilities. Such simulation tools must also be complemented by robust, convenient, reproducible, and ideally automated empirical measurement tools to enable the design-test-redesign iteration process to converge quickly to the desired outcomes.

This work presents the development of finite element simulations of enzyme electrodes incorporating full two-substrate enzyme kinetics, a dynamic simulation of the sensor environment, and a full treatment of oxygen recycling at the working electrode. While the simulations presented in this work are carried out with axisymmetric RZ meshes, they are ready for use with full 3D meshes. It additionally presents the development of an automated wafer-scale measurement system enabling the testing of up to twenty sensors in parallel, still on the wafer on which they were fabricated. We present this with the hope that the ability to attack the problem from both sides — better in silico simulation and faster and more controlled in vitro iteration — should assist in the development of new sensing technologies.

We also present selected results studied through the use of these tools, in particular the determination of the impact of enzyme geometry on sensor response. These results show the promise of thin-film deposition via spin-coating and vapor deposition crosslinking to enable the kind of fast response-time high-sensitivity electrodes that are needed for achieving monolithic wireless implantable biosensors.

TABLE OF CONTENTS

LIST OF ILLUSTRATIONS

LIST OF TABLES

Chapter 1

INTRODUCTION, BACKGROUND, AND RECENT ADVANCEMENTS

1.1 Global Burden of Diabetes and the Role of Continuous Glucose Monitoring

Diabetes mellitus (DM) represents one of the most pressing public-health challenges of the twenty-first century. The *International Diabetes Federation* Diabetes Atlas reports that 537 million adults (aged 20–79 years) were living with diabetes in 2021; this number is projected to rise to 783 million by 2045, an increase of 46% in just over two decades [1]. In the United States alone, the Centers for Disease Control and Prevention estimates that 38.4 million people — 11.6% of the population — live with diabetes, and a further 97.6 million adults have prediabetes [2].

Beyond its prevalence and economic cost, diabetes imposes substantial morbidity and mortality. Chronic hyperglycemia drives microvascular complications such as retinopathy, nephropathy, and neuropathy, alongside macrovascular disease that markedly elevates cardiovascular risk [3]. The Diabetes Control and Complications Trial (DCCT) in type 1 diabetes and the UK Prospective Diabetes Study (UKPDS) in type 2 established that intensive glycemic control confers lasting reductions in these complications [4, 3]. Achieving and maintaining normoglycemia, however, remains a continuous challenge.

Conventional self-monitoring of blood glucose (SMBG) relies on intermittent capillary measurements that provide only snapshot information. While SMBG is indispensable, its discrete nature can miss rapid glucose excursions and imposes a significant burden of finger-stick testing. Continuous glucose monitoring (CGM) overcomes these limitations by providing near-real-time data every 1–5 minutes, enabling dynamic assessment of glucose trends and variability[5]. Modern CGM systems fall into two broad categories: real-time CGM (rtCGM), which streams data continuously to a receiver or smartphone, and intermittently scanned CGM (isCGM), in which readings are obtained on demand by scanning a sensor patch [6].

A robust body of evidence demonstrates the clinical impact of CGM across diverse patient populations. Randomized controlled trials in type 1 diabetes have shown that rtCGM reduces hemoglobin A1c (HbA1c), increases time in range, and reduces the incidence of severe hypoglycemia [7, 6, 8]. Comparable benefits have been reported in insulin-treated type 2 diabetes [9] and in pregnancy [10].

Clinical guidelines now advocate CGM as standard of care for most individuals using intensive insulin therapy. The *American Diabetes Association* Standards of Medical Care in Diabetes (2025) recommend rtCGM or isCGM for all youths and adults on insulin therapy to improve glycemic outcomes and quality of life [11]. The European Association for the Study of Diabetes and other international bodies have issued concordant guidance [12].

The continued refinement of CGM technology is therefore a priority for both clinical and research communities. Advances in microfabrication, materials science, and computational modeling show great promise to address longstanding technical challenges, enable faster and cheaper iteration of designs, and give researchers greater control over short- and long-term sensor behavior. Coupled with complementary experimental approaches, finite element analysis (FEA) enables quantitative understanding of how micro-scale geometry and material properties influence macro-scale performance. The present dissertation builds upon this foundation, integrating finite-element models with wafer-scale empirical data to accelerate development of microfabricated continuous glucose sensors.

1.2 Advancements in Microfabricated Biosensors

Modern micro- and nanofabrication have transformed amperometric CGM devices from hand-assembled catheters into wafer-scale, highly integrated microsystems. Photolithography, thin-film deposition, and 3-D microstructuring now allow engineers to sculpt both the transducer and the biorecognition layer with micron-level precision, yielding faster, smaller, and more reproducible sensors.

Early glucose oxidase (GOx) layers were hand-dispensed gels that introduced large variability and slow diffusion. Photopatternable hydrogels now enable in situ immobilization of active enzyme exactly where electrochemical transduction occurs. Mugweru and co-workers photopolymerized PEG-diacrylate films containing GOx over gold microdisks on flexible polyimide using standard lift-off lithography, producing addressable arrays with linear response up to 20 mM glucose [13]. Yan et al. extended this strategy to multi-analyte chips by UV-crosslinking enzyme-containing PEG on gold arrays, demonstrating µm-scale feature control [14].

In previous work, we have described spin-coating a 500 nm GOx film across 4-inch wafers and using liftoff to define active regions directly above on-chip potentiostats;

the monolithic “sensor-on-CMOS” achieved sub-second stabilization and <5 % device-to-device variability in trasient response time [15]. Such advances bring closer the prospect of fully integrated monolithic wireless implants.

However, in addition to creating new possibilities, such developments also create new demands, namely for wafer-scale processing to be matched with wafer-scale testing, and for a more sophisticated theoretical and mathematical understanding of the underlying phenomena to enable rapid iteration and well-optimized design.

1.3 Theory of Operation, Modeling, and Simulation

The glucose sensors this work focuses on use the most common transduction modality: amperometric detection at an enzyme electrode. In this transduction method, an electrochemical sensor is coated with a layer (typically a hydrogel) containing glucose oxidase (GOx) enzyme. Glucose oxidase catalyzes the reaction of glucose with oxygen to form hydrogen peroxide and δ-gluconolactone. The hydrogen peroxide thus formed can then be amperometrically detected by the underlying electrochemical sensor. While this modality is conceptually simple and one of the most common transduction modalities in use [16], the design of sensors proceeding on it needs to incorporate a nuanced and multifaceted approach due to the complexity of the underlying phenomena.

It has been understood since the early days of enzyme electrodes that the development of mathematical models is a worthwhile endeavor not only due to the intellectual unsatisfactoriness of a purely phenomenological understanding but also due to the inefficiency of a trial-and-error approach to electrode design [17]. This need for accurate mathematical modeling is now greater than ever, given the possibilities opened up by the application of microfabrication techniques to enzyme electrodes. In particular, the possibility of monolithic fully wireless implantable sensors [15], with the possibility of employing energy harvesting [18] and intermittent operation to remove the need for wired power or a battery, requires a complete understanding of the phenomena involved not just at steady state but also in the transient.

The complex nature of glucose oxidase (and other oxidase enzyme) based biosensors has meant that simple analytical solutions have been elusive and the field has endeavored instead to producing increasingly sophisticated numerical solutions with the progress both of numerical methods and computational power over time. The phenomena to consider in such modeling include the enzyme kinetics, which involve two substrates and are nonlinear in each [19, 20, 21]. In order for the sensor to function, the two analytes involved — glucose and oxygen — must enter the biosensor stack at its outer boundary and diffuse through the immobilized enzyme, where their enzymatically catalyzed reaction must take place. If the sensor functions on the detection of one of the reaction products, such as amperometric detection of hydrogen peroxide, this product must then continue on diffusing and make its way to the final transduction element. The nonlinear two-variable enzyme kinetics and the transport of species interact in the diffusion-reaction equation:

$$D_i \nabla^2 c_i + R_i = \frac{\partial c_i}{\partial t} \tag{1.1}$$

Here D_i is the diffusivity of species i, c_i its concentration, R_i its reaction rate, and t is time. The nonlinearity of the reaction term R due to the nonlinear enzyme kinetics has meant that this equation has remained intractable to analytical solution.

There's additionally the complication that the sensor does not leave the environment unperturbed. The consumption of glucose and oxygen by the immobilized enzyme naturally creates a diffusion gradient in the sensor environment, whose depth and gradient of course depend on the properties of the environment itself, as well as the change in diffusivity and partitioning [22] between the sensor and environment.

In the case of amperometric sensors based on detecting hydrogen peroxide, there is the additional consideration that detection of hydrogen peroxide produces oxygen [23], which is one of the analytes of glucose oxidase. This oxygen is free to diffuse back into the immobilized enzyme matrix, complicating the boundary condition that must exist on the interface between the enzyme and the sensing electrode. We would also expect the reaction products to diffuse not only towards the transducer but also outwards towards the sensor environment, meaning that the assumption of zero concentration at the outer boundary would also only be a simplification.

$$H_2O_2 + 2Pt(OH) \longrightarrow O_2 + 2Pt + 2H_2O \tag{1.2}$$

$$2H_2O_2 + 2Pt \longrightarrow 2H^+ + 2Pt(OH) + 2e^- \tag{1.3}$$

Mell & Maloy provided one-dimensional steady-state and transient analyses using explicit finite difference methods [24, 25], using a simplified one-substrate version of glucose oxidase's ping-pong kinetics. Although performed in one dimension, with simplified enzyme kinetics, and with a simplified treatment of the enzyme environment, their seminal work provided an illustrative view of the dynamics of enzyme electrodes. In the decades since then, many analyses have been published, with varying levels of sophistication and different balances struck between model simplicity and fidelity, and computational efficiency and versatility. Parker and Schwartz provided a detailed one-dimensional analysis of the steady-state concentration profiles that develop in the enzyme-containing hydrogel layer [26], with a detailed treatment of glucose oxidase's kinetics but using simplifying assumptions about the sensor environment and without consideration of oxygen recycling. They correctly criticize the application of single-substrate Michaelis-Menten kinetics to glucose sensors due to the requisite assumptions rarely holding in practical applications. Further work studied specific geometries [27, 28], the impact of enzyme concentration [29], and applications to sensors with oxygen-consuming transducers [30].

Recent work has been relatively sparse [31] and much that has been published has regressed to a single-substrate Michaelis-Menten kinetics treatment of enzyme kinetics [32, 33, 34, 35]. However there has been some work incorporating the full reaction mechanism, including modeling the diffusion of intermediate species, and providing steady-state and transient solutions [36, 31, 37]. Although carried out in one dimension and making some simplifying assumptions (such as fixed diffusion thickness) about the environment, it provides a sophisticated simulation of immobilized glucose oxidase.

Although one-dimensional analyses are very informative, the possibility now of patterning enzyme layers precisely using lithographic techniques [38, 15] leaves one-dimensional analysis wanting. There is a gap in the field of a sophisticated 3D or pseudo-3D (by way of axisymmetric meshing) simulation that incorporates:

- Two-substrate enzyme kinetics of glucose oxidase
- The interaction of the sensor and the environment, such as the growing diffusion layer, diffusion of reaction product into the environment, and solute partitioning and hindered diffusion betwen environment and sensor
- The impact of oxygen recycling from the enzyme substrate through consumption of hydrogen peroxide at the working electrode
- Enough spatial degrees of freedom to simulate and iterate through different possible microfabricated enzyme geometries

- The transient dynamics upon sensor turn-on or changes to environment analyte concentration

We offer an advancement in this field by creating an axisymmetric RZ simulation, with easy expansion to full 3D geometry (by changing the mesh to a full 3D one), which models two-substrate enzyme kinetics, considers the role of oxygen recycling at the working electrode, implements two parameters for modeling hindered analyte transport in hdyrogels (one corresponding to solute partitioning and one to hindered diffusion), and treats the bulk solution as a dynamically changing environment, impacted by and impacting the biosensor, rather than a static environment characterized either by fixed concentration or a fixed diffusion layer.

The decision only to use axisymmetric meshing at this juncture is entirely due to consideration of computational cost and the desire to make the design iteration process tractable on an enthusiast-class personal computer and avoid the need for expensive computational hardware or rented server time.

References

[1] Dianna J. Magliano, Edward J. Boyko, and IDF Diabetes Atlas 10th edition scientific committee. *IDF DIABETES ATLAS*. 10th ed. IDF Diabetes Atlas. Brussels: International Diabetes Federation, 2021. ISBN: 978-2-930229-98-0. PMID: `35914061`.

[2] CDC. *National Diabetes Statistics Report*. Diabetes. July 23, 2024. URL: `https://www.cdc.gov/diabetes/php/data-research/index.html` (visited on 08/06/2025).

[3] "Intensive Blood-Glucose Control with Sulphonylureas or Insulin Compared with Conventional Treatment and Risk of Complications in Patients with Type 2 Diabetes (UKPDS 33). UK Prospective Diabetes Study (UKPDS) Group". In: *Lancet (London, England)* 352.9131 (Sept. 12, 1998), pp. 837–853. ISSN: 0140-6736. PMID: `9742976`.

[4] Diabetes Control and Complications Trial Research Group et al. "The Effect of Intensive Treatment of Diabetes on the Development and Progression of Long-Term Complications in Insulin-Dependent Diabetes Mellitus". In: *The New England Journal of Medicine* 329.14 (Sept. 30, 1993), pp. 977–986. ISSN: 0028-4793. DOI: `10.1056/NEJM199309303291401`. PMID: `8366922`.

[5] David C. Klonoff, David Ahn, and Andjela Drincic. "Continuous Glucose Monitoring: A Review of the Technology and Clinical Use". In: *Diabetes Research and Clinical Practice* 133 (Nov. 1, 2017), pp. 178–192. ISSN: 0168-8227, 1872-8227. DOI: `10.1016/j.diabres.2017.08.005`. PMID: `28965029`.

[6] Tadej Battelino et al. “Clinical Targets for Continuous Glucose Monitoring Data Interpretation: Recommendations From the International Consensus on Time in Range”. In: *Diabetes Care* 42.8 (Aug. 2019), pp. 1593–1603. ISSN: 1935-5548. DOI: `10.2337/dci19-0028`. PMID: `31177185`.

[7] Roy W. Beck et al. “Effect of Continuous Glucose Monitoring on Glycemic Control in Adults With Type 1 Diabetes Using Insulin Injections: The DIAMOND Randomized Clinical Trial”. In: *JAMA* 317.4 (Jan. 24, 2017), pp. 371–378. ISSN: 0098-7484. DOI: `10.1001/jama.2016.19975`.

[8] I. Dicembrini et al. “Effects of Real-Time Continuous Glucose Monitoring in Type 1 Diabetes: A Meta-Analysis of Randomized Controlled Trials”. In: *Acta Diabetologica* 58.4 (Apr. 2021), pp. 401–410. ISSN: 1432-5233. DOI: `10.1007/s00592-020-01589-3`. PMID: `32789691`.

[9] R. A. Ajjan, S. Seidu, and J. P. Riveline. “Perspective of Continuous Glucose Monitoring-Based Interventions at the Various Stages of Type 2 Diabetes”. In: *Diabetes Therapy* 15.8 (Aug. 2024), pp. 1657–1672. ISSN: 1869-6953. DOI: `10.1007/s13300-024-01607-5`. PMID: `38907936`.

[10] Eleanor M. Scott et al. “Continuous Glucose Monitoring in Pregnancy: Importance of Analyzing Temporal Profiles to Understand Clinical Outcomes”. In: *Diabetes Care* 43.6 (June 2020), pp. 1178–1184. ISSN: 0149-5992. DOI: `10.2337/dc19-2527`. PMID: `32209645`.

[11] American Diabetes Association Professional Practice Committee. “7. Diabetes Technology: Standards of Care in Diabetes—2025”. In: *Diabetes Care* 48 (Supplement_1 Dec. 9, 2024), S146–S166. ISSN: 0149-5992. DOI: `10.2337/dc25-S007`.

[12] Richard I.G. Holt et al. “The Management of Type 1 Diabetes in Adults. A Consensus Report by the American Diabetes Association (ADA) and the European Association for the Study of Diabetes (EASD)”. In: *Diabetes Care* 44.11 (Oct. 18, 2021), pp. 2589–2625. ISSN: 0149-5992. DOI: `10.2337/dci21-0043`.

[13] Amos Mugweru, Becky L. Clark, and Michael V. Pishko. “Electrochemical Redundant Microsensor Arrays for Glucose Monitoring with Patterned Polymer Films”. In: *Electroanalysis* 19.4 (2007), pp. 453–458. ISSN: 1521-4109. DOI: `10.1002/elan.200603749`.

[14] Jun Yan et al. “Immobilizing Enzymes onto Electrode Arrays by Hydrogel Photolithography to Fabricate Multi-Analyte Electrochemical Biosensors”. In: *ACS applied materials & interfaces* 2.3 (Mar. 24, 2010), pp. 748–755. ISSN: 1944-8244. DOI: `10.1021/am9007819`. PMID: `20356276`.

[15] Dvin Adalian et al. “Patterned Thin Film Enzyme Electrodes via Spincoating and Glutaraldehyde Vapor Crosslinking: Towards Scalable Fabrication of Integrated Sensor-on-CMOS Devices”. In: *Lab on a Chip* 24.17 (2024), pp. 4172–4181. ISSN: 1473-0197, 1473-0189. DOI: `10.1039/D4LC00206G`.

[16] S. Vigneshvar et al. “Recent Advances in Biosensor Technology for Potential Applications – An Overview”. In: *Frontiers in Bioengineering and Biotechnology* 4 (Feb. 16, 2016), p. 11. ISSN: 2296-4185. DOI: `10.3389/fbioe.2016.00011`. PMID: `26909346`.

[17] P.N. Bartlett and K.F.E. Pratt. “Modelling of Processes in Enzyme Electrodes”. In: *Biosensors and Bioelectronics* 8.9 (1993), pp. 451–462. ISSN: 0956-5663. DOI: `10.1016/0956-5663(93)80030-S`.

[18] Arian Hashemi Talkhooncheh et al. “A Biofuel-Cell-Based Energy Harvester With 86% Peak Efficiency and 0.25-V Minimum Input Voltage Using Source-Adaptive MPPT”. In: *IEEE Journal of Solid-State Circuits* 56.3 (Mar. 2021), pp. 715–728. ISSN: 0018-9200, 1558-173X. DOI: `10.1109/JSSC.2020.3035491`.

[19] Quentin H. Gibson, Bennett E.P. Swoboda, and Vincent Massey. “Kinetics and Mechanism of Action of Glucose Oxidase”. In: *Journal of Biological Chemistry* 239.11 (Nov. 1964), pp. 3927–3934. ISSN: 00219258. DOI: `10.1016/S0021-9258(18)91224-X`.

[20] Takao Nakamura and Ogura Yasuyuki. “Kinetic Studies on the Action of Glucose Oxidase”. In: *The Journal of Biochemistry* 52.3 (Sept. 1962), pp. 214–220. ISSN: 1756-2651, 0021-924X. DOI: `10.1093/oxfordjournals.jbchem.a127599`.

[21] Michael K. Weibel and Harold J. Bright. “The Glucose Oxidase Mechanism”. In: *Journal of Biological Chemistry* 246.9 (May 1971), pp. 2734–2744. ISSN: 0021-9258. DOI: `10.1016/s0021-9258(18)62246-x`.

[22] David Ezra Liu. “Solute Partitioning and Hindered Diffusion in Hydrogels”. UC Berkeley, 2016.

[23] Ioannis Katsounaros et al. “Hydrogen Peroxide Electrochemistry on Platinum: Towards Understanding the Oxygen Reduction Reaction Mechanism”. In: *Physical Chemistry Chemical Physics* 14.20 (May 2, 2012), pp. 7384–7391. ISSN: 1463-9084. DOI: `10.1039/C2CP40616K`.

[24] Leroy D. Mell and J. T. Maloy. “Model for the Amperometric Enzyme Electrode Obtained through Digital Simulation and Applied to the Immobilized Glucose Oxidase System”. In: *Analytical Chemistry* 47.2 (Feb. 1, 1975), pp. 299–307. ISSN: 0003-2700, 1520-6882. DOI: `10.1021/ac60352a006`.

[25] Leroy D. Mell and J. T. Maloy. “Amperometric Response Enhancement of the Immobilized Glucose Oxidase Enzyme Electrode”. In: *Analytical Chemistry* 48.11 (Sept. 1, 1976), pp. 1597–1601. ISSN: 0003-2700, 1520-6882. DOI: `10.1021/ac50005a045`.

[26] J. W. Parker and C. S. Schwartz. “Modeling the Kinetics of Immobilized Glucose Oxidase”. In: *Biotechnology and Bioengineering* 30.6 (Oct. 20, 1987), pp. 724–735. ISSN: 0006-3592, 1097-0290. DOI: `10.1002/bit.260300605`.

[27] Paulami Majumdar, Anees Y. Khan, and Rajdip Bandyopadhyaya. “Diffusion, Adsorption and Reaction of Glucose in Glucose Oxidase Enzyme Immobilized Mesoporous Silica (SBA-15) Particles: Experiments and Modeling”. In: *Biochemical Engineering Journal* 105 (Jan. 2016), pp. 489–496. ISSN: 1369-703X. DOI: `10.1016/j.bej.2015.10.011`.

[28] Joseph Y. Lucisano and David A. Gough. “Transient Response of the Two-Dimensional Glucose Sensor”. In: *Analytical Chemistry* 60.13 (July 1, 1988), pp. 1272–1281. ISSN: 0003-2700, 1520-6882. DOI: `10.1021/ac00164a007`.

[29] Naoto Sakamoto. “Effect of Enzyme Concentration on the Dynamic Behavior of a Membrane-Bound Enzyme System”. In: *Journal of Membrane Science* 70.2–3 (June 1992), pp. 237–247. ISSN: 03767388. DOI: `10.1016/0376-7388(92)80109-W`.

[30] Pius H. S. Tse and David A. Gough. “Transient Response of an Enzyme Electrode Sensor for Glucose”. In: *Analytical Chemistry* 59.19 (Oct. 1, 1987), pp. 2339–2344. ISSN: 0003-2700, 1520-6882. DOI: `10.1021/ac00146a006`.

[31] Ming Gao and Mark E. Orazem. “The Development of Advanced Mathematical Models for Continuous Glucose Sensors”. In: *Electrochimica Acta* 382 (June 2021), p. 138226. ISSN: 00134686. DOI: `10.1016/j.electacta.2021.138226`.

[32] Naveed Ahmad Khan et al. “Mathematical Analysis of Reaction–Diffusion Equations Modeling the Michaelis–Menten Kinetics in a Micro-Disk Biosensor”. In: *Molecules* 26.23 (Dec. 2, 2021), p. 7310. ISSN: 1420-3049. DOI: `10.3390/molecules26237310`.

[33] M. Lilly Clarance Mary et al. “Mathematical Modeling of Immobilized Enzyme in Porous Planar, Cylindrical, and Spherical Particle: A Reliable Semi-Analytical Approach”. In: *Reaction Kinetics, Mechanisms and Catalysis* 134.2 (Dec. 2021), pp. 641–651. ISSN: 1878-5190, 1878-5204. DOI: `10.1007/s11144-021-02088-4`.

[34] Marco Fratus et al. “Geometry-Defined Response Time and Sensitivity for Microneedle-Based Amperometric Sensors”. In: *IEEE Sensors Journal* 23.13 (July 2023), pp. 14285–14294. ISSN: 1558-1748. DOI: `10.1109/JSEN.2023.3277425`.

[35] Seyed Mohsen Hashem Zadeh et al. “Numerical Modeling and Investigation of Amperometric Biosensors with Perforated Membranes”. In: *Sensors* 20.10 (10 Jan. 2020), p. 2910. ISSN: 1424-8220. DOI: `10.3390/s20102910`.

[36] Samuel Jacobs. “A MATHEMATICAL MODEL FOR THE TRANSIENT ELECTROCHEMICAL RESPONSE OF A CONTINUOUS GLUCOSE SENSOR”. University of Florida, 2022.

[37] Ming Gao. “A MATHEMATICAL MODEL FOR THE ELECTROCHEMICAL IMPEDANCE RESPONSE OF A CONTINUOUS GLUCOSE SENSOR”. University of Florida, 2020.

[38] Dvin Artashes-Boghos Adalian. “Development and Dynamics of Microfabricated Enzymatic Biosensors”. PhD thesis. California Institute of Technology, 2019. DOI: `10.7907/7GHS-NX49`.

Chapter 2

AXISYMMETRIC FINITE ELEMENT ANALYSIS

2.1 Overview

The application of semiconductor fabrication techniques to enzyme electrode fabrication has not enabled the fabrication of novel enzyme geometries, including the ability not only to develop sub-micron enzyme-containing hydrogels but also to pattern them lithographically [1, 2]. We believe it's essential for the theoretical understanding of sensor behavior to keep pace with these fabrication possibilities to inform and govern design decisions in the engineering of enzyme electrodes. It is especially important to understand not only the steady state but also the transient behavior of such electrodes if low energy-per-measurement devices are to be possible. This is likely a necessity for any miniaturized wireless battery-less implantable device, whether powered wirelessly from outside the body or through energy harvesting within the body. In vivo energy harvesting schemes can yield μW-range power output [3] and devices utilizing them would likely benefit from periodic measurements that don't necessitate keeping the sensor continuously on. Here, it is necessary to distinguish between two types of transient analysis – one that looks at the transient when the bulk glucose concentration is changed, and one that looks at the transient after the sensor is turned on. For designing low energy-per-measurement devices, we are most concerned with understanding the transient upon sensor turn-on, as understanding that is what would enable making short-duration low-energy measurements.

The behavior of our sensors, and enzyme electrodes more broadly, is governed by myriad complex phenomena including the diffusion of the substrates (glucose and oxygen) and the sensed product (hydrogen peroxide), nonlinear enzyme kinetics [4, 5, 6], sensor and enzyme geometry, and the partition of concentrations between the sensor environment and the enzyme layer [7]. In the case of glucose oxidase (and other oxidase enzymes for amperometric measurement), matters are further complicated by the production of oxygen at the electrode due to the consumption of hydrogen peroxide [8], which must be accommodated in any full theoretical model of the system.

In this chapter, we develop a finite element simulation to enable a systematic theoretical study of different sensor geometries and pull at each of these threads to see the impact it has on the dynamic sensor performance. The simulation developed has broader application than glucose sensors. At the very least, it can model other planar oxidase enzyme-based amperometric sensors by tweaking the input parameters to match the kinetics of a different enzyme. Diffusivity and partition coefficients for the enzyme-containing hydrogel are also tunable parameters.

2.2 System Description

The full system simulated consists of the sensor environment (measurement cell in vitro or interstitial fluid in vivo), which contains glucose and oxygen. Glucose and oxygen diffuse into the immobilized enzyme matrix, where they are catalytically converted to gluconolactone and hydrogen peroxide [4, 6, 5, 9]. This hydrogen peroxide diffuses through the enzyme matrix both towards the sensor surface and towards the sensor environment. The hydrogen peroxide may be consumed in the environment, depending on the nature of the environment being considered. When the sensor is turned on, it consumes the hydrogen peroxide at its surface, depleting it and setting up a concentration gradient reaching into the enzyme and potentially the sensor environment. Additionally, the sensor also produces oxygen while active [8], which diffuses back into the enzyme matrix, affecting the local rates of glucose consumption and hydrogen peroxide production.

2.3 Enzyme Kinetics

Single-Substrate Model

Much recent work [10, 11, 12, 13] uses the single-substrate Michaelis-Menten kinetics description for glucose oxidase, which proceeds from the following simplified reaction scheme:

$$E + S \underset{k_2}{\overset{k_1}{\longleftrightarrow}} ES \xrightarrow{k_3} P \tag{2.1}$$

Here, E is the enzyme, S is the (sugar) substrate, ES is the enzyme-substrate complex, and P is the product. This leads to the following description of enzyme kinetics:

$$V = V_{max} \frac{[S]}{[S] + K_m} \tag{2.2}$$

Here V is the reaction rate, V_{max} is the maximum reaction rate, and K_m is the (effective) Michaelis constant. The single-substrate Michaelis-Menten model is only an approximation of the ping-ping kinetics of glucose oxidase, reliant on a spatially and temporally fixed and known (or excell) oxygen concentration [9]. The value of K_m is often reported without an account of the oxygen concentration at all, limiting the value of such data. Additionally, we wish to include in our analysis the impact, if any, of oxygen recycling at the working electrode, which would be ignored by the single-substrate simplification. Therefore, we reject this in favor of using a more complete two-substrate descriptions of the reaction scheme and enzyme kinetics.

Two-Substrate Model

Gibson et al. determined the general two-substrate mechanism for glucose oxidase to be as follows [4] (reverse reactions are ignored as their rate constants are effectively zero when the oxidizer is oxygen) [14]:

$$\begin{aligned} E_O + G &\xrightarrow{k_1} E_R\text{-}P_1 \xrightarrow{k_2} E_R + \delta\text{-lactone} \\ E_R + O_2 &\xrightarrow{k_3} E_O - P_2 \xrightarrow{k_4} E_O + H_2O_2 \end{aligned} \tag{2.3}$$

This gives us the velocity equation [4, 9]:

$$\frac{1}{v} = \frac{k_2 + k_4}{k_2 k_4} + \frac{1}{k_1 c_g} + \frac{1}{k_3 c_{O_2}} \tag{2.4}$$

Leading naturally to the definition of kinetic parameters:

$$v_{max} = \frac{k_2 k_4}{k_2 + k_4} \tag{2.5}$$

$$K_G = \frac{v_{max}}{k_1} \tag{2.6}$$

$$K_{O_2} = \frac{v_{max}}{k_3} \tag{2.7}$$

And the following two-substrate Michaelis-Menten kinetics equation:

$$V = V_{max} \frac{[G][O_2]}{K_{O_2}[G] + K_G[O_2] + [G][O_2]} \tag{2.8}$$

where:

$$V_{max} = [E]v_{max} \tag{2.9}$$

Gibson et al. determined the kinetic parameters $K_G = 110\,mM$ and $K_{O_2} = 0.48\,mM$ at 27°C and pH 5.6 [4]. These parameters are strongly dependent on pH [6], but for the example simulation we use them as-is. While K_G and K_{O_2} are wholly determined by the enzyme kinetic constants, V_{max} is additionally dependent on (live) enzyme concentration (equation 2.9). The concentration of live enzyme in the final crosslinked and wetted matrix depends on a variety of factors including enzyme loss during the fabrication process due to leaching and inactivation, change in layer volume due to crosslinking, and degree of swelling upon wetting. Therefore in general it is difficult to estimate the density of live enzyme remaining post-immobilization and wetting. Glucose oxidase from Aspergillus niger is typically sold with some specification of specific activity although unit definitions can vary across suppliers (e.g. due to measurement at different pH by different suppliers). Enzyme stocked in our lab (BBI Solutions #GO3A) has typical activity around 285 units per mg, specified at pH 7.0. At a hypothetical live enzyme concentration of 2 gL^{-1} after accounting for loss and inactivation during fabrication and exposure to solvents, this converts to $V_{max} \approx 10\ mMs^{-1}$, which we use for our illustrative example simulation.

Parameter	Description	Value
V_{max}	Maximum enzymatic reaction rate per unit volume	$10\,mMs^{-1}$
K_G	Michaelis constant with respect to glucose	$110\,mM$
K_{O_2}	Michaelis constant with respect to oxygen	$480\,\mu M$

Table 2.1: Enzyme kinetic parameters for the example simulation.

2.4 Mass Transport

The fundamental equation governing mass transport in our system is the well-known diffusion-reaction equation:

$$D_i\nabla^2 c_i + R_i = \frac{\partial c_i}{\partial t} \tag{2.10}$$

where c_i is the concentration of species i, D_i is its diffusivity, R_i represents its rate of production (negative if consumption) per unit volume, and t is time.

In bulk solution, we use the reported values for the diffusivity of each species in water, specifically $D_{H_2O_2} = 1.43 \times 10^{-9}\ m^2s^{-1}$, $D_{O_2} = 1.93 \times 10^{-9}\ m^2s^{-1}$, and $D_{glucose} = 7.20 \times 10^{-10}\ m^2s^{-1}$ [15].

In hydrogel, two additional phenomena are at play: solute partitioning and hindered diffusion [7]. In the absence of specific interactions between a solute and the hydrogel polymer matrix, ideal point solutes are partitioned in proportion to the volume water fraction of the hydrogel whereas larger solutes are subject to size exclusion. Hindered diffusivity is owed to interactions between the solute and the polymer matrix, including physical obstruction and increased hydrodynamic resistance.

We define α_i to be the partitioning coefficient for solute i and β_i to be a penalty coefficient applied to the diffusivity in free solution to obtain diffusivity in the hydrogel:

$$\alpha_i = \frac{\text{concentration in hydrogel}}{\text{concentration in solution}} \tag{2.11}$$

$$\beta_i = \frac{\text{diffusivity in hydrogel}}{\text{diffusivity in solution}} \tag{2.12}$$

Empirical measurements of partition and diffusivity coefficients depend on the specific hydrogel used. Stroe-Biezen et al. [15] studied essentially the product $\alpha_i \cdot \beta_i$ by our definitions. In each hydrogel they studied, they found the "effective diffusivity" (incorporating the combined mass transport hindrance of solute partitioning and hindered diffusion) to be reduced relative to diffusivity in free solution by the same factor for oxygen and hydrogen peroxide, and by a greater factor for glucose. They found values between 0.19 and 0.40 for oxygen and hydrogen peroxide, and between 0.062 and 0.086 for glucose, in different polyvinyl alchohol hydrogels. Raja et al. estimated glucose diffusivity $\sim 10^{-11}\ m^2s^{-1}$ in albumin hydrogel [16]. Krupa et al. found glucose diffusivity in the range of $2.0 \times 10^{-10}\ m^2s^{-1}$ in silica hydrogels [17]. Benavidez and Baruzzi found the total glucose permeability of mucin/chitosan hydrogels could be varied by changing the mucin-chitosan ratio [18]. Figueiredo et al. found that the diffusivity of oxygen could be varied from $3.4 \times 10^{-10}\ m^2s^{-1}$ to $2.4 \times 10^{-10}\ m^2s^{-1}$ by changing the polymer concentration in silated-hydroxypropylmethylcellulose hydrogels [19].

Since these are parameters that can be engineered by appropriate choice of hydrogel, their choice is somewhat arbitrary. The simulation leaves all of them as tunable parameters and for the example simulation we use $\alpha = 0.2$ for all three species, $\beta_{H_2O_2} = \beta_{O_2} = 1.0$, and $\beta_{Glucose} = 0.3$. These values maintain the relative relationship between the effective diffusivity coefficients of H_2O_2, O_2, and glucose measured by Stroe-Biezen et al.

Parameter	Description	Value
D_G	Glucose diffusivity in water	$7.20 \times 10^{-10}\ m^2 s^{-1}$
D_{O_2}	Oxygen diffusivity in water	$1.93 \times 10^{-9}\ m^2 s^{-1}$
$D_{H_2O_2}$	Hydrogen peroxide diffusivity in water	$1.43 \times 10^{-9}\ m^2 s^{-1}$
$\alpha_{H_2O_2}$	Partition coefficient for H_2O_2	0.2
α_{O_2}	Partition coefficient for O_2	0.2
$\alpha_{Glucose}$	Partition coefficient for glucose	0.2
$\beta_{H_2O_2}$	Relative diffusion coefficient for H_2O_2	1.0
β_{O_2}	Relative diffusion coefficient for O_2	1.0
$\beta_{Glucose}$	Relative diffusion coefficient for glucose	0.3

Table 2.2: Mass transport parameters for the example simulation.

2.5 Sensor Dynamics

We expect the following two-step process at the sensing electrode:

$$H_2O_2 + 2Pt(OH) \longrightarrow O_2 + 2Pt + 2H_2O \tag{2.13}$$

$$2H_2O_2 + 2Pt \longrightarrow 2H^+ + 2Pt(OH) + 2e^- \tag{2.14}$$

This chemical-electrochemical reaction overall results in the consumption of one mole of H_2O_2 and the generation of one mole of oxygen. Recalling from equation 5.1 that one mole of H_2O_2 is produced from consumption of one mole of glucose and one mole of O_2, this means we obtain back all of the oxygen that was used in the enzymatic reaction, some portion of which (which doesn't diffuse away) will again be available for reaction with glucose.

We model the hydrogen peroxide consumption as a concentration of zero at the sensor surface. This is a standard assumption in mass transport simulations [20, 21]. We model the oxygen recycling by imposing flux equality between H_2O_2 and O_2 at the sensor surface. We ignore double-layer charging effects, as impedance spectra of microfabricated sensors show a very small effective double-layer capacitance (Appendix A).

2.6 Simulation Platform

We implemented the simulation using the free and open-source MOOSE framework [22]. We implemented custom physics to incorporate two-substrate enzyme kinetics and oxygen recycling at the sensor electrode and performed steady-state and transient simulations for a variety of in vitro and in vivo configurations. The simulation was performed as a pseudo-3D simulation in the form of an axisymmetric RZ simulation. This enables us to visualize simulations carried out with identical mathematics as would apply to a full 3D simulation, and gives us the spatial degrees of freedom we need to simulate the geometries of interest, while also being able to use the symmetry to reduce the computation time to that of a 2D simulation.

MOOSE framework simulations are also particularly amenable to being automated via Bash (the popular Unix scripting language) scripting to, for example, run the same simulation multiple times with different bulk concentrations, or to keep all other parameters the same but vary the enzyme layer thickness, and such scripts were implemented for exploring sensor geometries.

Automatic differentiation [23] was leveraged in the creation of this simulation.

2.7 Mesh Design

Mesh design is a key component of analysis using the finite element method, requiring balancing computing time and resources with the desired accuracy and resolution. Since we have set up the problem as an axisymmetric RZ simulation, we generate a 2D mesh to represent one half of a slice through a cylinder, with the y-axis of the mesh representing the axis of symmetry. We used a combination of a coarse mesh representing the sensor environment and a fine mesh representing the enzyme layer.

We generated meshes with cells growing geometrically (constant ratio) along the x-axis the further away they are from the sensor center, as we need less resolution far away from the sensor. Within the enzyme layer, the cells grow until reaching the halfway point of the enzyme layer and shrink back down, until reaching the top of the enzyme layer, as diffusion gradients are highest near the top and bottom of the enzyme layer and these are the locations where precision is most needed. Finally, the environment mesh grows geometrically in both the x- and y-dimensions.

Figure 2.1 shows the mesh used in the example simulation presented later. It represents half the cross-section of a cylindrical geometry (the y-axis representing the axis of symmetry). The red mesh at the bottom-left is the mesh for the enzyme

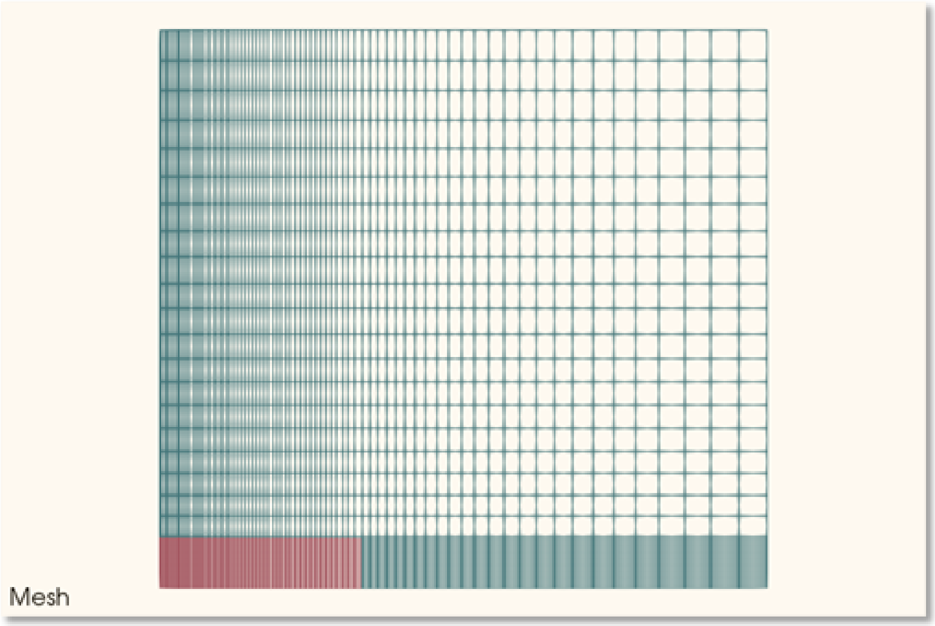

Figure 2.1: The mesh used in the example simulation.

whereas the coarse green mesh is the mesh for the bulk solution. Figure 2.2 shows a close-up of the finer enzyme mesh whereas Figure 2.3 shows the complete simulated slice through cylindrically symmetric geometry after mirroring around the axis of symmetry in postprocessing.

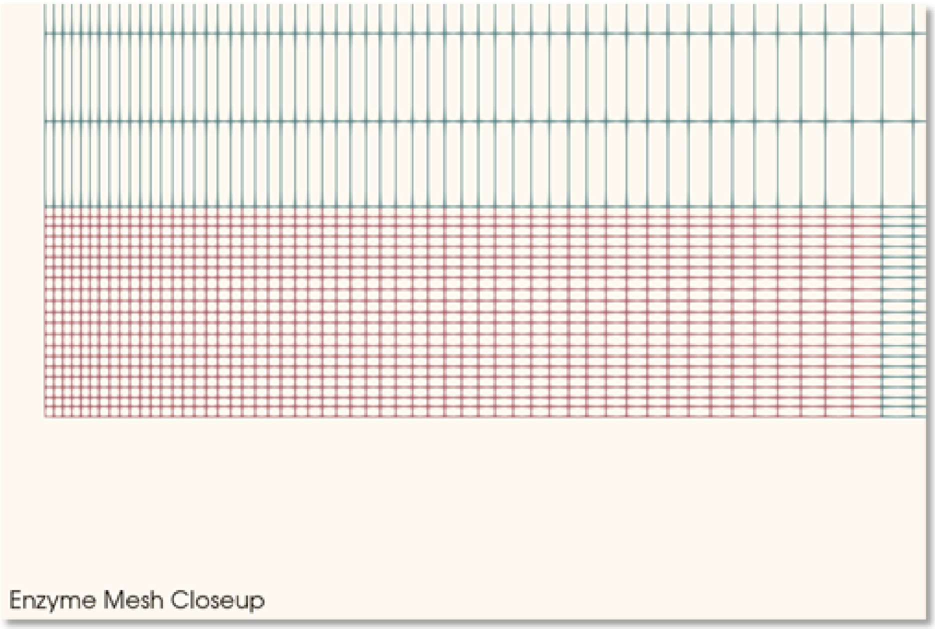

Figure 2.2: Closeup of the finer-meshed enzyme portion.

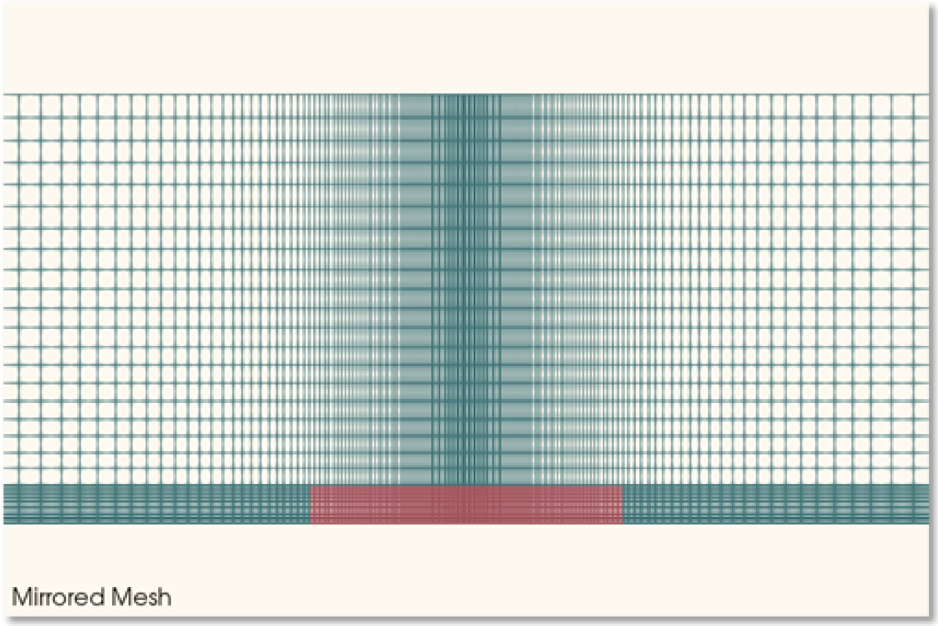

Figure 2.3: The mirrored mesh after postprocessing represents a slice through a cylindrically-symmetric 3D geometry.

2.8 Physics and Boundary Conditions Implementation

Two-substrate enzyme kinetics were implemented with custom kernels, and peroxide consumption at the electrode was implemented with a Dirichlet boundary condition enforcing zero concentration at the electrode surface. Oxygen recycling was implemented as a custom Neumann boundary condition enforcing equality between the oxygen flux from the electrode surface and the peroxide flux into it. The inactive part of the sensor surface (around the electrode) was implemented with a zero-valued Neumann boundary condition. The interface between the solution and the enzyme was implemented using a combination of a matched-value boundary condition with coefficients enforcing partition of concentrations between the two media, and an interface diffusion kernel enforcing mass conservation. Finally, the very outer edges of the environment were implemented using the inbuilt Diffusion Flux boundary condition, which adds the gradient of the concentration profile to the residual at the boundary, or a zero-valued Neumann boundary condition to enforce zero flux and simulate a finite and bounded environment.

2.9 Time Stepping

Control over the time-stepping algorithm is another key area requiring optimization for faster processing and better precision. The specific time-stepping strategies employed will, of course, vary by the specific geometry being simulated, but the broad approach we use is of combining multiple time steppers. MOOSE Framework allows us to specify more than one time-stepping algorithm, each of which may be dependent on the phase or state of the simulation, and allow the simulation to choose the one with the smallest time step. We combine an iterative adaptive time stepper with pre-programmed function-of-time time steppers to force higher temporal resolution in critical phases of the simulation.

2.10 Example Simulation

For the example simulation, we simulate a cylindrical sensor environment with 'extended' boundary conditions (allowing flux into and out of the boundary). The sensor has a radius of $70\mu m$. The enzyme-containing hydrogel layer is 20 μm thick and has a radius of 80 μm. The simulation was run six times, each time with a different bulk glucose concentration between 1 and 32 mM. Bulk solution oxygen concentration was kept fixed at 260 μM, the equilibrium concentration at room temperature and pressure.

The example simulation conjures a scenario where the enzyme-coated sensor, fully deprived of both glucose and oxygen, is suddenly brought into contact with a solution containing both at time $t = 0$. For $30s$, the glucose and oxygen are allowed to diffuse into and react in the enzyme layer, at which point the sensor is turned on. While not physically realizable, this simulation showcases the diffusive, enzyme kinetic, and sensor turn-on dynamics.

Parameter	Description	Value
V_{max}	Maximum enzymatic reaction rate per unit volume	$10\,mMs^{-1}$
K_G	Michaelis constant with respect to glucose	$110\,mM$
K_{O_2}	Michaelis constant with respect to oxygen	$480\,\mu M$
D_G	Glucose diffusivity in water	$7.20 \times 10^{-10}\,m^2 s^{-1}$
D_{O_2}	Oxygen diffusivity in water	$1.93 \times 10^{-9}\,m^2 s^{-1}$
$D_{H_2O_2}$	Hydrogen peroxide diffusivity in water	$1.43 \times 10^{-9}\,m^2 s^{-1}$
$\alpha_{H_2O_2}$	Partition coefficient for H_2O_2	0.2
α_{O_2}	Partition coefficient for O_2	0.2
$\alpha_{Glucose}$	Partition coefficient for glucose	0.2
$\beta_{H_2O_2}$	Relative diffusion coefficient for H_2O_2	1.0
β_{O_2}	Relative diffusion coefficient for O_2	1.0
$\beta_{Glucose}$	Relative diffusion coefficient for glucose	0.3
r_s	Sensor radius	$70\,\mu m$
r_e	Enzyme radius	$80\,\mu m$
h_e	Enzyme height	$20\,\mu m$
t_{on}	Time at which sensor is turned on	$30\,s$
t_{dur}	Measurement duration	$60\,s$
c_G	Bulk glucose concentration	$1 - 32\,mM$
c_{O_2}	Bulk oxygen concentration	$260\,\mu M$

Table 2.3: All parameters for the example simulation.

2.11 Glucose Diffusion and Reaction

Figure 2.4 shows the initial glucose concentration, zero in the enzyme layer and $1.0\,mM$ in bulk solution. Figure 2.5 shows the concentration profile after $0.1\,s$. The glucose has begun diffusing into the hydrogel layer, where it will react with oxygen. Figure 2.6 shows the glucose concentration profile after 2.0 s. The glucose profile remains largely changed after this point. The glucose concentration is lower deep into the enzyme layer (due to consumption) than it is on the boundaries, where it is, of course, in equilibrium with bulk solution.

To prevent the partition coefficient between bulk solution and hydrogel distorting the visualization, the color bars have been rescaled for inside the hydrogel layer vis-à-vis outside. With a partition coefficient of 0.2, as here, a concentration of $0.2\,mM$ inside the hydrogel layer has the same color as a concentration of 1.0 outside. This enables the colors to transition smoothly from bulk to hydrogel, properly visualizing the equilibrium between the two.

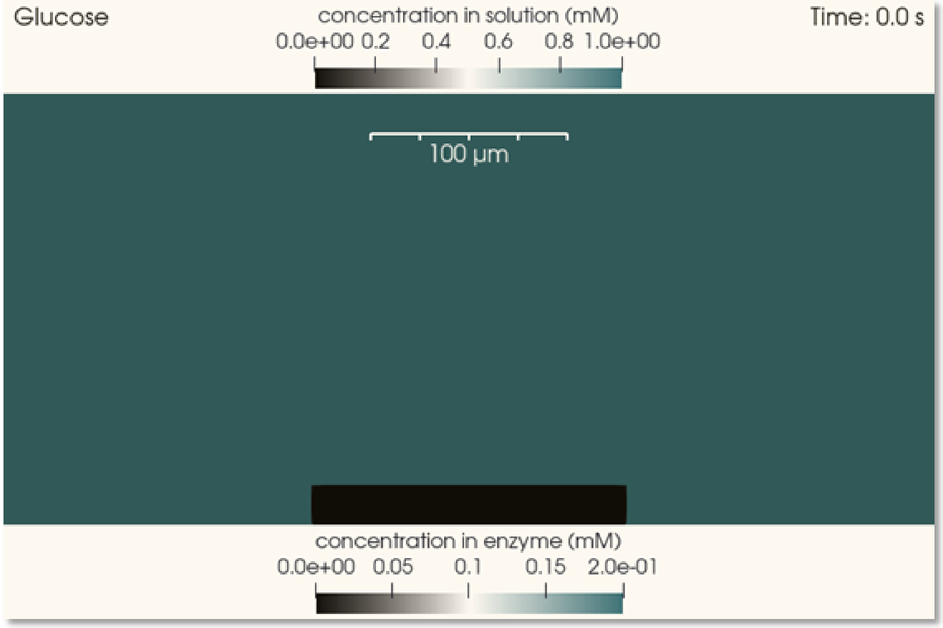

Figure 2.4: Glucose concentration profile with $c_G = 1.0\,mM$ at $t = 0.0\,s$

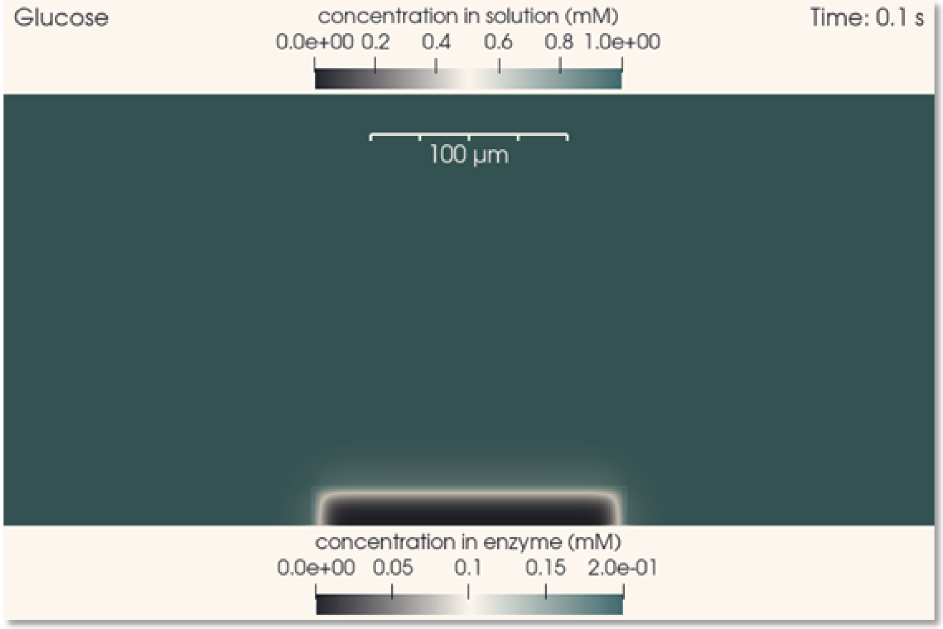

Figure 2.5: Glucose concentration profile with $c_G = 1.0\,mM$ at $t = 0.1\,s$

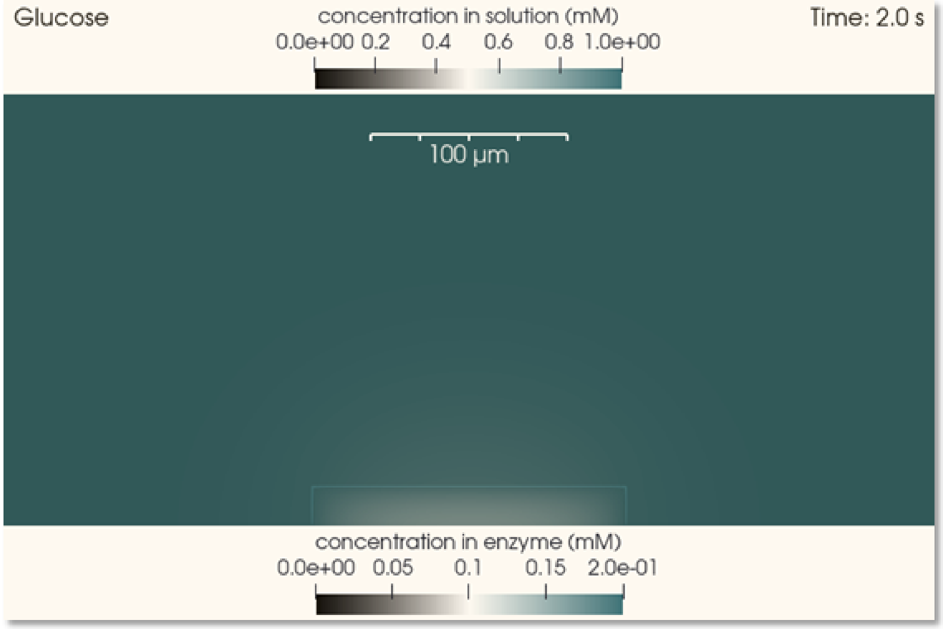

Figure 2.6: Glucose concentration profile with $c_G = 1.0\,mM$ at $t = 2.0\,s$

2.12 Oxygen Diffusion and Reaction

Figure 2.7 shows the starting oxygen concentration profile, $0.26 mM$ in bulk solution and zero in the hydrogel. Figure 2.8 shows the O_2 concentration profile at 0.1 s. Due to the higher diffusivity of oxygen, the oxygen has penetrated deeper into the hydrogel here than glucose had at the same time (Figure 2.5). Figure 2.9 shows the O_2 concentration profile at 0.5 s, where it has penetrated fully into the hydrogel layer. Despite the lower concentration of oxygen and the 1:1 stoichiometric ratio of glucose and oxygen consumed by the glucose oxidase reaction, oxygen reaches deeper into the enzyme layer simply due to its higher diffusivity. Intuitively, we would expect the extent of this to depend on glucose concentration and the level of live enzyme loading.

The same color bar rescaling for inside vs. outside hydrogel is done as for the glucose concentration profiles in the previous section.

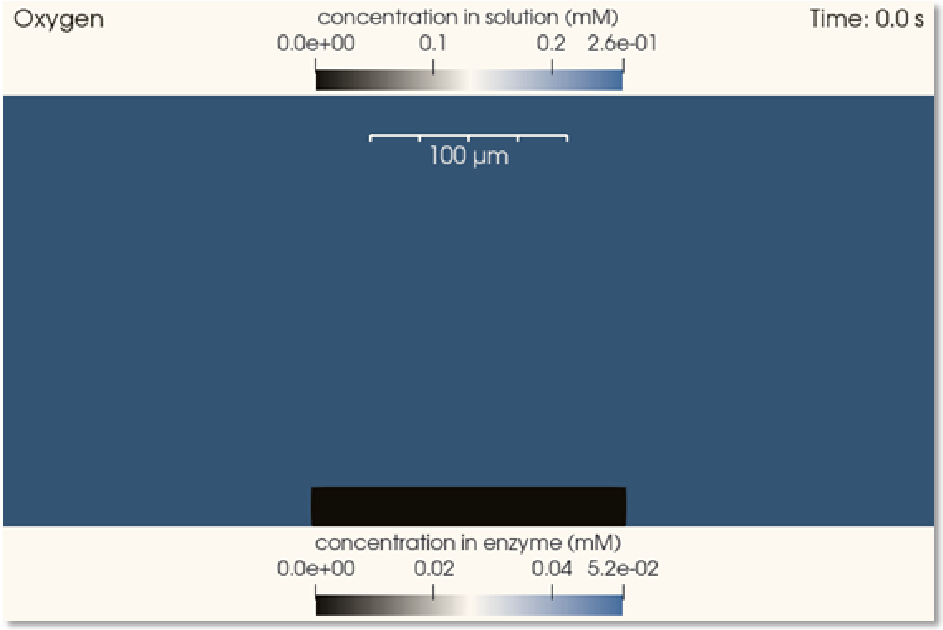

Figure 2.7: O_2 concentration profile with $c_G = 1.0\,mM$ at $t = 0.0\,s$

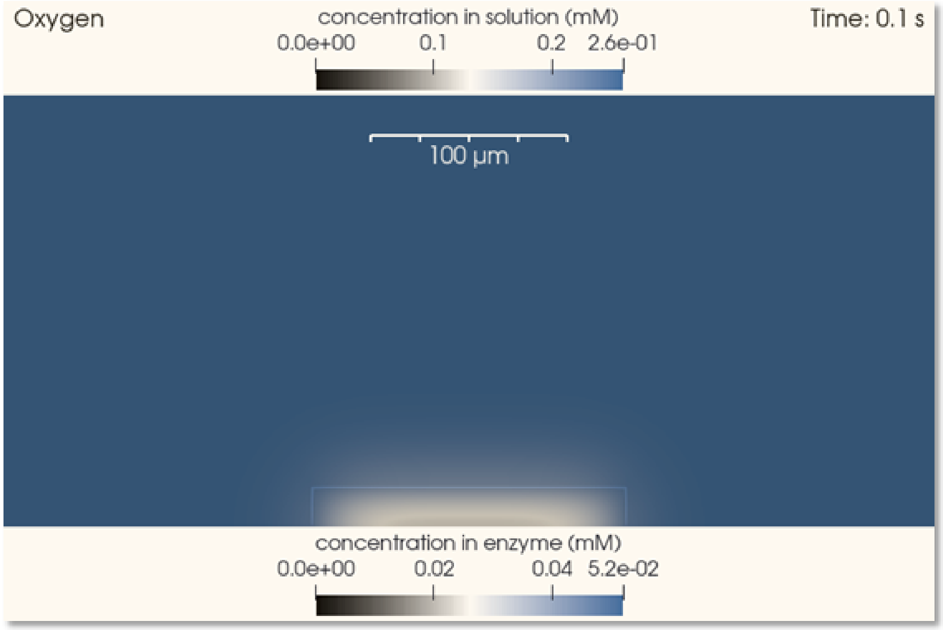

Figure 2.8: O_2 concentration profile with $c_G = 1.0\,mM$ at $t = 0.1\,s$

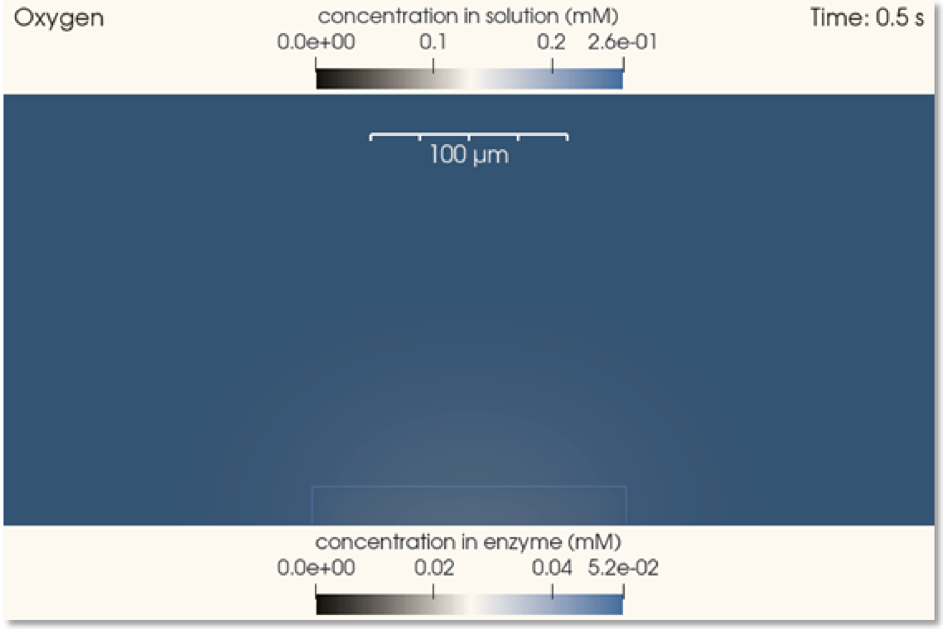

Figure 2.9: O_2 concentration profile with $c_G = 1.0\, mM$ at $t = 0.5\, s$

2.13 Hydrogen Peroxide Generation and Diffusion

Figure 2.10 shows the starting hydrogen peroxide concentration profile, which is zero everywhere. Fig 2.11 shows the H_2O_2 concentration profile at 15.0 s. The enzyme has been generating hydrogen peroxide, which has not only been building up in the hydrogel layer itself but also been diffusing into the solution. The area in the vicinity of the hydrogel has built up a small hydrogen peroxide reservoir. Fig 2.12 shows this reservoir at 30.0 s, the instant before the sensor is turned on in this simulation.

The color bars have been kept consistent for figures 2.11 and 2.12 to enable comparison. The same partition coefficient rescaling has been performed as was done for glucose and oxygen.

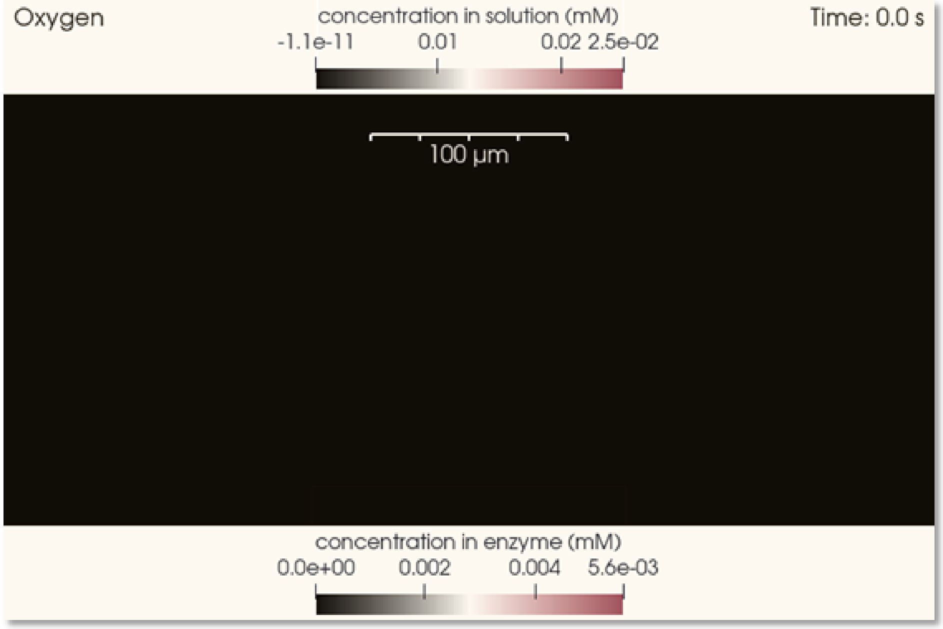

Figure 2.10: H_2O_2 concentration profile with $c_G = 1.0\,mM$ at $t = 0.0\,s$

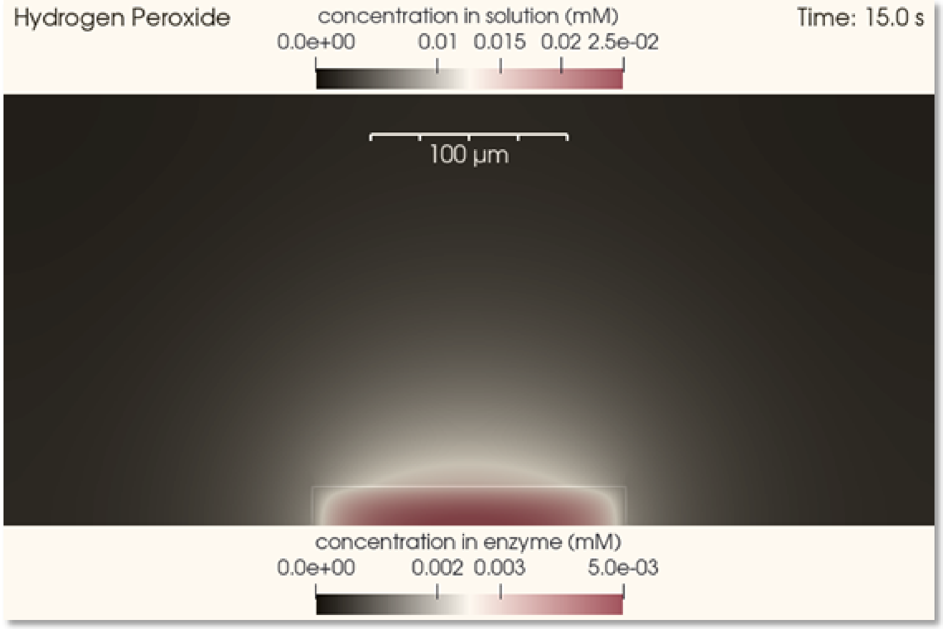

Figure 2.11: H_2O_2 concentration profile with $c_G = 1.0\,mM$ at $t = 15.0\,s$

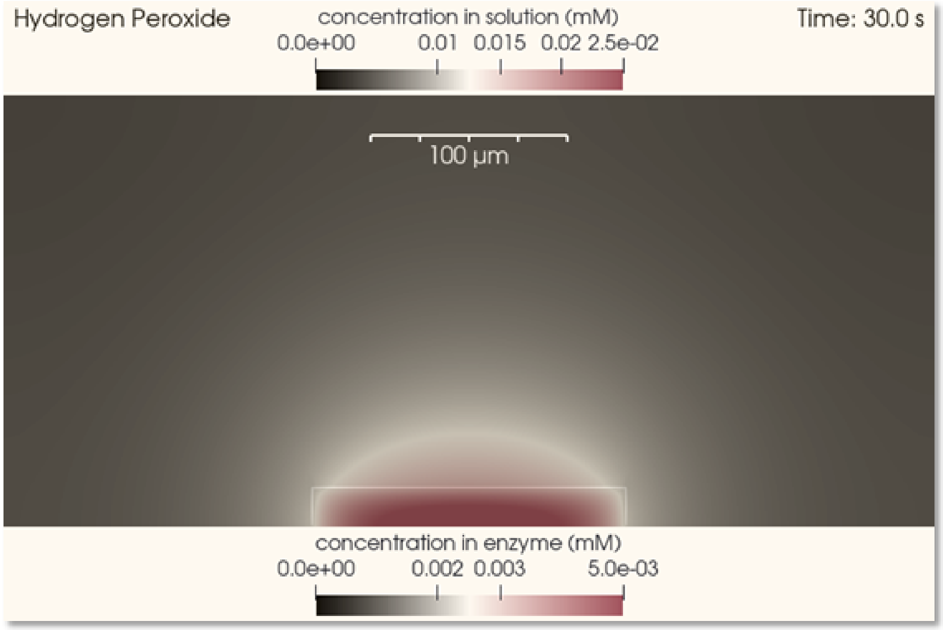

Figure 2.12: H_2O_2 concentration profile with $c_G = 1.0\,mM$ at $t = t_{on}$

2.14 Hydrogen Peroxide Consumption

Figure 2.13 shows the hydrogen peroxide concentration profile 0.2 s after the sensor is turned on. The hydrogel layer has developed a peroxide 'depletion' region immediately above it, seen in black, and the built-up reservoir is collapsing into the sensor surface. Figure 2.14 shows the H_2O_2 profile 0.4 s after sensor turn-on. The reservoir is not quite depleted. Finally, Figure 2.15 shows the concentration profile 2.0 s after sensor turn-on, by which time the built-up reservoir is gone but H_2O_2 continues to be generated by the enzyme and consumed by the sensor.

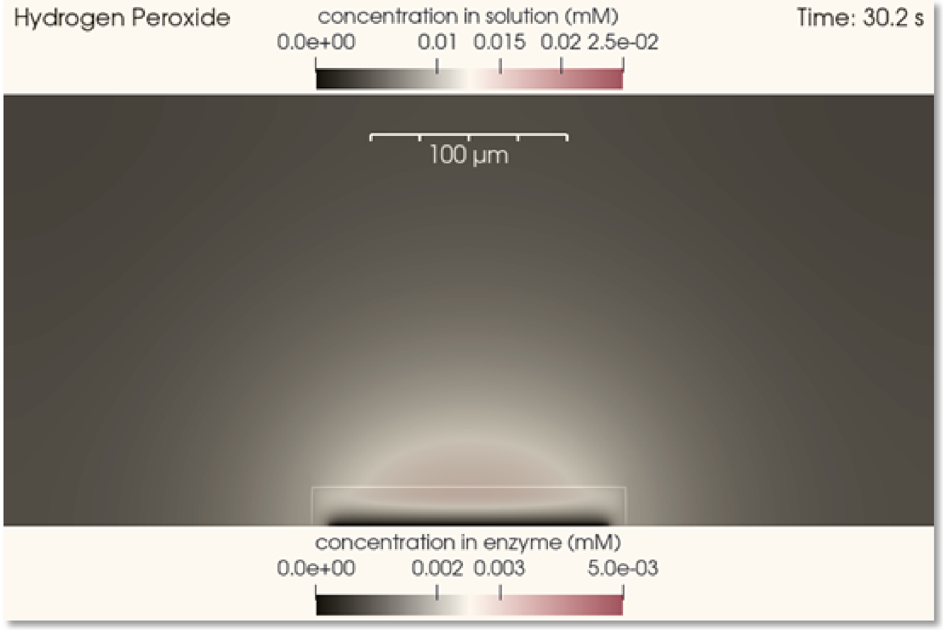

Figure 2.13: H_2O_2 concentration profile with $c_G = 1.0\ mM$ at $t = t_{on}$+0.2 s

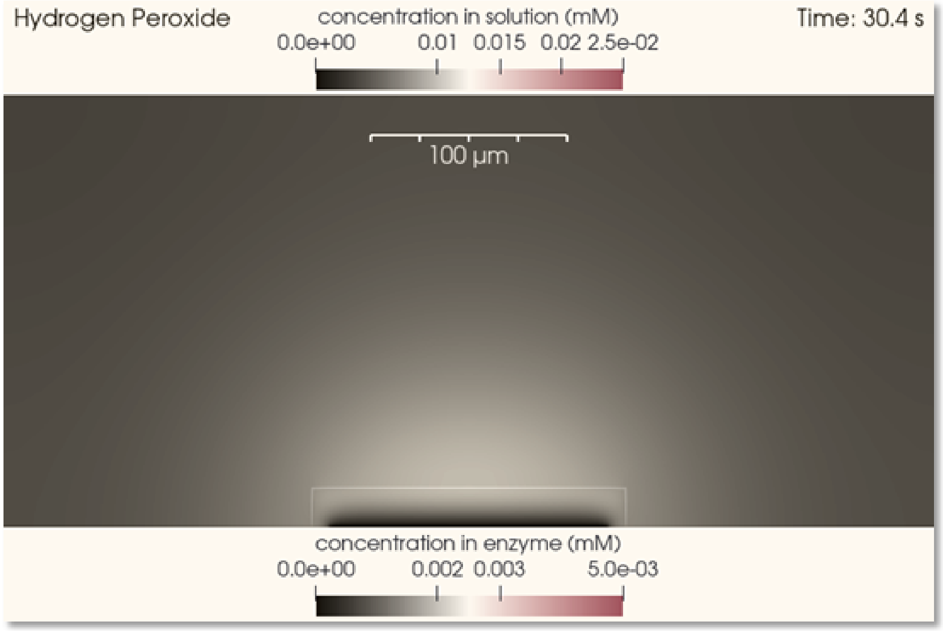

Figure 2.14: H_2O_2 concentration profile with $c_G = 1.0\ mM$ at $t = t_{on}$+0.4 s

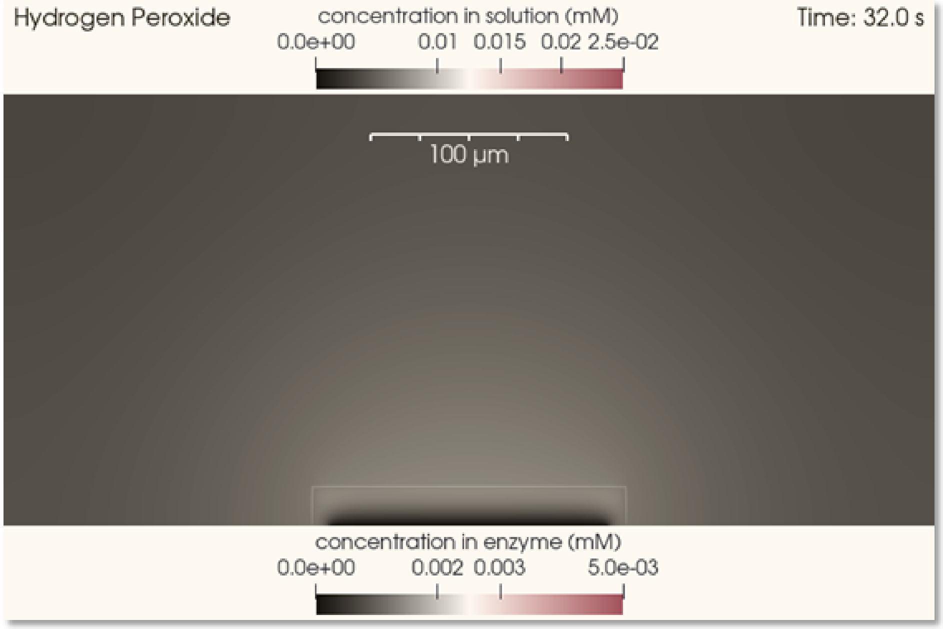

Figure 2.15: H_2O_2 concentration profile with $c_G = 1.0\ mM$ at $t = t_{on}$+2.0 s

Hydrogen Peroxide Consumption at High Glucose Concentration

We now look at the other end of the glucose range simulated, with $c_G = 32.0\ mM$. We skip the glucose and pre-sensor turn-on oxygen profiles and look directly at the H_2O_2 profile. At this end of the range, the H_2O_2 'bubble' extends deeper into the sensor's environment as of the instant the sensor is turned on (Figure 2.16) and remains present even as the measurement progresses, seen at 0.5 s (Figure 2.17) and 10.0 s (Figure 2.18) into the measurement.

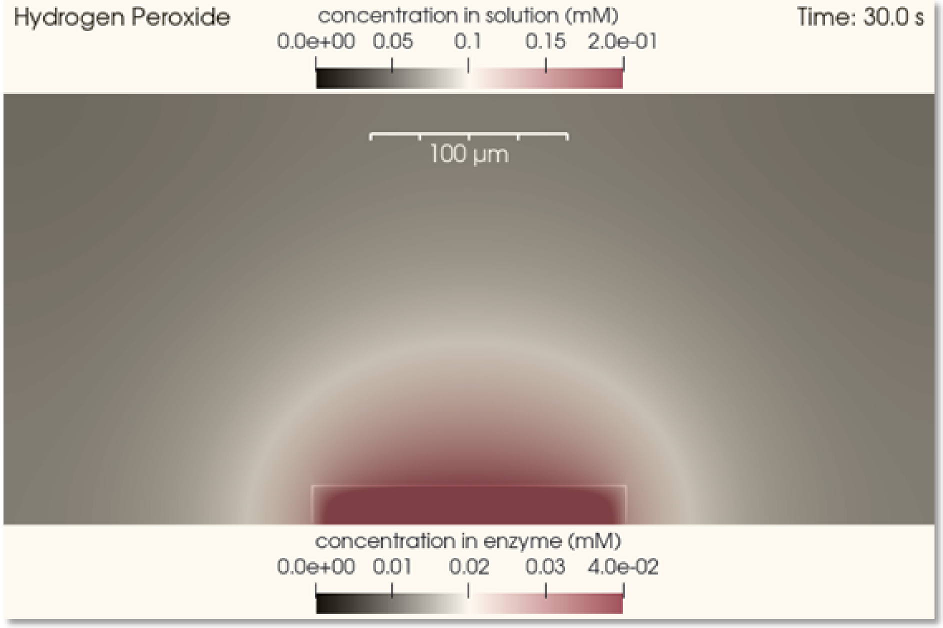

Figure 2.16: H_2O_2 concentration profile with $c_G = 1.0\,mM$ at $t = t_{on}$+0.0 s

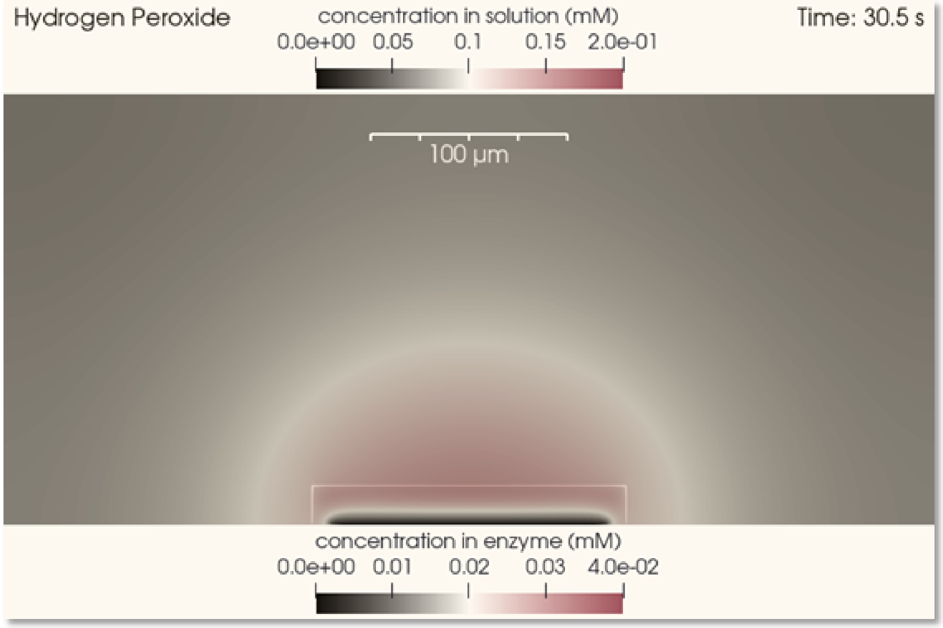

Figure 2.17: H_2O_2 concentration profile with $c_G = 1.0\,mM$ at $t = t_{on}$+0.5 s

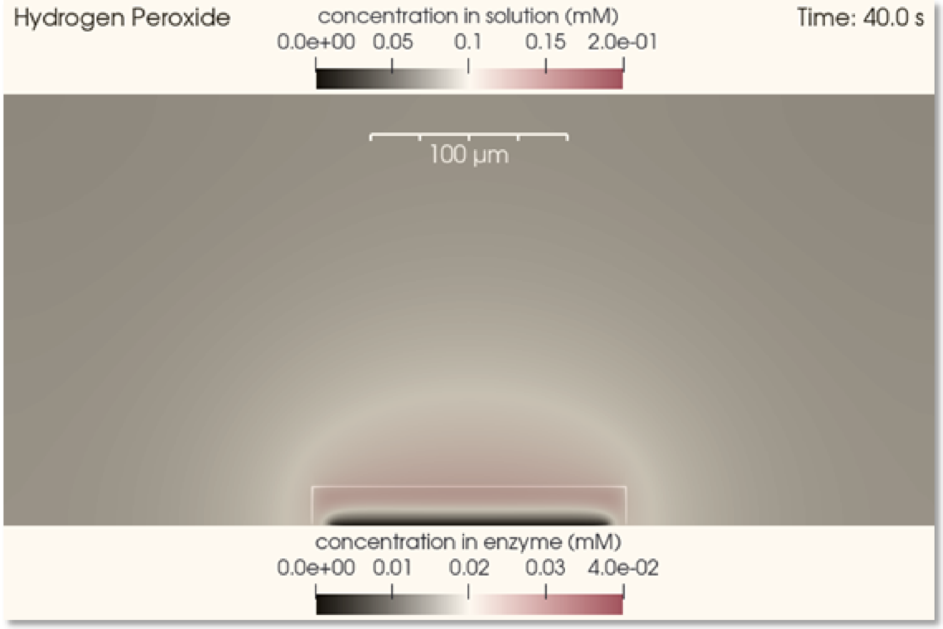

Figure 2.18: H_2O_2 concentration profile with $c_G = 1.0\ mM$ at $t = t_{on}$+10.0 s

2.15 Oxygen Recycling

Finally, we turn our attention to oxygen recycling at the electrode. Each mole of H_2O_2 consumed at the electrode produces a mole of O_2, as described earlier in this chapter, which diffuses back towards the hydrogel, where it is free once again to react enzymatically with glucose and produce H_2O_2 to be detected at the sensor.

Figure 2.19 shows the oxygen concentration profile the instant the sensor is turned on, before recycling has begun. The initial bulk glucose concentration here is $c_G = 32.0\,mM$ and noticeably more oxygen has been depleted not only in the sensor environment but also in the hydrogel layer than was depleted in the corresponding profile with $c_G = 1.0mM$ (Figure 2.9). Figure 2.20 shows oxygen concentration $0.5s$ into the measurement, where the oxygen in the hydrogel layer has been replenished by oxygen beign produced at the sensor surface from consumption of H_2O_2. Evidently, with the parameters used, this initial burst of oxygen gives way to a comparatively reduced high-oxygen zone near the sensor surface as the measurement continues (Figure 2.21).

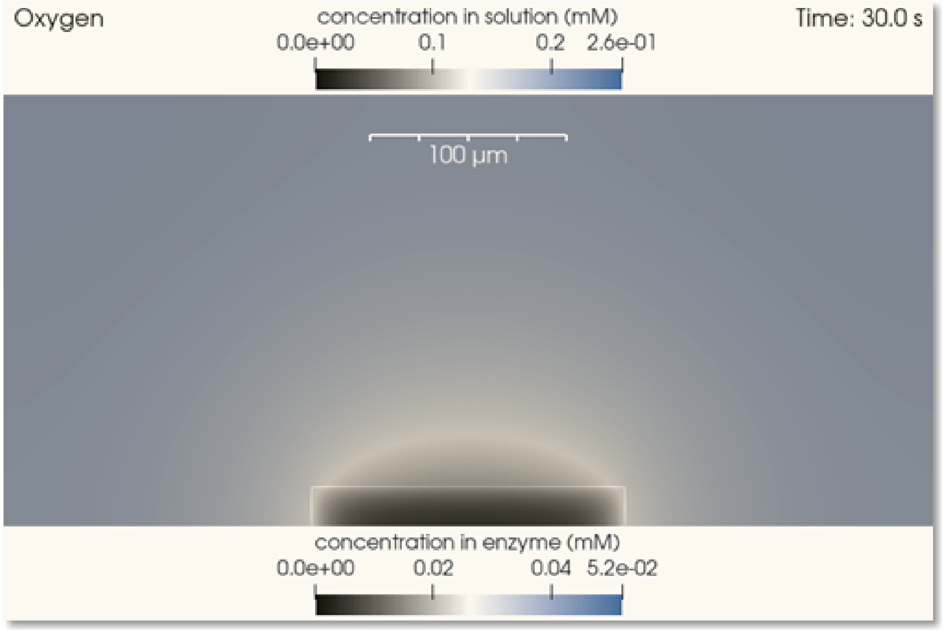

Figure 2.19: O_2 concentration profile with $c_G = 32.0\,mM$ at $t = t_{on}$

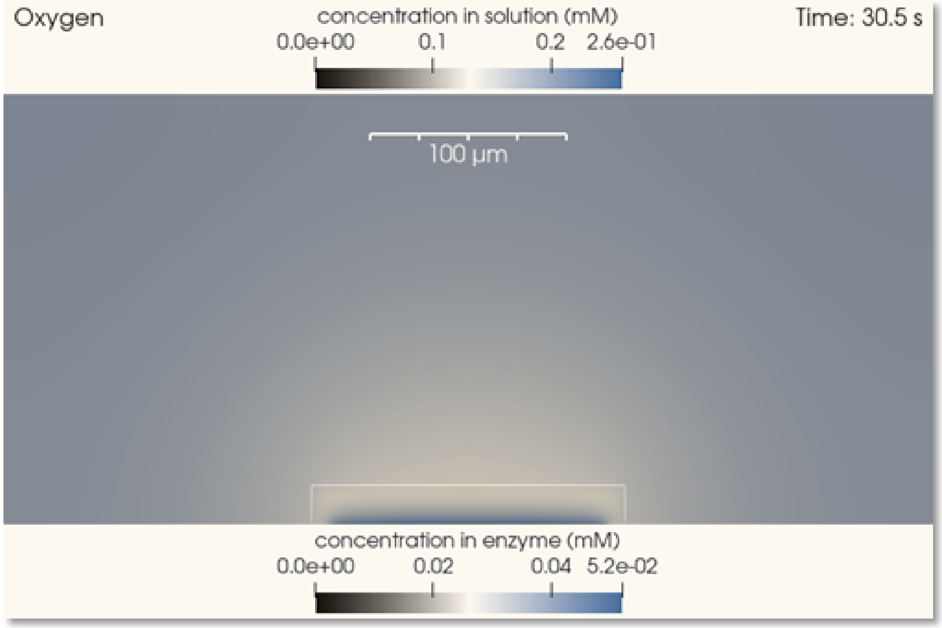

Figure 2.20: O_2 concentration profile with $c_G = 32.0\ mM$ at $t = t_{on}+0.5\ s$

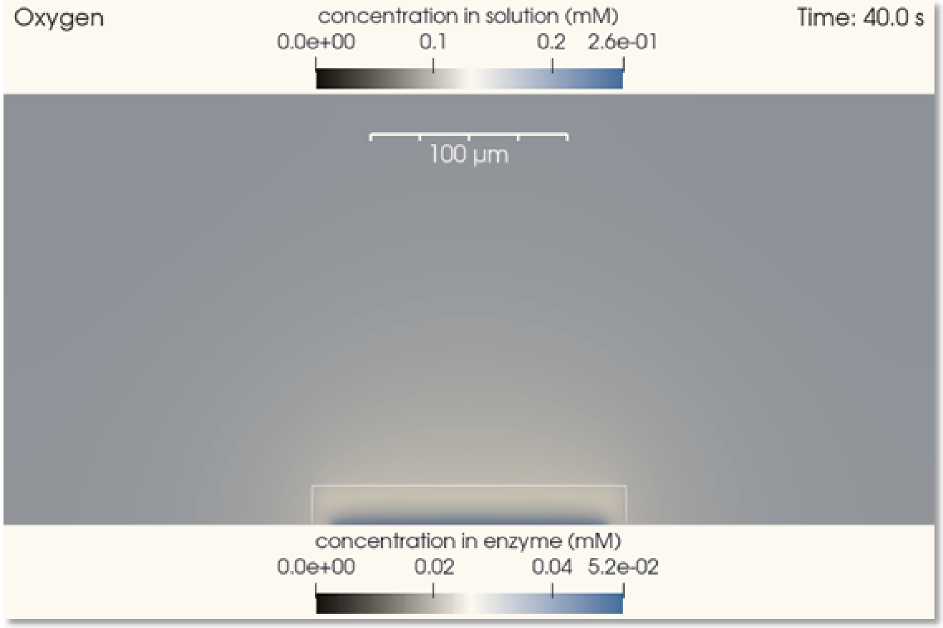

Figure 2.21: O_2 concentration profile with $c_G = 32.0\ mM$ at $t = t_{on}+10.0\ s$

2.16 Simulated Dynamic Response and Sensitivity

The normal H_2O_2 flux into the sensor was converted to current in nA. Figure 2.22 shows the turn-on transient current at the sensor for each concentration over time. There is a rapid initial reduction in the current as the accumulated H_2O_2 reservoir is depleted, followed by a slow rise as the enzyme continues to produce more H_2O_2, which diffuses into the sensor and into the environment, raising the environment H_2O_2 concentration and increasing the percentage of newly-generated H_2O_2 that diffuses to the sensor instead of diffusing into the environment.

Figure 2.23 shows the sensitivity and linearity of this simulated sensor by plotting the mean current sampled between 59 and 60 s vs. the simulated glucose concentration.

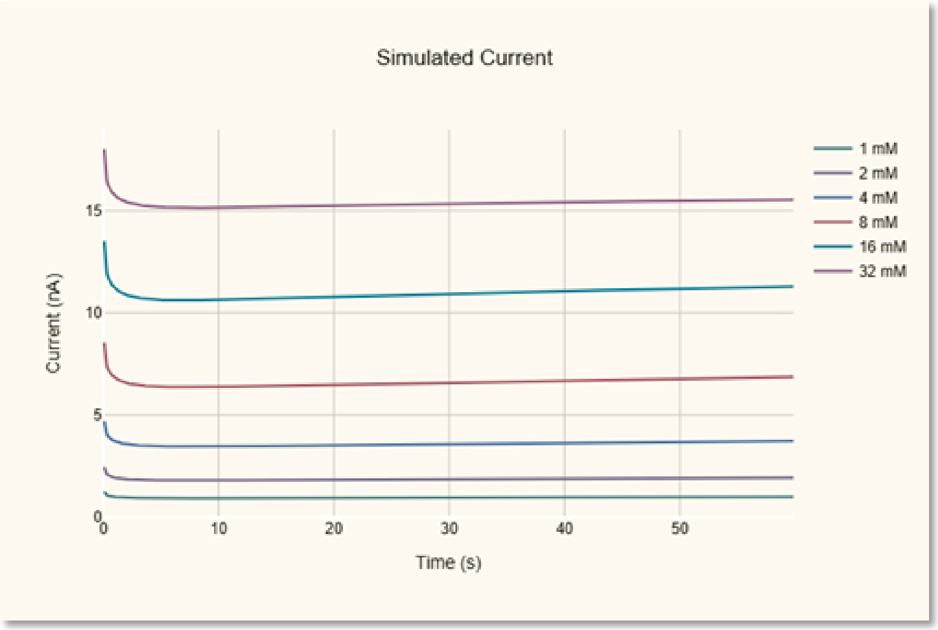

Figure 2.22: Sensor turn-on transients at the simulated glucose concentrations.

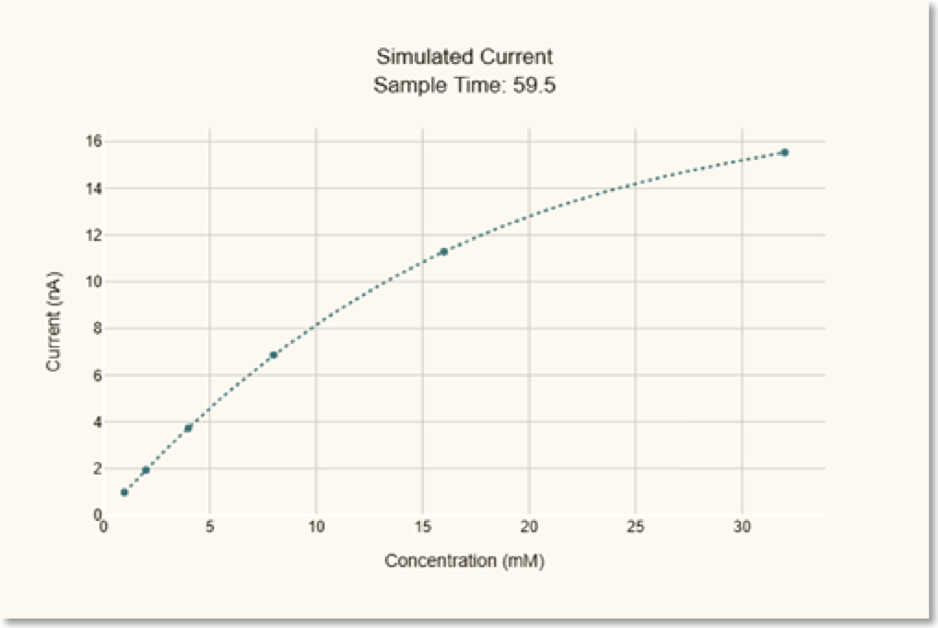

Figure 2.23: Glucose sensitivity of the simulated sensor. Current averaged from samples from 59-60 s. Interpolating spline fit curve shown as dotted line.

2.17 Discussion and Future Improvements

The simulations developed here are a potent tool for predicting trends in the behavior of microfabricated enzyme electrodes. They have the potential to allow a reduction in fabrication time and cost as initial iterations could be performed in silico instead of in vitro. Additionally, they are a potent pedagogical tool for understanding and explaining the transport phenomena involved in microfabricated electrodes.

These simulation tools could also help characterize fabricated electrodes and help determine unknown constants (such as partition or hindered diffusion coefficients), although there is a word of caution there regarding there being too many possible unknown parameters to fit and consequent false confidence in fit results. Nevertheless, it would likely be a powerful future development to add scripts to control the simulation programmatically, process its outputs, and modify selected unknown inputs to fit observed data, especially when as many parameters as possible have otherwise been determined, and fit results are regarded with the due uncertainty.

One major remaining area of improvement is the development of more advanced post-processing tools and methods to expand their scope past MOOSE's inbuilt postprocessors.

References

[1] Dvin Artashes-Boghos Adalian. “Development and Dynamics of Microfabricated Enzymatic Biosensors”. PhD thesis. California Institute of Technology, 2019. DOI: `10.7907/7GHS-NX49`.

[2] Dvin Adalian et al. “Patterned Thin Film Enzyme Electrodes via Spincoating and Glutaraldehyde Vapor Crosslinking: Towards Scalable Fabrication of Integrated Sensor-on-CMOS Devices”. In: *Lab on a Chip* 24.17 (2024), pp. 4172–4181. ISSN: 1473-0197, 1473-0189. DOI: `10.1039/D4LC00206G`.

[3] Arian Hashemi Talkhooncheh et al. “A Biofuel-Cell-Based Energy Harvester With 86% Peak Efficiency and 0.25-V Minimum Input Voltage Using Source-Adaptive MPPT”. In: *IEEE Journal of Solid-State Circuits* 56.3 (Mar. 2021), pp. 715–728. ISSN: 0018-9200, 1558-173X. DOI: `10.1109/JSSC.2020.3035491`.

[4] Quentin H. Gibson, Bennett E.P. Swoboda, and Vincent Massey. “Kinetics and Mechanism of Action of Glucose Oxidase”. In: *Journal of Biological Chemistry* 239.11 (Nov. 1964), pp. 3927–3934. ISSN: 00219258. DOI: `10.1016/S0021-9258(18)91224-X`.

[5] Takao Nakamura and Ogura Yasuyuki. “Kinetic Studies on the Action of Glucose Oxidase”. In: *The Journal of Biochemistry* 52.3 (Sept. 1962), pp. 214–220. ISSN: 1756-2651, 0021-924X. DOI: `10.1093/oxfordjournals.jbchem.a127599`.

[6] Michael K. Weibel and Harold J. Bright. “The Glucose Oxidase Mechanism”. In: *Journal of Biological Chemistry* 246.9 (May 1971), pp. 2734–2744. ISSN: 0021-9258. DOI: `10.1016/s0021-9258(18)62246-x`.

[7] David Ezra Liu. “Solute Partitioning and Hindered Diffusion in Hydrogels”. UC Berkeley, 2016.

[8] Ioannis Katsounaros et al. “Hydrogen Peroxide Electrochemistry on Platinum: Towards Understanding the Oxygen Reduction Reaction Mechanism”. In: *Physical Chemistry Chemical Physics* 14.20 (May 2, 2012), pp. 7384–7391. ISSN: 1463-9084. DOI: `10.1039/C2CP40616K`.

[9] J. W. Parker and C. S. Schwartz. “Modeling the Kinetics of Immobilized Glucose Oxidase”. In: *Biotechnology and Bioengineering* 30.6 (Oct. 20, 1987), pp. 724–735. ISSN: 0006-3592, 1097-0290. DOI: `10.1002/bit.260300605`.

[10] Naveed Ahmad Khan et al. “Mathematical Analysis of Reaction–Diffusion Equations Modeling the Michaelis–Menten Kinetics in a Micro-Disk Biosensor”. In: *Molecules* 26.23 (Dec. 2, 2021), p. 7310. ISSN: 1420-3049. DOI: `10.3390/molecules26237310`.

[11] M. Lilly Clarance Mary et al. “Mathematical Modeling of Immobilized Enzyme in Porous Planar, Cylindrical, and Spherical Particle: A Reliable

Semi-Analytical Approach". In: *Reaction Kinetics, Mechanisms and Catalysis* 134.2 (Dec. 2021), pp. 641–651. ISSN: 1878-5190, 1878-5204. DOI: `10.1007/s11144-021-02088-4`.

[12] Marco Fratus et al. "Geometry-Defined Response Time and Sensitivity for Microneedle-Based Amperometric Sensors". In: *IEEE Sensors Journal* 23.13 (July 2023), pp. 14285–14294. ISSN: 1558-1748. DOI: `10.1109/JSEN.2023.3277425`.

[13] Seyed Mohsen Hashem Zadeh et al. "Numerical Modeling and Investigation of Amperometric Biosensors with Perforated Membranes". In: *Sensors* 20.10 (10 Jan. 2020), p. 2910. ISSN: 1424-8220. DOI: `10.3390/s20102910`.

[14] V. Leskovac et al. "Glucose Oxidase from Aspergillus Niger: The Mechanism of Action with Molecular Oxygen, Quinones, and One-Electron Acceptors". In: *The International Journal of Biochemistry & Cell Biology* 37.4 (Apr. 2005), pp. 731–750. ISSN: 1357-2725. DOI: `10.1016/j.biocel.2004.10.014`.

[15] S.A.M. Van Stroe-Biezen et al. "Diffusion Coefficients of Oxygen, Hydrogen Peroxide and Glucose in a Hydrogel". In: *Analytica Chimica Acta* 273.1–2 (Feb. 1993), pp. 553–560. ISSN: 00032670. DOI: `10.1016/0003-2670(93)80202-V`.

[16] Mohammad Raja, Ilanna Campelo Lopes, and Pankaj Vadgama. "A Preliminary Electrochemical Study of Crosslinked Albumin and Collagen Membranes as Diffusion Barriers for Potentially Degradable Chronic Wound Biosensors". In: *Electrochemical Science Advances* 2.4 (Aug. 2022). ISSN: 2698-5977, 2698-5977. DOI: `10.1002/elsa.202100132`.

[17] Igor Krupa et al. "Glucose Diffusivity and Porosity in Silica Hydrogel Based on Organofunctional Silanes". In: *European Polymer Journal* 47.7 (July 2011), pp. 1477–1484. ISSN: 0014-3057. DOI: `10.1016/j.eurpolymj.2011.02.011`.

[18] Tomás E. Benavidez and Ana M. Baruzzi. "Comparative Behavior of Glucose Oxidase and Oxalate Oxidase Immobilized in Mucin/Chitosan Hydrogels for Biosensors Applications". In: *Polymer* 53.2 (Jan. 2012), pp. 438–444. ISSN: 0032-3861. DOI: `10.1016/j.polymer.2011.12.014`.

[19] L. Figueiredo et al. "Assessing Glucose and Oxygen Diffusion in Hydrogels for the Rational Design of 3D Stem Cell Scaffolds in Regenerative Medicine". In: *Journal of Tissue Engineering and Regenerative Medicine* 12.5 (May 2018), pp. 1238–1246. ISSN: 1932-7005. DOI: `10.1002/term.2656`. PMID: `29489057`.

[20] Leroy D. Mell and J. T. Maloy. "Model for the Amperometric Enzyme Electrode Obtained through Digital Simulation and Applied to the Immobilized Glucose Oxidase System". In: *Analytical Chemistry* 47.2 (Feb. 1, 1975), pp. 299–307. ISSN: 0003-2700, 1520-6882. DOI: `10.1021/ac60352a006`.

[21] Leroy D. Mell and J. T. Maloy. “Amperometric Response Enhancement of the Immobilized Glucose Oxidase Enzyme Electrode”. In: *Analytical Chemistry* 48.11 (Sept. 1, 1976), pp. 1597–1601. ISSN: 0003-2700, 1520-6882. DOI: `10.1021/ac50005a045`.

[22] Guillaume Giudicelli et al. “3.0 - MOOSE: Enabling massively parallel multiphysics simulations”. In: *SoftwareX* 26 (2024), p. 101690. ISSN: 2352-7110. DOI: `https://doi.org/10.1016/j.softx.2024.101690`.

[23] Alexander Lindsay et al. “Automatic Differentiation in MetaPhysicL and Its Applications in MOOSE”. In: *Nuclear Technology* (2021), pp. 1–18.

Chapter 3

AUTOMATED MEASUREMENT SYSTEM

3.1 Overview

Despite advances in sensor design, characterizing new enzyme electrodes is still largely a labor-intensive process. Traditional benchtop testing involves pipetting reagents, manually switching samples, and calibrating sensors one at a time. Such manual workflows are slow and susceptible to human error. Additionally, electrochemical measurements are highly susceptible to diffusion effects and are often impacted by factors such as reaction container shape and fill level, the exact position of the sensor within the reaction chamber, and distance from the stir bar if one is used [1][2].

Automation of biosensing systems holds the promise of increasing data throughput and reducing the impact of human error and bias [3]. Automated flow injection systems [4] and sequential injection systems [5] have long been described in the literature and applied to a wide variety of sensors, such as in-line glucose monitoring for cell cultures [6] and fermentation [7], Flow-ELISA [8] and amperometric detection of ethanol [9]. However, to the best of our knowledge, we present here the first automated measurement system for wafer-scale testing of chronoamperometric enzyme electrodes directly on the wafer on which the electrodes were fabricated.

To combat the inconsistencies of manual measurement and enable higher data throughput, we developed an automated measurement system and accompanying software to test sensors at the wafer scale in a repeatable way day after day and sensor across sensor. The goal was to build a system that can recreate an identical environment each time it flushes in a new solution and carries out an electrochemical measurement, while also maintaining a measurement error smaller than 1 nA.

The automated measurement system also enables the use of protocols incorporating randomized concentration order to prevent temporally correlated confounding variables from obfuscating the data while replicating an identical measurement environment each time a new solution is flushed in. An early example of such an error was insulation failures leading to growing electrode area with each successive measurement, which was easily isolated due to automated randomization of analyte concentration order. Additionally, the system increases our data throughput by en-

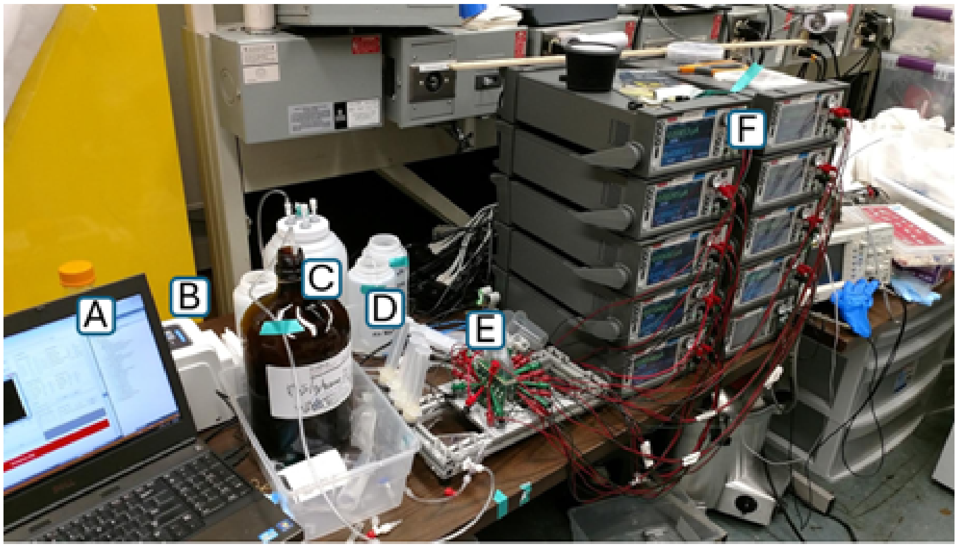

Figure 3.1: The automated measurement system. Labeled are A: computer running measurement software, B: peristaltic pump, C: source and waste containers, D: flow rate noise dampener, E: wafer-holding and flow cell assembly, and F: sourcemeter panel.

abling us to test up to ten sensors at a time, largely unsupervised after the initial setup for a measurement session.

The central piece of the automated measurement system is the wafer-holding and flow cell assembly, where the mechanical, electrical, and fluidic subsystems meet and interface with the fabricated test wafers. The fluidics subsystem consists of a peristaltic pump, pinch valves, a flow rate noise dampener, and plumbing to connect these components to the source and waste containers. The electronics subsystem consists of ten Keithley 2450 sourcemeters acting as potentiostats, a printed circuit board in the flow-cell assembly to make electrical contact with the wafer, an interposer board to connect the two, and a contact tester to ensure the wafer had been correctly aligned. The software subsystem consists of custom application software that controls the sourcemeters, pump, and pinch valves, to direct liquid flow and electrochemical measurement, and collect and store data as well as forensic and diagnostic information. It additionally comprises of scripts to parse and analyze the data files and collate comments entered by experimenters through the course of a measurement session through the main application software.

3.2 Flow Cell Assembly

The flow cell assembly was the central piece of the automated measurement system. It provided a precisely machined 6061 aluminum base on which to place the wafer and align it precisely using the wafer flat. The wafer flat was also used in a sister wafer-marking assembly to create mechanical marks on the wafer, which were subsequently referenced during lithography steps. Consequently, wafer features were ultimately precisely aligned to the flat and enabled the electrical contacts to end up in the same location each time.

Figure 3.2: 250 µm mechanical mark aligned with lithographically defined feature.

The top manifold contained flow cells milled into PMMA with machined 6061 aluminum backing. The bottom of each flow cell had a groove for an O-ring whereas the top had two 9-gauge thin wall stainless steel needles to enable connection to flexible plastic tubing. It was also fitted with a printed circuit board with spring connectors for making electrical contact with the wafer and female headers on the other side for connection to the sourcemeters. The spring connectors were hand soldered with extreme care as to mechanical placement to ensure alignment with the wafer contact pads. This manifold was precisely aligned to the base using metal dowel pins inserted into corresponding holes in the base and the manifold aluminum backing and then screwed into place to maintain the correct pressure for O-ring sealing. Figure 4: The flow cell assembly with a test wafer in the system.

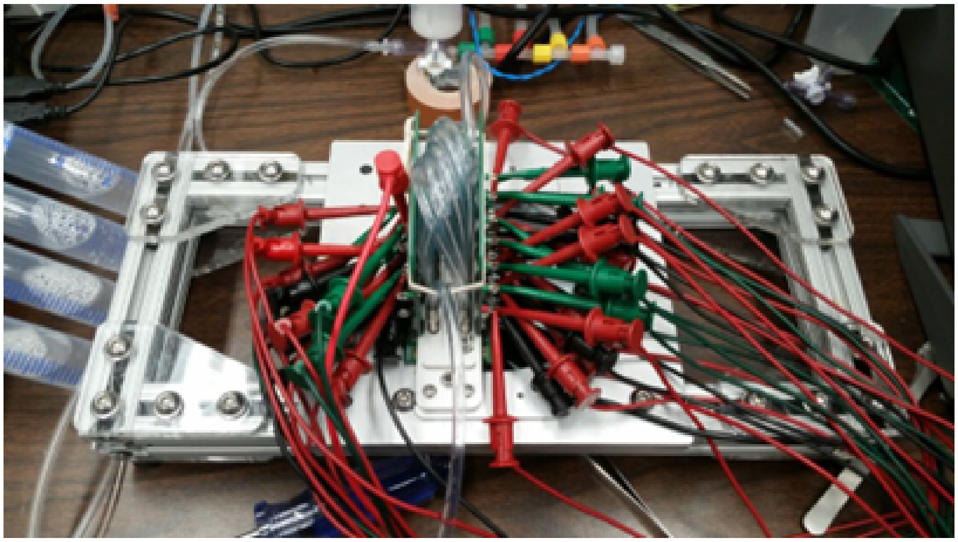

Figure 3.3: Flow cell assembly. Pictured is an early iteration of the interposer with mini grabber cables instead of the ribbon cables used later.

The bottom of the flow cells is exposed, showing the flow cells themselves, the spring connectors that contact the wafer, and the O-rings that form the seal. The aluminum backing contains alignment holes (one on each side) and holes for screws for maintaining sealing pressure (two on each side).

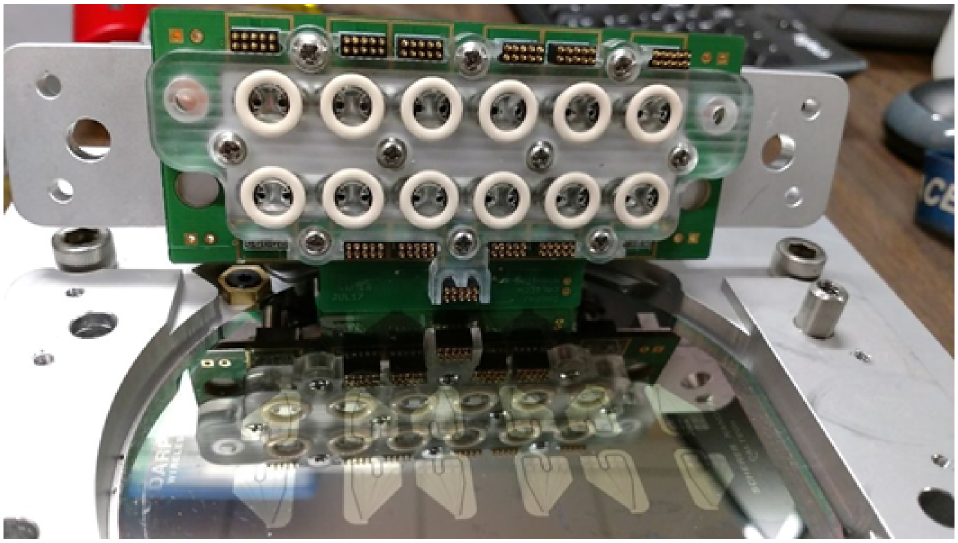

Figure 3.4: The flow cell assembly with a test wafer in the system. The bottom of the flow cells is exposed, showing the flow cells themselves, the spring connectors that contact the wafer, and the O-rings that form the seal. The aluminum backing contains alignment holes (one on each side) and holes for screws for maintaining sealing pressure (two on each side).

3.3 Fluidics Subsystem

After some initial experimentation with single- and dual-syringe pump configurations, a peristaltic pump was chosen for the final system build. A Langer Instruments BT100 was selected as the primary pump, with a BT300 available if needed for high-speed flushes. Silicone tubing from the pump manufacturer was selected for the tubing within the pump. Chemical-resistant clear plastic tubing with 1/8” inner diameter was selected for the rest of the tubing.

Figure 3.5: Inline flow rate noise dampener comprising of four syringes with plungers fixed in place with adhesive.

It was desired to be able to carry out both ‘flow’ and ‘static’ measurements (with and without liquid flow during measurement), but peristaltic pumps create a noisy flow rate due to the effect of the rollers [10]. A very effective low-cost solution was found in the form of a noise dampener consisting of partially-filled syringes in which the plunger was fixed in place with permanent adhesive placed in-line with liquid flow. The air gap in the syringes would compress and relax with changing pressure, effectively smoothing out the flow rate. The dampener reduced all flow rate-related noise from the measurements to below measurement threshold.

Solenoid pinch valves were used to select between different premixed source solutions. A custom electronic controller was designed to allow our software to control the experiment. Luer-lock or barb connectors were used for tubing connections. The system was primarily used in a negative pressure configuration both to enable placing the flow noise dampener downstream of the flow cells to avoid contamination with the buffer liquid in the syringes and to reduce chances of liquid leakage,

Figure 3.6: Solenoid pinch valves, controller, and fluid source containers

which (though rare) necessitated elaborate cleaning and drying to eliminate current leakage paths and return to the specified < 1 nA precision requirement.

3.4 Electrical Subsystem

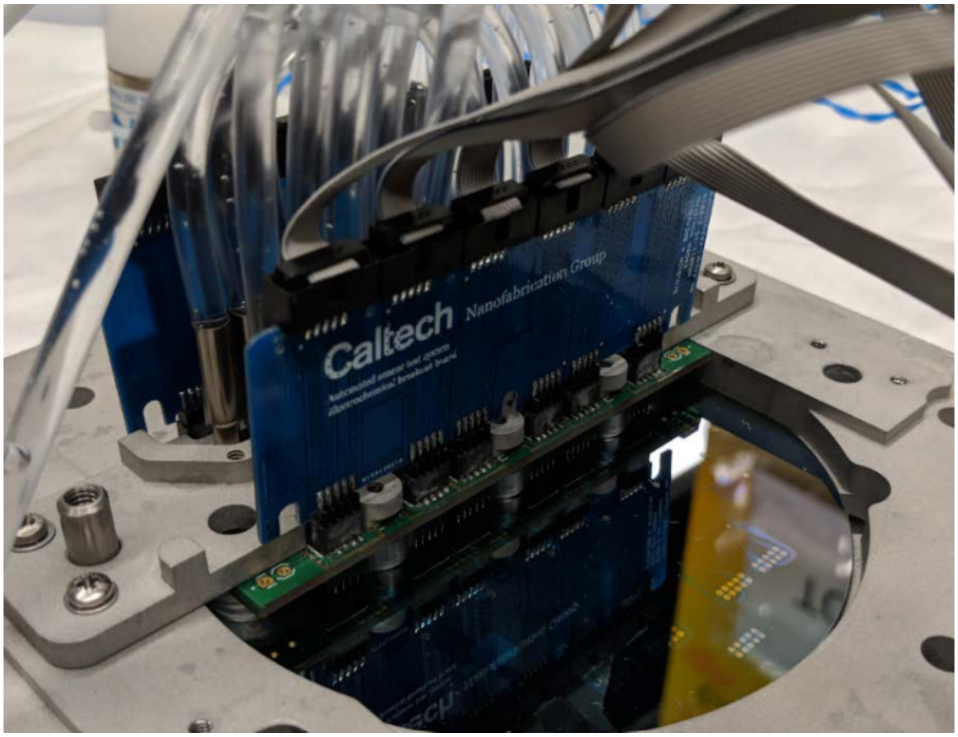

Figure 3.7: Interposer board

The electrical subsystem consisted of a rack of ten Keithly 2450 sourcemeters used in four-wire (potentiostatic) mode, an interposer board to connect these to the headers on the flow cell manifold, the pinch valve controller described in the previous section, and a board to adapt the banana connectors on the Keithly output panel to flat ribbon cables, which connected to the interposer board, pictured here. The interposer board and adapter contained guard traces around the working and reference electrode traces to avoid current leakage through the FR4 PCB material and maintain < 1 nA leakage current.

3.5 Software Subsystem

Full-featured application software was created for use not only by this researcher but also by colleagues and collaborators. The goal was to enable automated testing by any member of the overall project (or partnered projects led by collaborators) without needing knowledge of programming.

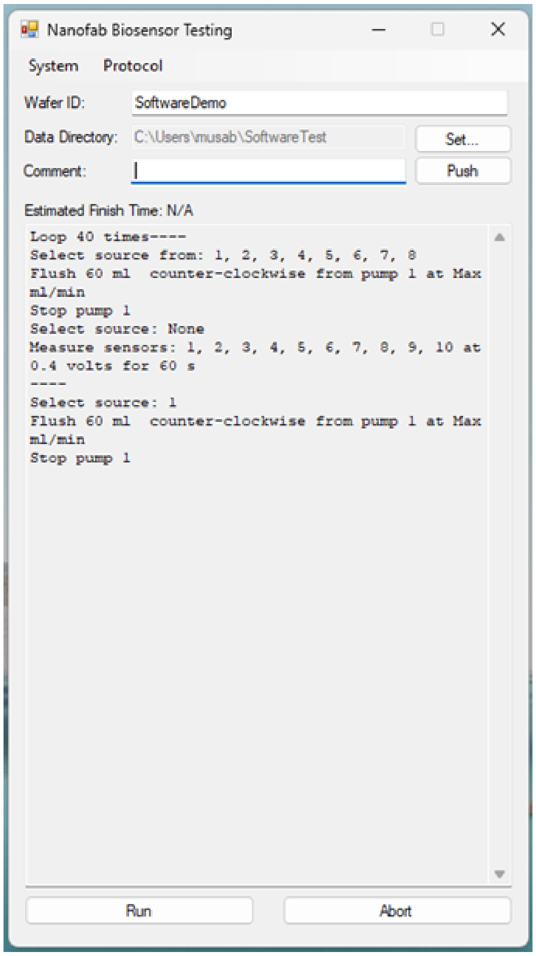

Wafer ID: SoftwareDemo

Data Directory: C:\Users\musab\SoftwareTest

Comment:

Estimated Finish Time: N/A

```
Loop 40 times----
Select source from: 1, 2, 3, 4, 5, 6, 7, 8
Flush 60 ml  counter-clockwise from pump 1 at Max
ml/min
Stop pump 1
Select source: None
Measure sensors: 1, 2, 3, 4, 5, 6, 7, 8, 9, 10 at
0.4 volts for 60 s
----
Select source: 1
Flush 60 ml  counter-clockwise from pump 1 at Max
ml/min
Stop pump 1
```

Figure 3.8: Software main screen

The system was highly multithreaded, allowing a live-updating and fully responsive graphical interface running in parallel with threads managing each piece of connected equipment. Additionally, there were threads constantly logging interthread messages to save forensic data.

At a low level, the software interfaces with the pump, sourcemeters, and pinch valve controller, issuing commands, verifying readbacks, and collecting data. At a higher level, it enables the creation of custom experimental protocols through a convenient user interface, also allowing them to be saved and loaded.

The main software screen provides an overview of the loaded experimental protocol and an estimated finish time once it's running. A separate detailed live-updated system status screen is also provided for live-monitoring of the link status with each connected instrument.

Sourcemeter Control

The Tektronix TSP command interface was used to drive the Keithly sourcemeters and obtain data. Each sourcemeter was run on a separate thread for full nonblocking operating and to avoid communication issues with one sourcemeter affecting measurements on another. A sensor panel configuration screen allows the user to select the sourcemeter IDs.

Fluidics Control

Support is provided for Langer BT100 and BT300 pumps, including support for connecting more than one pump simultaneously and using each at a different time in the experiment protocol. The BT300 pump has higher flow rate but less precision in adjusting it, allowing for faster flushes for static measurements whereas the BT100 pump allows greater precision in tuning the flow rate. A protocol could, for instance, use a BT300 pump to flush new fluid in and then switch to a BT100 pump to maintain a precise flow rate during measurement. Both pumps need routine flow rate calibration due to gradual tubing degradation before the tubing needs replacement, and the software provides a feature for researchers to perform a calibration protocol and update a calibration table.

A container/valve control screen allows the researcher to connect to the pinch valve controller and designate which containers are connected to the system as well as the name and concentration of the fluid in each. A ping feature is made available for the researcher to confirm connections on the correct COM ports for the valves and

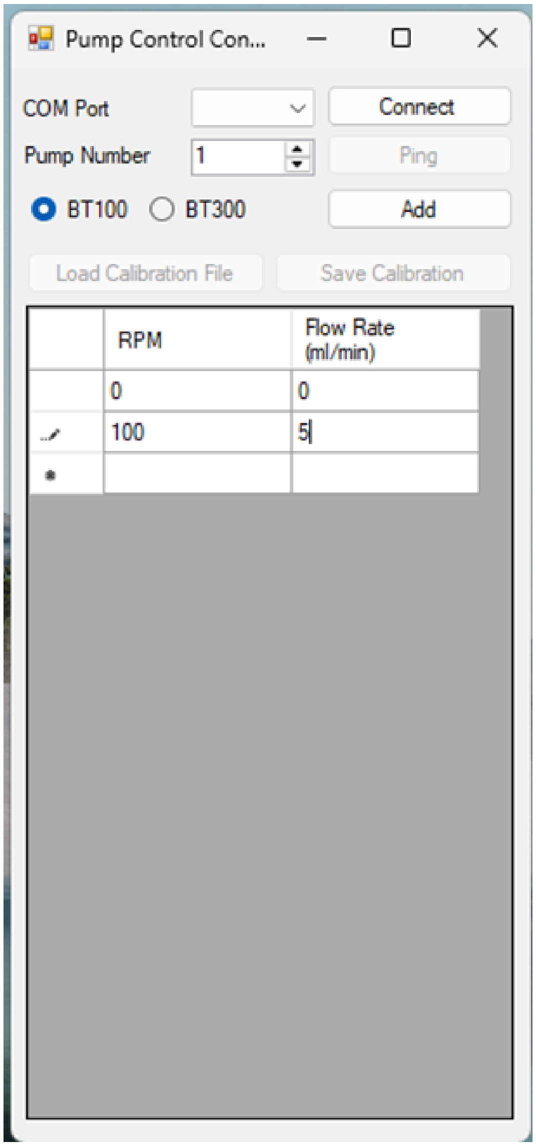

COM Port

Pump Number 1

● BT100 ○ BT300

	RPM	Flow Rate (ml/min)
	0	0
	100	5

Figure 3.9: Pump control subsystem

the pump.

Experiment Control

A manual experiment control screen allows the user to test out the system or its features before starting an automated run. It enables full manual control of the pump(s), fluid source pinch valves, and sourcemeters to have the system carry out any task it could perform during an automated session. This screen is typically used during automated measurement session setup to ensure the first fluid is flushed through with no bubbles in the system.

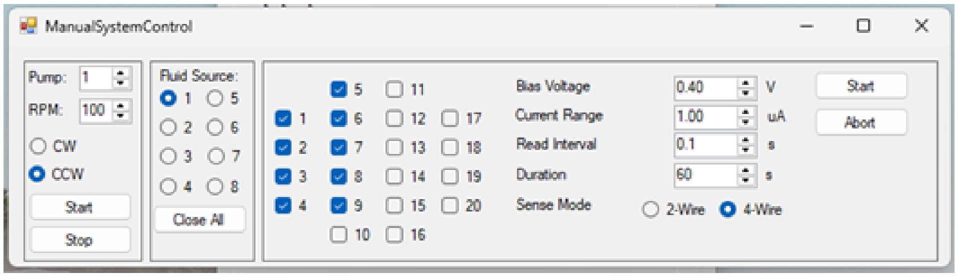

Pump: 1
RPM: 100
○ CW
● CCW

Fluid Source:
● 1 ○ 5
○ 2 ○ 6
○ 3 ○ 7
○ 4 ○ 8

☑ 5 ☐ 11
☑ 1 ☑ 6 ☐ 12 ☐ 17
☑ 2 ☑ 7 ☐ 13 ☐ 18
☑ 3 ☑ 8 ☐ 14 ☐ 19
☑ 4 ☑ 9 ☐ 15 ☐ 20
☐ 10 ☐ 16

Bias Voltage 0.40 V
Current Range 1.00 uA
Read Interval 0.1 s
Duration 60 s
Sense Mode ○ 2-Wire ● 4-Wire

Figure 3.10: Manual system control screen

The true utility of the system, however, lies in the automated measurement protocol functionality. A convenient user interface allows the user to create custom protocols using ‘blocks.’ Examples of blocks are “random source select,” “flush,” “flow,” and “delay,” each corresponding to one or more steps the software would take to implement the block.

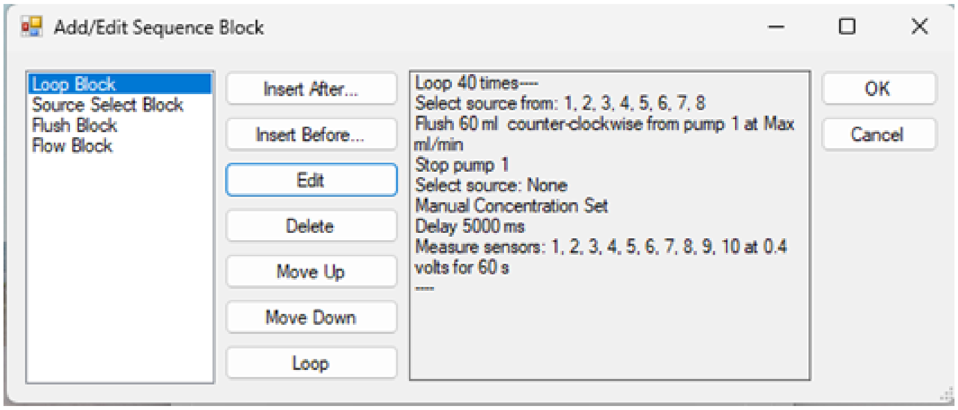

Loop Block
Source Select Block
Flush Block
Flow Block

```
Loop 40 times----
Select source from: 1, 2, 3, 4, 5, 6, 7, 8
Flush 60 ml  counter-clockwise from pump 1 at Max
ml/min
Stop pump 1
Select source: None
Manual Concentration Set
Delay 5000 ms
Measure sensors: 1, 2, 3, 4, 5, 6, 7, 8, 9, 10 at 0.4
volts for 60 s
----
```

Figure 3.11: Automated protocol control

A typical measurement protocol was to make a specified number of measurements, randomly selecting a source for each and inserting a delay between the flush and measurement, and then flushing PBS through the system at the end of the session to avoid the enzyme sitting in a high glucose concentration until the experimenter returned to the bench.

3.6 Performance

The automated measurement system has provided a highly repeatable testing environment for the studies performed in addition to improving data throughput. Some of the data presented later in this document is previewed here as a demonstration of the measurement system's capabilities. Figure 3.12 shows 40 chronoamperometry curves for 6 unique solutions containing glucose and acetaminophen plotted on the same graph, showcasing the repeatability of the system. Each measurement was taken with a randomized source selected from the solutions. Figure 3.13 shows mean chronoamperometry curves for 12 measurements with 3 unique concentrations of hydrogen peroxide. Measurement-to-measurement standard deviation is plotted as a shaded region around each average curve. Table 3.1 summarizes the system's data throughput performance in a typical measurement session when used by a colleague.

Metric	Value
Sensors simultaneously tested	10
Measurements	40 (typical) × 10 sensors = 400
System setup time	30 minutes
Measurement cycle	4 minutes × 40 measurements
Cleanup time	2 minutes
Total time	3.2 hours
Measurement rate	126 measurements/hour

Table 3.1: Data throughput metrics for the automated measurement system

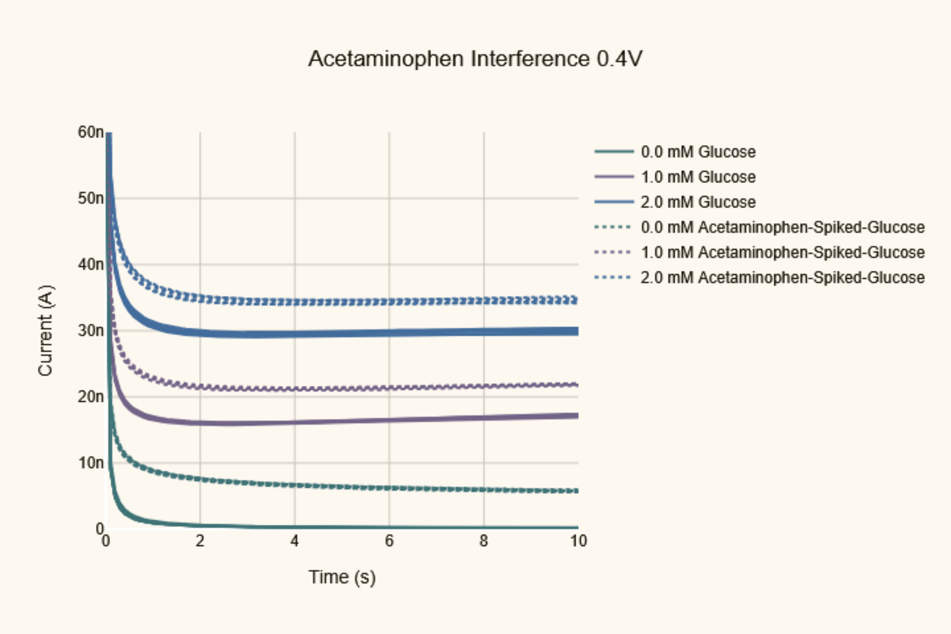

Figure 3.12: Interference data collected using the automated measurement system. A total of 40 curves are plotted here, distributed over six source fluids. All curves are plotted but effectively only one is seen for each source fluid due to the high repeatability of the measurement system.

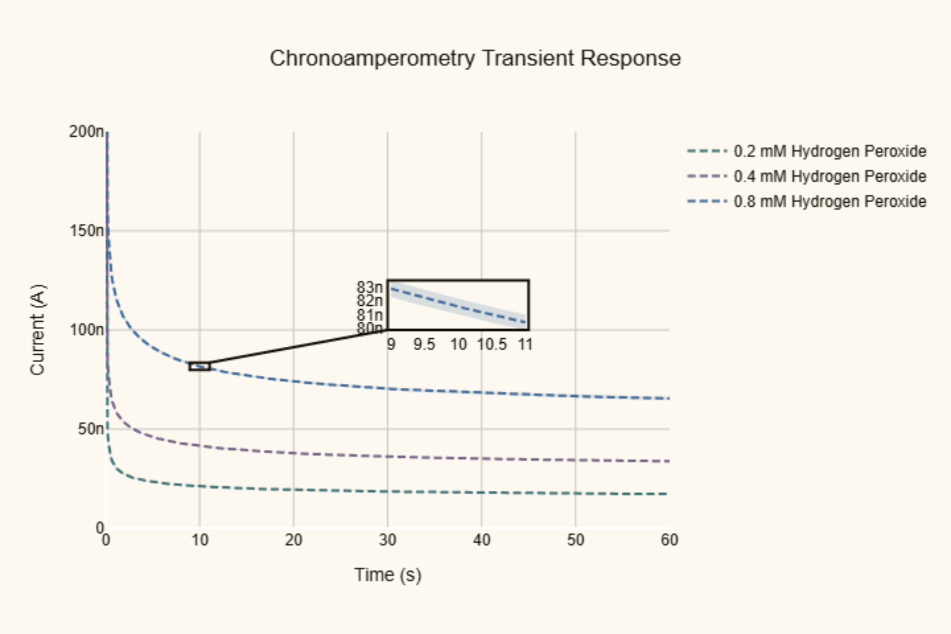

Figure 3.13: The mean of four nonconsecutive chronoamperometry curves in hydrogen peroxide is plotted for each concentration. The solutions were tested in randomized order using random selection without replacement until each concentration had been measured and then starting over. Standard deviation error between measurements is shown as a shaded region. A zoomed-in inset is added so that the error bounds can be seen.

3.7 Discussion and Future Improvements

The automated measurement system enables testing sensors at wafer scale on the substrates on which they were fabricated. This eliminates the need for dicing prior to measurement, enables automated randomized measurement protocols, facilitates exact replication of the testing environment, and improves data throughput. The main labor-intensive tasks at this stage are solution preparation and flow rate calibration, which can be reduced or eliminated via further improvements to the system. An inline flow rate gauge would reduce the need for manual calibration and act as an early warning before peristaltic pump tubing degradation (which, in our experience, appears as a reduction in flow rate at a given RPM before catastrophic failure). The solution preparation bottleneck could be reduced by adding metered solution mixing, but achieving analytical accuracy in such a system was deemed beyond the scope of this implementation. It would also be useful, in the alternative, to expand the total number of source fluids supported by the system (currently between 6 and 8 depending on the service status of the solenoid valves).

This measurement system has enabled the characterization of different sensor architectures and enzyme deposition techniques over short and long time spans [11] [12] [13]. Enabling on-wafer testing immediately after fabrication has the potential to vastly speed up iteration of enzymatic and electrochemical sensor design by eliminating intermediate steps.

References

[1] Noémie Elgrishi et al. "A Practical Beginner's Guide to Cyclic Voltammetry". In: *Journal of Chemical Education* 95.2 (Feb. 13, 2018), pp. 197–206. issn: 0021-9584, 1938-1328. doi: `10.1021/acs.jchemed.7b00361`.

[2] Petr Sedlák and Petr Kuberský. "The Effect of the Orientation towards Analyte Flow on Electrochemical Sensor Performance and Current Fluctuations". In: *Sensors (Basel, Switzerland)* 20.4 (Feb. 14, 2020), p. 1038. issn: 1424-8220. doi: `10.3390/s20041038`. PMID: `32075126`.

[3] ChamarthiMaheswar Raju, Decibel P. Elpa, and Pawel L. Urban. "Automation and Computerization of (Bio)Sensing Systems". In: *ACS Sensors* 9.3 (Feb. 16, 2024), pp. 1033–1048. issn: 2379-3694. doi: `10.1021/acssensors.3c01887`. PMID: `38363106`.

[4] J. Ruzicka and E. H. Hansen. "Flow Injection Analyses: Part I. A New Concept of Fast Continuous Flow Analysis". In: *Analytica Chimica Acta* 78.1 (Aug. 1, 1975), pp. 145–157. issn: 0003-2670. doi: `10.1016/S0003-2670(01)84761-9`.

[5] Jaromir Ruzicka and Graham D. Marshall. “Sequential Injection: A New Concept for Chemical Sensors, Process Analysis and Laboratory Assays”. In: *Analytica Chimica Acta* 237 (Jan. 1, 1990), pp. 329–343. ISSN: 0003-2670. DOI: `10.1016/S0003-2670(00)83937-9`.

[6] Chanyanut Wongsa et al. “Sequential Injection Amperometric System Coupling with Bioreactor for In-Line Glucose Monitoring in Cell Culture Application”. In: *Molecules* 27.19 (Oct. 7, 2022), p. 6665. ISSN: 1420-3049. DOI: `10.3390/molecules27196665`. PMID: `36235202`.

[7] Katrin Pontius et al. “Automated Electrochemical Glucose Biosensor Platform as an Efficient Tool Toward On-Line Fermentation Monitoring: Novel Application Approaches and Insights”. In: *Frontiers in Bioengineering and Biotechnology* 8 (May 21, 2020). ISSN: 2296-4185. DOI: `10.3389/fbioe.2020.00436`.

[8] Lesedi Lebogang et al. “Electrochemical Flow-ELISA for Rapid and Sensitive Determination of Microcystin-LR Using Automated Sequential Injection System”. In: *Sensors* 17.7 (7 July 2017), p. 1639. ISSN: 1424-8220. DOI: `10.3390/s17071639`.

[9] Eva Vargas et al. “Automated Bioanalyzer Based on Amperometric Enzymatic Biosensors for the Determination of Ethanol in Low-Alcohol Beers”. In: *Beverages* 3.2 (2 June 2017), p. 22. ISSN: 2306-5710. DOI: `10.3390/beverages3020022`.

[10] Michael P. McIntyre et al. “Modelling the Pulsatile Flow Rate and Pressure Response of a Roller-Type Peristaltic Pump”. In: *Sensors and Actuators A: Physical* 325 (July 2021), p. 112708. ISSN: 09244247. DOI: `10.1016/j.sna.2021.112708`.

[11] Dvin Artashes-Boghos Adalian. “Development and Dynamics of Microfabricated Enzymatic Biosensors”. PhD thesis. California Institute of Technology, 2019. DOI: `10.7907/7GHS-NX49`.

[12] Dvin Adalian et al. “Patterned Thin Film Enzyme Electrodes via Spincoating and Glutaraldehyde Vapor Crosslinking: Towards Scalable Fabrication of Integrated Sensor-on-CMOS Devices”. In: *Lab on a Chip* 24.17 (2024), pp. 4172–4181. ISSN: 1473-0197, 1473-0189. DOI: `10.1039/D4LC00206G`.

[13] Christin Ahlbrecht. “Entwicklung und Charakterisierung neuartiger Biosensoren”. PhD thesis. Hannover : Institutionelles Repositorium der Leibniz Universitat Hannover, 2023.

Chapter 4

SIMULATION AND EXPERIMENTAL CHARACTERIZATION OF MICROFABRICATED HYDROGEN PEROXIDE SENSORS

4.1 Abstract

Here we present the results of simulations and experimental measurements of microfabricated planar electrodes. An automated measurement system (AMS) flow cell was simulated along with a circular sensor of area $1.8 \times 10^4\, \mu m^2$ placed bottom-center of the flow cell. The dynamics of the sensor and its environment upon sensor turn-on were simulated. A microfabricated electrochemical sensor with a rectangular working electrode of the same area was then tested in the AMS and the practical results compared to simulation. The shape of the measured dynamic response of the rectangular sensor was found to be in reasonably good agreement with the dynamic response of the simulated circular sensor, whereas the magnitude error reduced with increasing mesh fineness and was found to be $< 10\%$ across the wafer for the finest mesh tested.

4.2 Introduction

The transient current at planar electrodes was originally described by Cottrell in the now well-known Cottrell equation[1]:

$$i = \frac{nFAc_0\sqrt{D}}{\sqrt{\pi t}} \tag{4.1}$$

$$= \frac{k}{\sqrt{t}} \tag{4.2}$$

where n is the number of electrons involved in the reaction, F is the Faraday constant ($96,485\ C\ mol^{-1}$), A is the electrode area, c_0 is the initial analyte concentration, and D is the analyte diffusivity. The various constants can also be combined into one constant k. However, this description is for macroscopic planar electrodes and proceeds on the reduction of the problem to one dimension.

Improvements and refinements have been calculated and published over the years[1][2][3] for other electrode geometries as well as for including finite volume effects. Of particular interest to us, for small disk electrodes, the Shoup-Szabo equation provides a de-facto solution with 0.6% theoretical accuracy[3] and 3% accuracy reported[4] compared to empirical measurements.

$$f(\tau) = 0.7854 + 0.8862\tau^{-\frac{1}{2}} + 0.2146e^{-0.7823\tau^{-\frac{1}{2}}} \tag{4.3}$$

Having developed a finite element simulation for simulating various microfabricated enzyme electrodes, as described in Chapter 2, as well as an automated measurement system, as described in Chapter 3, enabling the testing of physical realizations of the same at wafer scale, we applied those tools first to testing the simplest case of an electrochemical sensor containing no enzyme and simply detecting hydrogen peroxide with fixed initial starting concentration. By testing the performance of the simulation and the measurement system with a simpler problem with known solutions, we undergird our confidence in applying these tools to more complex sensor geometries, such as with different enzyme geometries and top coats, especially those that leverage the additional degree of freedom provided by our axisymmetric simulation and might be less amenable to explicit (analytical or numerical) solutions.

4.3 Simulation

Methods

One of the flow cells of the automated measurement system (AMS) described in Chater 3 was simulated. The flow cells have a radius of 1.4 mm and a height of 1.25 mm. A stripped-down version of the simulation described in Chapter 2 was used (no enzyme, glucose, or oxygen was simulated) using a mesh matching the size and shape of the AMS flow cells. A sensor with radius 76 μm was simulated to yield an area of 1.8×10^4 μm^2 to match the working electrode area of the physical sensor.

The "no flux" boundary condition was selected for the outer boundaries to simulate a finite measurement cell. However, experimenting with other boundary conditions revealed that 60 seconds measurement is insufficient time for the boundary conditions to make a difference to the recorded current values, indicating that the simulated flow cell volume is sufficient to avoid finite volume effects.

Time was stepped in 0.1 s increments. An initial concentration of 1.0 mM H_2O_2 was used. Different concentrations weren't simulated as the Diffusion-Reaction Equation is linear in the absence of a reaction term, so the solution for different concentrations would simply be the solution for 1.0 mM multiplied by a scalar. Coarser and more refined versions of the mesh were also tested.

Results

The evolving hydrogen peroxide concentration profile is shown. The diffusion layer grows with near-spherical symmetry around the sensor and snapshots of it are shown at 0.1 s (Figure 4.1), 5.0 s (Figure 4.2), 10.0 s (Figure 4.3), 30.0 s (Figure 4.4), and 60 s (Figure 4.5) after start of chronoamperometry measurement. The color scales have been discretized to 10 color steps for easier visualization from one time point to another.

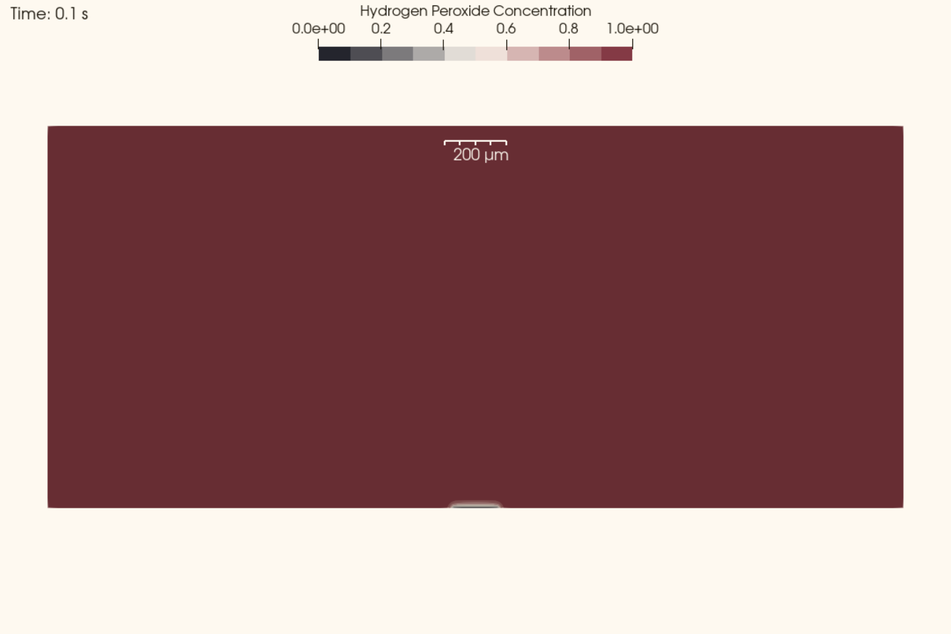

Figure 4.1: H_2O_2 concentration at 0.1 s. The sensor has just begun consuming hydrogen peroxide, seen as the small black area immediately above the sensor surface (center-bottom).

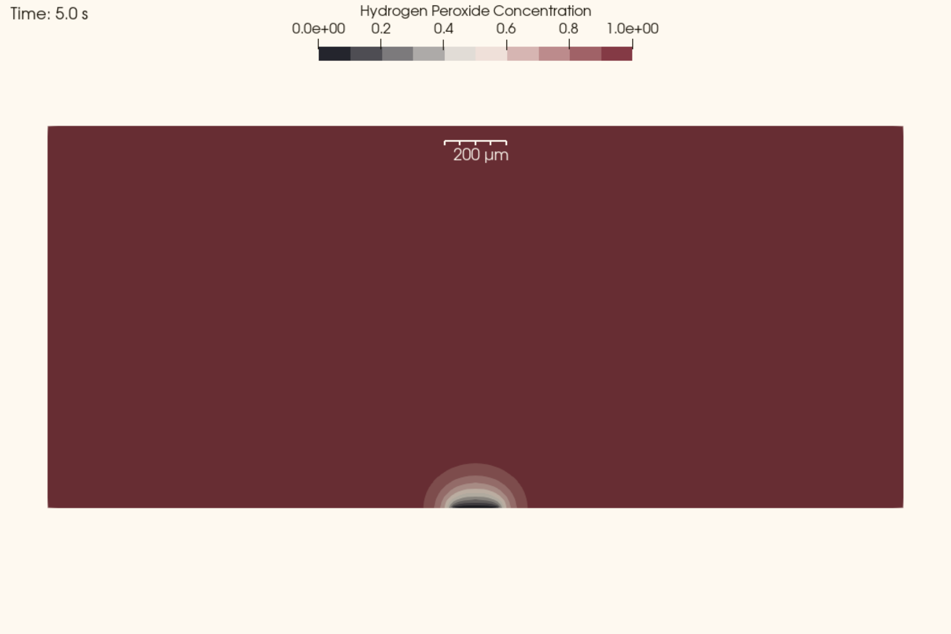

Figure 4.2: H_2O_2 concentration at 5.0 s. The diffusion layer begins to grow with close to shperical symmetry.

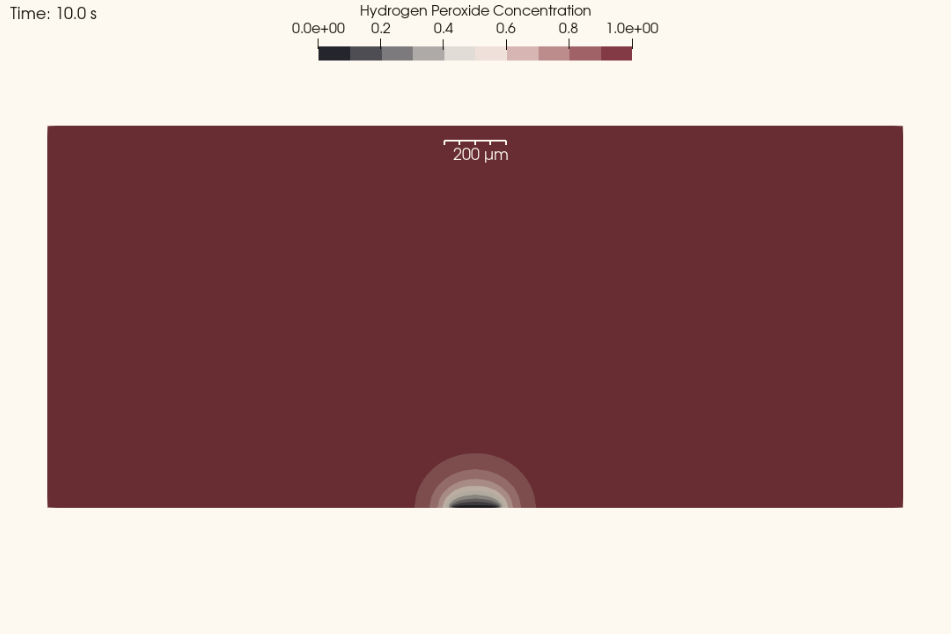

Figure 4.3: H_2O_2 concentration at 10.0 s. The diffusion region expands further.

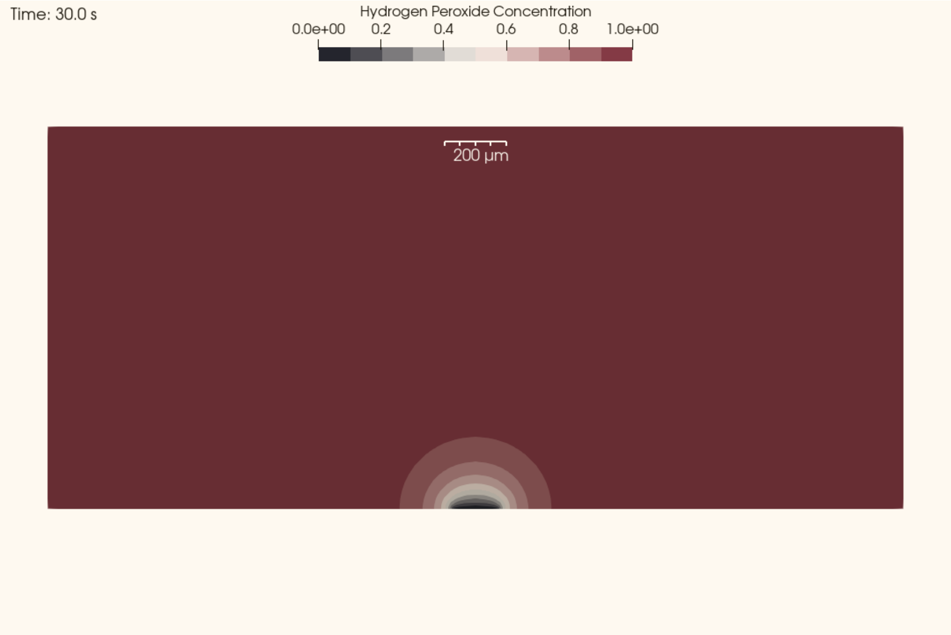

Figure 4.4: H_2O_2 concentration at 30.0 s. The rate of growth of the diffusion region has slowed down at this stage.

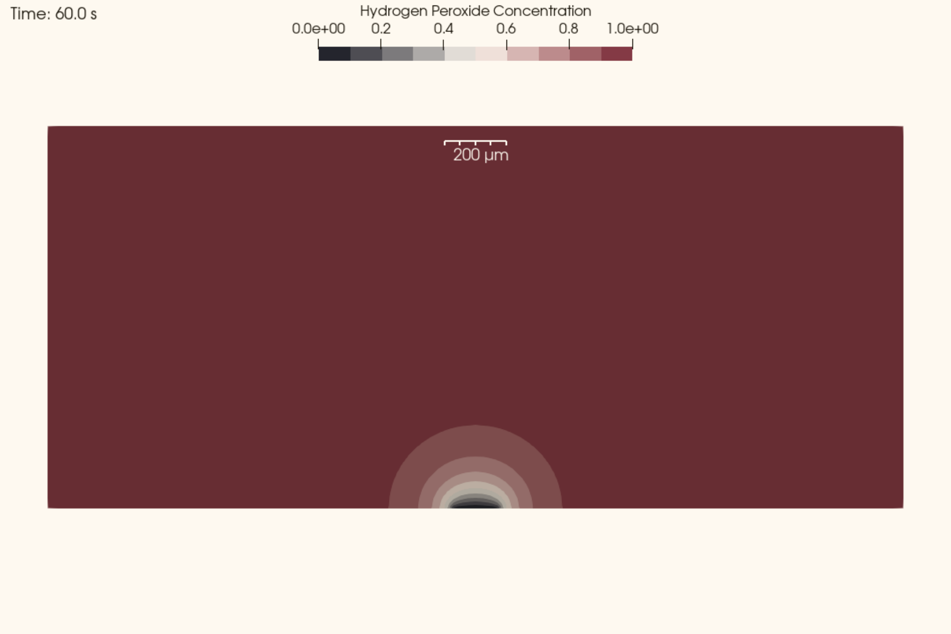

Figure 4.5: H_2O_2 concentration at 60.0 s. This is the final diffusion region in a 60 s measurement.

The dynamic response was calculated by multiplying the total normal flux into the sensor by the using the relationship $i = n \times F \times$ flow rate where n is the number of electrons involved in the reaction (2), F the Faraday constant (96,485 $C\ mol^{-}1$), and flow rate the area integral of the simulated flux over the sensor. It was found to agree highly with the Shoup-Szabo equation (Figure 4.6).

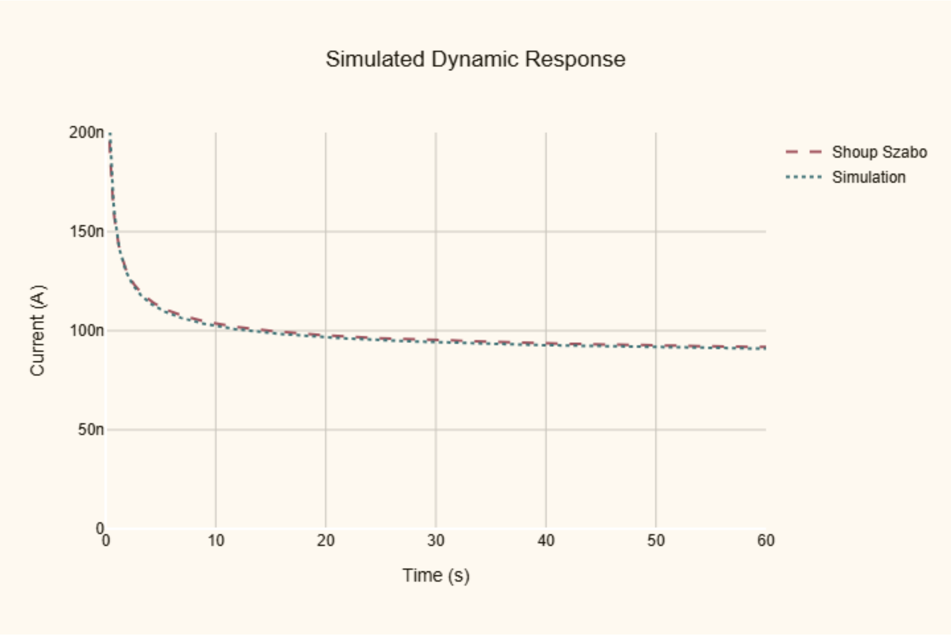

Figure 4.6: The simulated dynamic response at 1.0 mM H_2O_2 (green, dotted) compared to the Shoup-Szabo equation (red, dashed). Other concentrations would result in this curve multiplied by a scalar.

4.4 Experimental Characterization

Methods

The electrochemical sensors used here were described in detail previously by Adalian [5]. They employ a three-electrode setup with a working electrode (WE), a counter electrode (CE), and a reference electrode (RE). All three are made of platinum, which is deposited using electron beam evaporation. The wafer area outside the platinum electrodes is insulated with silicon oxide/silicon nitride. The working electrode area is 0.018 mm^2 enclosed by an RE and CE within a total area of $500\mu m \times 500\mu m$. WE is held at a potential of $0.4V$ relative to RE.

Hydrogen peroxide solutions were made in 1× phosphate buffered saline (PBS) immediately prior to measurement. The wafer under test was aligned and seated in the automated measurement system described in Chapter 3. Hydrogen peroxide concentrations were cycled through in random order. 60 ml of each concentration was flowed through the measurement system before turning off flow and waiting 5 s to the system to stabilize.

After the 5 s stabilization time, chronoamperometry was performed at 0.4 V vs. the platinum reference electrode while maintaining static conditions. Each measurement was performed for 60 s with current samples taken every 0.1 s. Ten sensors were tested but measurements for one were excluded due to poor electrical contact.

Results

The measured dynamic responses showed a high degree of consistency measurement-to-measurement for the same sensor, indicating low sensor drift. Four of the nine sensors had nearly identical responses to each other whereas the other five showed sensor-to-sensor variation. Cross-wafer statistics are summarized in Table 4.1. The recorded chronoamperometry curves for one of the sensors is provided in Figure 4.7, showing its measurement-to-measurement consistency. For each curve shown, standard deviation error over four nonconsecutive measurements (with the other concentrations measured in between) is represented by a shaded region around the curve.

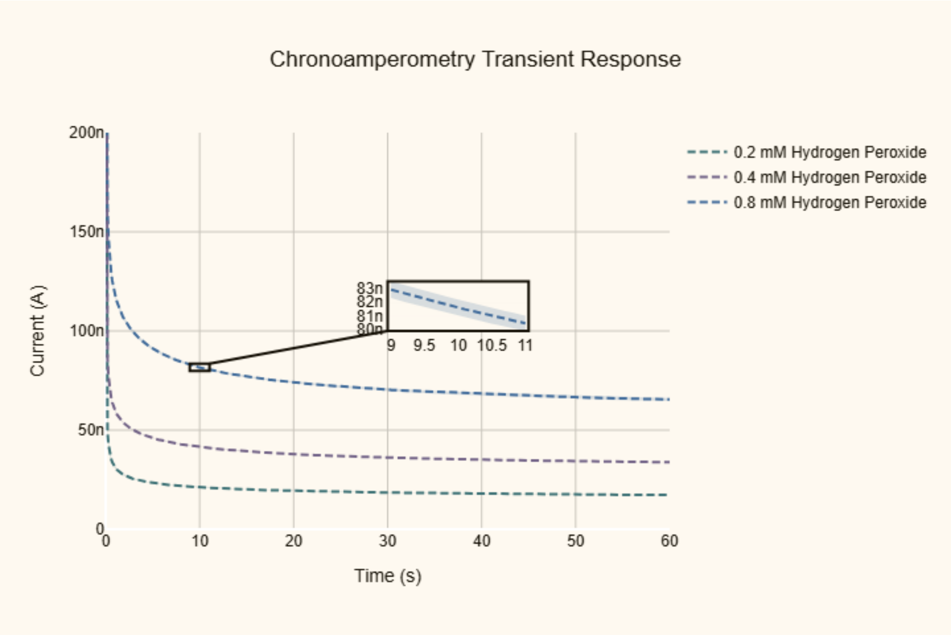

Figure 4.7: The measured dynamic response of one of the sensors at 0.2, 0.4, and 0.8 mM H_2O_2. Zoomed-in inset shows standard deviation error over four measurements at 0.8 mM.

The sensitivity, of course, depends on the time at which the current is sampled, due to the nature of the dynamic response seen in Figure 4.7. Linear fits were done at selected time points between 1.0 and 60.0 s and the sensors had good linearity regardless of the point in the dynamic response where current was sampled. The linear fit for a sensor at 60.0 s is shown in Figure 4.8.

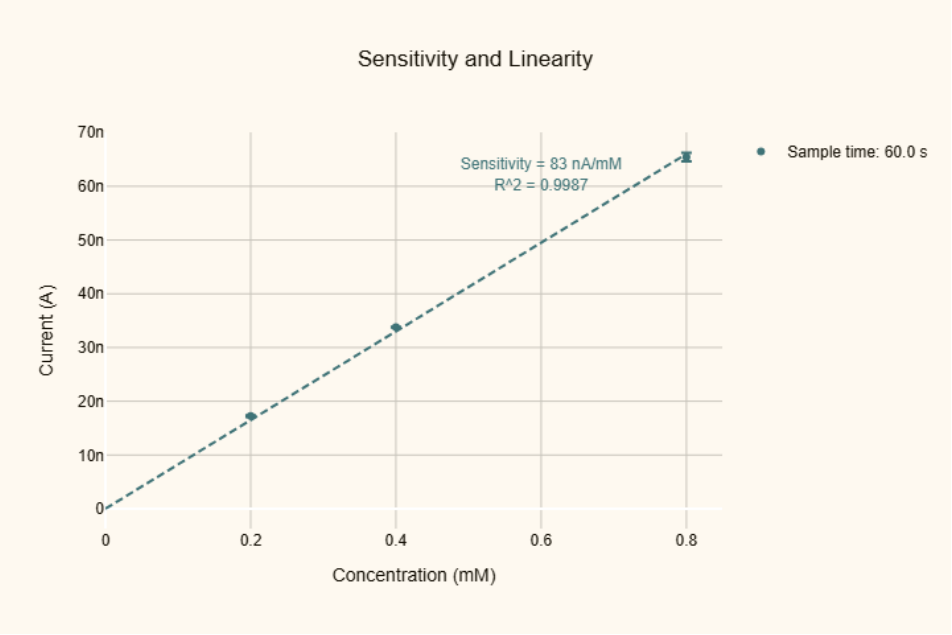

Figure 4.8: The measured sensitivity and linearity of one of the measured sensors. Standard deviation error bars are shown (across four measurements at each concentration).

Parameter	Mean	Standard Deviation
Sensitivity @ 60.0 s	102 $\mathrm{nAmM^{-1}}$	18 $\mathrm{nAmM^{-1}}$
R^2 @ 60.0 s	0.9980	0.0010

Table 4.1: Sensitivity and linearity parameter statistics across the 9 sensors tested.

4.5 Comparison of Simulated and Experimental Results

The measured dynamic response was in good agreement with the simulation for four of the nine sensors tested whereas for the other five, the shape was in good agreement but there was disagreement in the magnitude due to the sensor-to-sensor variation mentioned in the previous section (and summarized in Table 4.1). In assessing the goodness of fit with experimental data, we keep in mind that a practical electrode may deviate from the ideality assumptions inherent in the simulation or have fabrication errors affecting available electrode area. Figure 4.9 shows the comparison of the simulated and measured responses of one of the sensors tested.

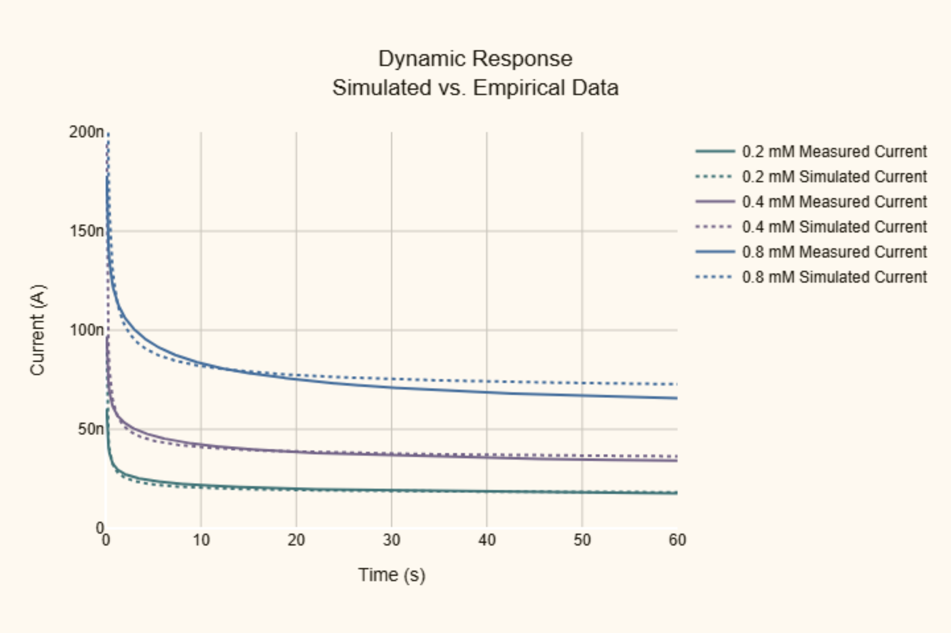

Figure 4.9: The measured dynamic response (solid) compared to the simulated dynamic response (dotted) for 0.2, 0.4, and 0.8 mM H_2O_2 (green, purple, and blue respectively) for one of the sensors tested.

4.6 Discussion

The results of the finite element analysis simulation correspond extremely tightly to the de-facto solution provided by Shoup and Szabo [3] (Equation 4.3, Figure 4.6). They also show good agreement with the transient response of practical sensors measured empirically (cross-wafer variation notwithstanding), with some error likely due to deviations from ideality of the sensors tested. This gives us confidence in applying these tools to more complex sensor geometries and constructions.

References

[1] Jan C Myland and Keith B Oldham. “Cottrell’s Equation Revisited: An Intuitive, but Unreliable, Novel Approach to the Tracking of Electrochemical Diffusion”. In: *Electrochemistry Communications* 6.4 (Apr. 1, 2004), pp. 344–350. ISSN: 1388-2481. DOI: `10.1016/j.elecom.2004.01.013`.

[2] Narottam P. Bansal and James A. Plambeck. “An Aid to the Interpretation of Electrochemical Data Measured with Spherical and Cylindrical Electrodes: Corrections to the Cottrell Equation”. In: *Canadian Journal of Chemistry*

56.2 (Jan. 15, 1978), pp. 155–156. ISSN: 0008-4042, 1480-3291. DOI: `10.1139/v78-024`.

[3] David Shoup and Attila Szabo. “Chronoamperometric Current at Finite Disk Electrodes”. In: *Journal of Electroanalytical Chemistry and Interfacial Electrochemistry* 140.2 (Nov. 23, 1982), pp. 237–245. ISSN: 0022-0728. DOI: `10.1016/0022-0728(82)85171-1`.

[4] Haruko Ikeuchi. “Accuracy of Theoretical Equations for Diffusion Currents at a Disk Electrode”. In: *Journal of Electroanalytical Chemistry* 577.1 (Mar. 2005), pp. 55–58. ISSN: 15726657. DOI: `10.1016/j.jelechem.2004.11.013`.

[5] Dvin Artashes-Boghos Adalian. “Development and Dynamics of Microfabricated Enzymatic Biosensors”. PhD thesis. California Institute of Technology, 2019. DOI: `10.7907/7GHS-NX49`.

Chapter 5

SIMULATION OF MICROFABRICATED GLUCOSE SENSORS AND EMPIRICAL VALIDATION

5.1 Abstract

In this chapter, we apply the simulations described in Chapter 2 to consider the impact of hydrogel geometry and enzyme loading on sensor performance, and carry out empirical validation of the results considering the impact of hydrogel geometry. We simulate thin and thick (2.2 μm and 47 μm) enzyme-containing hydrogels on top of the sensor. We also explore the impact of patterning the enzyme layer to cover only the active electrode areas vs. leaving the enzyme unpatterned, covering the wafer as a whole. Empirical validation was carried out by comparing measurements from spin-coated sensors using a technique we have found to produce layers as thin as 500 nm at the highest spin speeds, and conventional drop-coated sensors, which produce thicker coatings. The simulated geometries are thicker than the profilometer measurements of dry hydrogel primarily to account for hydrogel swelling upon wetting, which hydrophilic albumin-based hydrogels are particularly prone to.

5.2 Introduction

In Chapter 2, we looked at the development of an axisymmetric finite element simulation enabling the mathematical modeling of enzyme electrodes and their liquid environment. The goal of developing these simulation tools was to help understand the empirically-observed behavior of enzyme electrodes fabricated by our group and guide the future effort towards predictive and deterministic design. In Chapter 3, we looked at the development of an automated measurement system to enable wafer-scale measurements, and in Chapter 4 an initial look at applying these tools to basic hydrogen peroxide sensors. Now we look at the application of these tools to the more complex glucose sensors, combining theoretical study with empirical testing. We shall modify the simulation parameters to suit the sensors tested and compare simulation results to the observed empirical ones. In particular, we shall take a second look at the modification of enzyme kinetic constants, which are strongly dependent on pH [1] and were originally measured at glucose oxidase's optimal pH of 5.5 [2].

5.3 Geometries Simulated

The sensors we developed and tested contain glucose oxidase (GOx) immobilized in a hydrogel comprised, in addition to the GOx, of bovine serum albumin crosslinked with glutaraldehyde. Such hydrogels have been reported to have a swelling ratio of up to around 4x (weight/weight) at netural pH [3]. Work by our group has found spin-coating to have the ability to produce layers as thin as 300-500 nm, measured when dry [4, 5]. While exact thickness of the wet hydrogel proved difficult to measure, we use the 2.2 μm enzyme thickness run from our thickness sweep as the illustrative example here. (Thicknesses were swept as 1.0 μm, 2.2 μm, 4.7 μm, 10 μm, and so on, to have three points per decade.)

The geometries of drop-coated sensors were even more difficult to measure owing to their irregular shape and uneven thickness over the sensor surface. They were also significantly more variable in thickness than spin-coated sensors due to the criticality of the time between mixing and depositing, as mixing together the composite chemicals begins the crosslinking process. We use the 47μm thickness simulation as illustrative. Due to the high degree of swelling assumed, we also adjust the solute partitioning ratio to 0.9.

In addition to varying the hydrogel thicknesses, we also varied the simulated widths of each hydrogel. While drop-coated sensors were not patterned, spin-coated sensors were optionally patterned by being preceded by lithography and followed by acetone liftoff.

pH Correction of Enzyme Kinetics

We presented a first look at the two-substrate enzyme kinetics of glucose oxidase in Chapter 2 but did not discuss the modification of kinetic parameters to their expected values at pH 7.4. To recap, the two-substrate mechnism determined by Gibson et al. is [2]:

$$\begin{aligned} E_O + G &\xrightarrow{k_1} E_R\text{-}P_1 \xrightarrow{k_2} E_R + \delta\text{-lactone} \\ E_R + O_2 &\xrightarrow{k_3} E_O - P_2 \xrightarrow{k_4} E_O + H_2O_2 \end{aligned} \tag{5.1}$$

With velocity equation:

$$\frac{1}{v} = \frac{k_2 + k_4}{k_2 k_4} + \frac{1}{k_1 c_g} + \frac{1}{k_3 c_{O_2}} \tag{5.2}$$

Kinetic parameters:

$$v_{max} = \frac{k_2 k_4}{k_2 + k_4} \tag{5.3}$$

$$K_G = \frac{v_{max}}{k_1} \tag{5.4}$$

$$K_{O_2} = \frac{v_{max}}{k_3} \tag{5.5}$$

And the two-substrate Michaelis-Menten kinetics equation:

$$V = V_{max} \frac{[G][O_2]}{K_{O_2}[G] + K_G[O_2] + [G][O_2]} \tag{5.6}$$

Where:

$$V_{max} = [E] v_{max} \tag{5.7}$$

While in the illustrative simulation we use Gbison's kinetic parameters measured at pH 5.6, the sensors we plan to test will be tested in phosphate buffered saline at pH 7.4, so we shall adapt these parameters to that pH. Weibel and Bright used effectively the following reaction mechanism in their study [1]:

$$E_O + G \xrightarrow{k_{red}} E_B \xrightarrow{k_{cat}} E_R + \delta\text{-lactone} \tag{5.8}$$

$$E_R + O_2 \xrightarrow{k_{ox}} E_O + H_2O_2 \tag{5.9}$$

Although this mechanism is missing the second step in the second reaction according to Gibson, that last step is not the limiting step and we can compare these rate constants to the rate constants of Gibson et al. Effectively, k_{red} and k_{ox} are approximately equivalent to k_1 and k_3 respectively [6]. Therefore, with this model, our kinetic parameters become:

$$v_{max} = k_{cat} \tag{5.10}$$

$$K_G = \frac{v_{max}}{k_{red}} \tag{5.11}$$

$$K_{O_2} = \frac{v_{max}}{k_{ox}} \tag{5.12}$$

Graphically interpolating Weibel and Bright's published data, we estimate at pH 7.4 (the pH maintained by the PBS buffer used in our in vitro studies) that $k_{cat} = 850 s^{-1}$, $k_{red} = 12,000\ M^{-1}s^{-1}$,and $k_{ox} = 1 \times 10^6\ M^{-1}s^{-1}$. These rate constants evaluate approximately to $K_G = 71\ mM$, and $K_{O_2} = 0.85\ mM$. We note here that at pH 7.4, k_{ox} has a sharp slope and has a larger uncertainty associated with it due to the compounding of uncertainty in the original data and possible interpolation error.

Parameter	Description	Value
V_{max}	Maximum enzymatic reaction rate per unit volume	100 mMs^{-1}
K_G	Michaelis constant with respect to glucose	71 mM
K_{O_2}	Michaelis constant with respect to oxygen	850 μM
D_G	Glucose diffusivity in water	$7.20 \times 10^{-10}\ m^2s^{-1}$
D_{O_2}	Oxygen diffusivity in water	$1.93 \times 10^{-9}\ m^2s^{-1}$
$D_{H_2O_2}$	Hydrogen peroxide diffusivity in water	$1.43 \times 10^{-9}\ m^2s^{-1}$
$\alpha_{H_2O_2}$	Partition coefficient for H_2O_2	0.9
α_{O_2}	Partition coefficient for O_2	0.9
$\alpha_{Glucose}$	Partition coefficient for glucose	0.9
$\beta_{H_2O_2}$	Relative diffusion coefficient for H_2O_2	0.2
β_{O_2}	Relative diffusion coefficient for O_2	0.2
$\beta_{Glucose}$	Relative diffusion coefficient for glucose	0.06
r_s	Sensor radius	66 μm
r_e	Enzyme radius	300 μm
h_e	Enzyme height	$2.2 - 47\ \mu m$
t_{on}	Time at which sensor is turned on	30 s
t_{dur}	Measurement duration	60 s
c_G	Bulk glucose concentration	$0.47 - 10\ mM$
c_{O_2}	Bulk oxygen concentration	260 μM

Table 5.1: Parameters used for simulation study.

5.4 Thickness Sweep Results

Two types of thickness sweeps were done, one for "wide" hydrogel layers, where the sensor and its surrounding wafer surface are completely covered with hydrogel, and one for "patterned" hydrogel layers, where the enzyme is limited to a 300 μm radius around the working electrode. For both types of hydrogel layers, the thickness played the dominant role in determining response settling time, being significantly slower for the thick layer than for the thin layers. The chronoamperometry curves for a simulated concentration of 4.7 mM are shown in Figure 5.1 for the wide-type hydrogels and Figure 5.2 for the patterned-type hydrogels.

Additionally, the thick layer for each type showed lower currents than the thin layer for each type, despite the greater total quantity of enzyme. The comparison for the two thicknesses of wide type hydrogels is shown in Figure 5.3, and of the patterned type in Figure 5.4.

We also show the final hydrogen peroxide concentration profiles for the thin and thick wide-type sensors in figures 5.5 and 5.6 respectively.

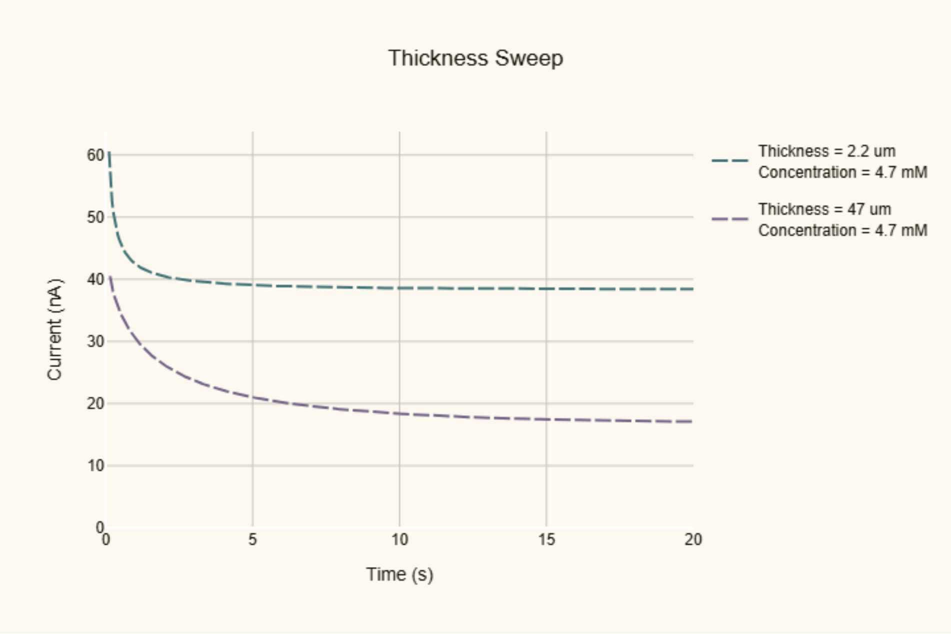

Figure 5.1: Chronoamperometry simulation of "wide" hydrogel layers of thickness 2.2 and 4.7 $\mu\ m$ at 4.7 mM concentration.

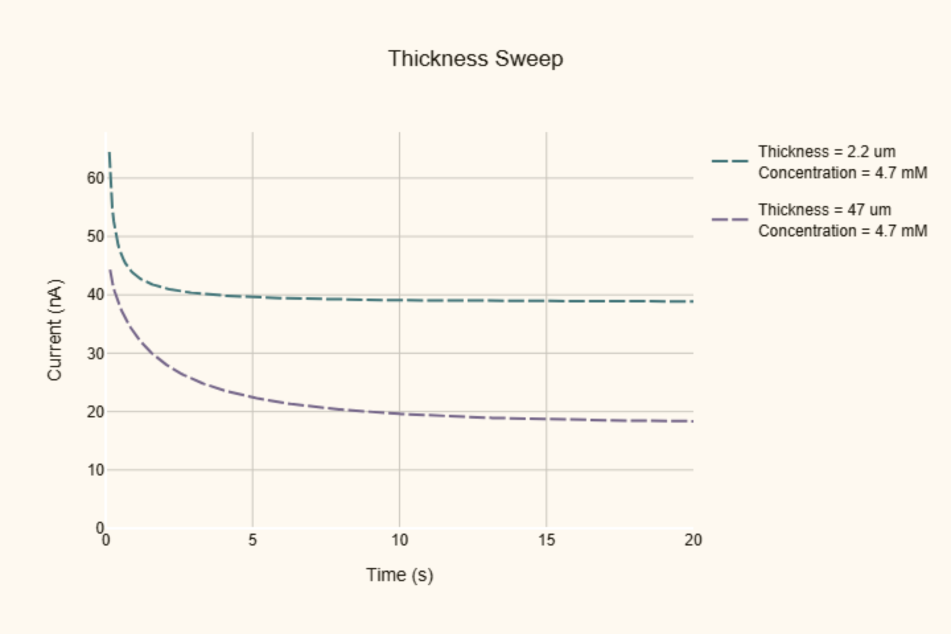

Figure 5.2: Chronoamperometry simulation of "patterned" hydrogel layers of thickness 2.2 and 4.7 μm at 4.7 mM concentration.

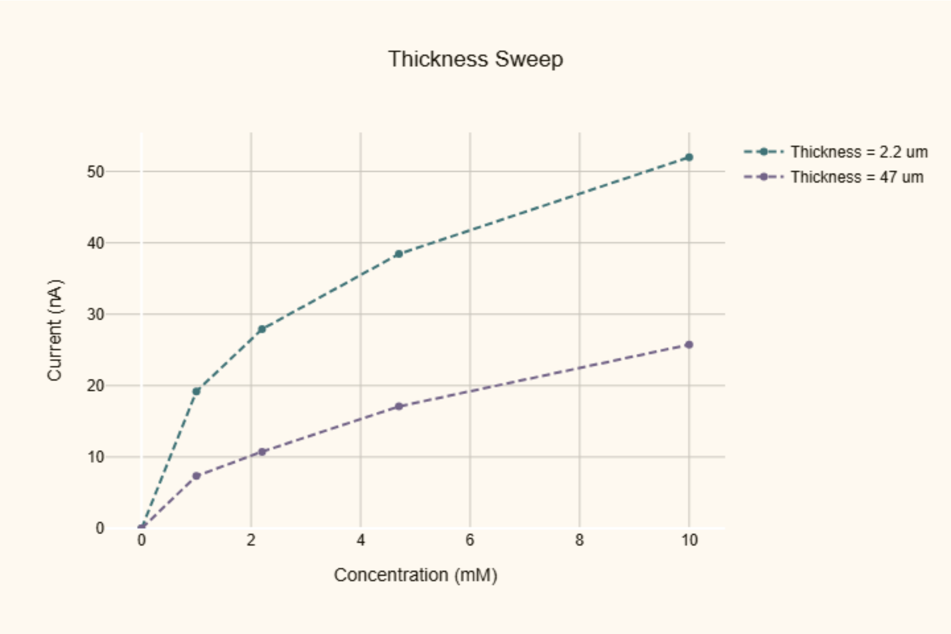

Figure 5.3: Concentration-current curves for the simulated wide hydrogels. The thick hydrogel produces lower currents (purple) than the thin hydrogel (green).

Figure 5.4: Concentration-current curves for the simulated patterned hydrogels. The thick hydrogel produces lower currents (purple) than the thin hydrogel (green).

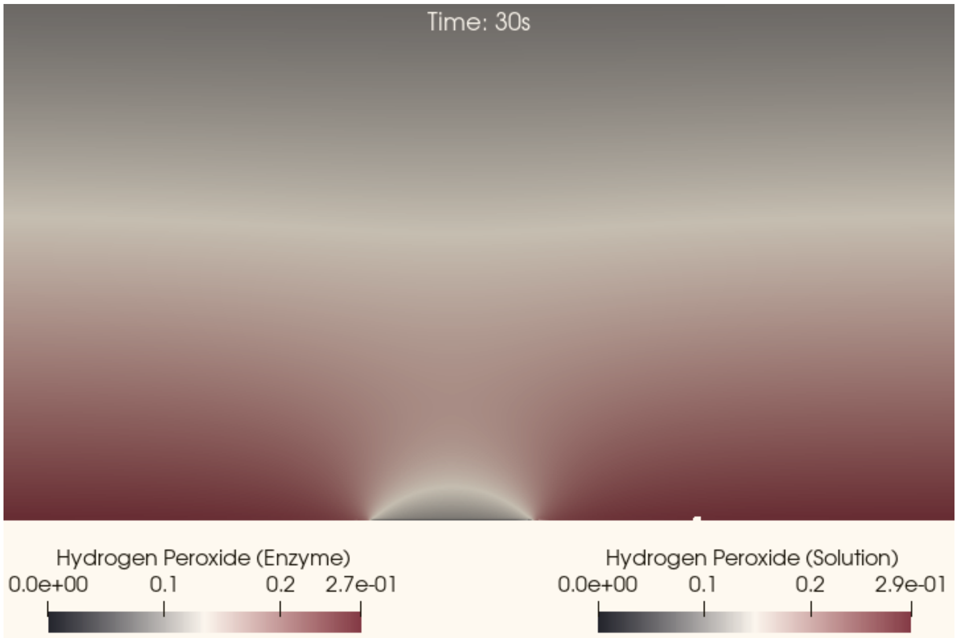

Figure 5.5: Final hydrogen peroxide concentration profile of thin enzyme-containing hydrogel.

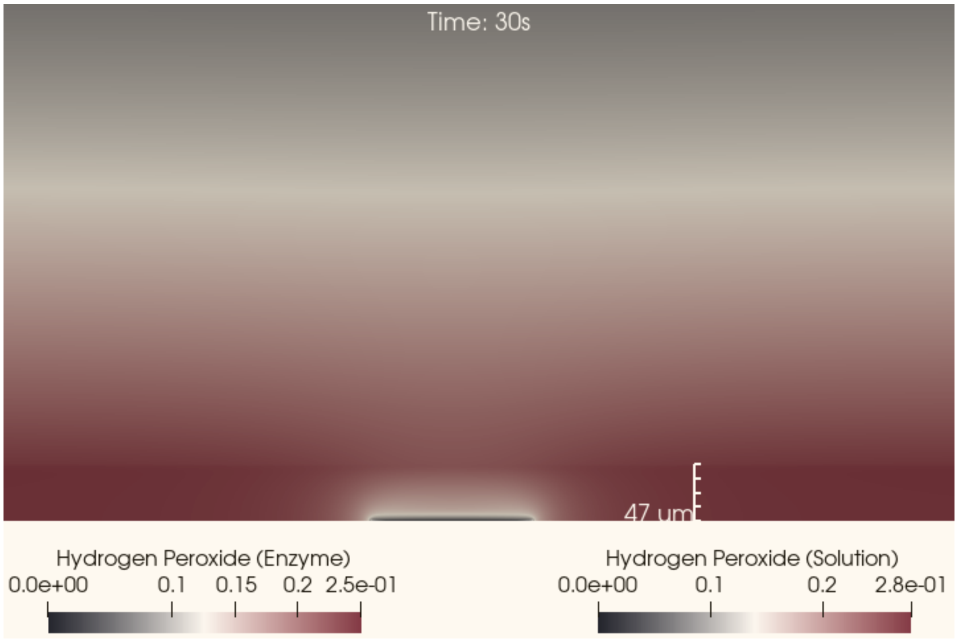

Figure 5.6: Final hydrogen peroxide concentration profile of thick enzyme-containing hydrogel.

5.5 Experimental Methods

Materials

Glucose oxidase from Aspergillus niger was obtained from BBI Solutions (#GO3A). Bovine serum albumin (AMRESCO #97064-340), molecular biology grade 10× phosphate buffer saline (Corning #46-013-CM), d-(+) glucose (Sigma #G8270), and 25% electron microscopy grade glutaraldehyde (ACROS #23328) were purchased from VWR. 99.0% sodium benzoate (ACROS #AC148980010) was purchased from Fisher Scientific. PBS solutions were diluted to 1× concentration using deionized water filtered through 0.22 μm pores (Durapore #CVDI02TPE) and UV sterilized.

Fabrication of Drop-Coated Enzyme Sensors (Type 0)

As described in previously published work [5], a 20 μl GOx-BSA solution consisting of 1.6 mg GOx and 1.3 mg BSA in 1x PBS was vortexed for 15 s and then centrifuged for 15 s. Then 25% glutaraldehyde was diluted 10:1 with 1× PBS. Then 2 μl glutaraldehyde was mixed with 6 μl of the GOx-BSA solution. Since this step begins the crosslinking process, the rest of the deposition was carried out expeditiously. The mixture was vortexed for 5 s and centrifuged for 5 s and 1 μl of the mixture was pipetted onto each sensor.

Fabrication of Spin-Coated Enzyme Sensors (Type 1)

As described in previously-published work [5], 0.56 g GOx and 0.47 g BSA were dissolved in 7 ml 1x PBS. The enzyme solution was vortexed for 30 s and centrifuged for 1 min before being passed through a 0.22 μm filter. An open container of glutaraldehyde was placed inside a bell jar on a hot plate heated to 80 °C to prepare for vapor deposition after spin coating. The filtered solution was dispensed onto the wafer and spin-coated at 500 RPM for 10 s followed by 4000 RPM for 30 s. The coated wafer was then placed on a thermally insulating wooden block inside the bell jar containing the open container of glutaraldehyde and coated for 7.5 minutes to complete the crosslinking process. The wafer was left to stand for 30 minutes before further handling.

Sensor Characterization

Glucose solutions were mixed to their final concentrations and stabilized with 1 gl^{-1} sodium benzoate at least three hours prior to testing to allow for mutarotation equilibrium. All sensors were tested in the automated measurement system described previously. The system cycled through all the concentrations being tested in random order. 60 ml of each solution was flowed at the maximum flow rate to flush the flow cells and then flow was stopped and the system was kept steady for 5 s. This allowed the analytes to diffuse into the enzyme layer and form the product so we could measure the sensor turn-on dynamics after product had already been allowed to form and diffuse into the sensor environment.

After the 5 s stabilization time, the working electrode was biased to the measurement potential (0.4 V vs. platinum reference electrode). Bias was kept on for 60 s for each measurement and current sampled every 0.1 s.

5.6 Experimental Results

The measured currents showed the same trends as the simulated results, both for current magnitude and for response settling time. The drop-coated sensors showed high variability sensor-to-sensor in their settling time, which is to be expected as the coating geometry had high variability too. To illustrate the difference in settling times, the currents for each type of sensor were normalized to the 60-second settling current and averaged over nine sensors of each type. This data has previously appeared in published work [5] and is reproduced here.

Figure 5.7 shows the settling times across five sensors of each type. The current for each measurement is normalized to its final value to show the shape of the transient response. Figure 5.8 shows the concentration-current behavior, also across five sensors of each type. The thicker drop-coated sensors exhibit lower currents than the thinner spin-coated sensors.

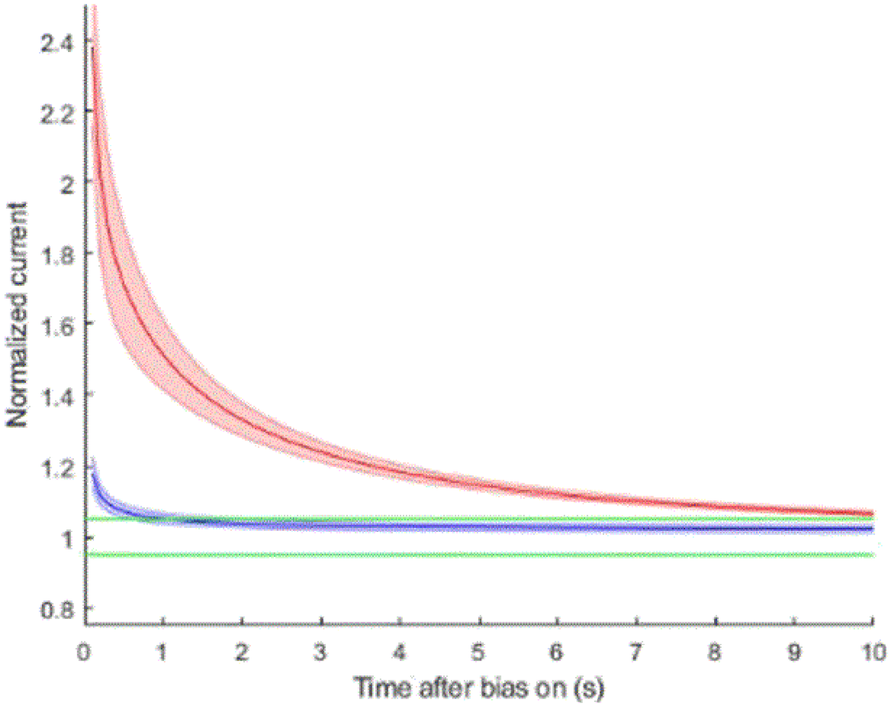

Figure 5.7: Settling times across five thick hydrogel drop-coated sensors (red) and five thin hydrogel spin-coated sensors (blue). The currents are normalized to the final measured current at 60 s. The green horizontal lines represent 5% deviation from the final current value. Reproduced from previous work [5].

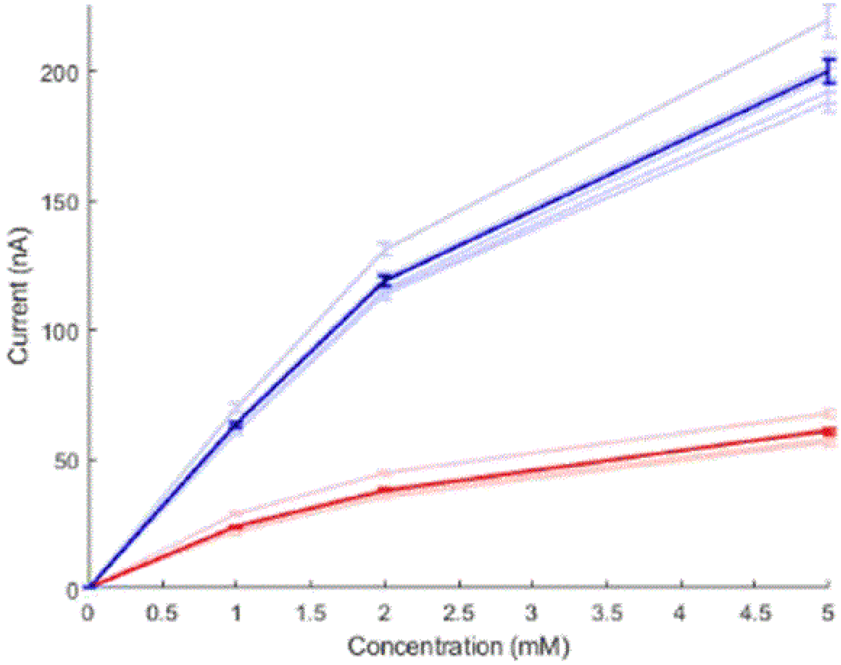

Figure 5.8: Final (60 s) currents across five thick hydrogel drop-coated (red) and five thin hydrogel spin-coated (blue) sensors. The dark lines show an average of each sensor type's behavior whereas the faint lines show the data for each individual sensor. Reproduced from previous work [5].

5.7 Discussion

This practical application of the simulation tools developed allows us to have a better understanding of the factors at play in the overall performance if microfabricated enzyme electrodes. It explains observed experimental results pertaining both to the long-duration or steady-state behavior and to the short-duration transient behavior. Coupled with wafer-scale microfabrication enabling the production of substantively identical biosensors and wafer-scale automated testing allowing the observation of many sensors at a time in identical and reproducible conditions, we believe we demonstrate a potent set of tools for enzyme electrode design, fabrication, testing, and iteration.

More specifically to the research question addressed by this set of simulations and experiments, the demonstration that thin spin-coated enzyme layers produce sensors with higher currents and fast settling times compared to thick enzyme layers deposited via other methods is a vital one in the design of low power intermittently-on implantable biosensors. In addition to the cross-wafer consistency that can be accomplished via refinement of the spin-coating process, the thinner layers so produced provide tangible performance benefits for the final application. These findings and their theoretical basis represent a key milestone on the path to miniaturization and a major step towards the goal of a fully wireless low-power implantable electrochemical biosensing platform.

References

[1] Michael K. Weibel and Harold J. Bright. “The Glucose Oxidase Mechanism”. In: *Journal of Biological Chemistry* 246.9 (May 1971), pp. 2734–2744. ISSN: 0021-9258. DOI: `10.1016/s0021-9258(18)62246-x`.

[2] Quentin H. Gibson, Bennett E.P. Swoboda, and Vincent Massey. “Kinetics and Mechanism of Action of Glucose Oxidase”. In: *Journal of Biological Chemistry* 239.11 (Nov. 1964), pp. 3927–3934. ISSN: 00219258. DOI: `10.1016/S0021-9258(18)91224-X`.

[3] Michael F. Butler, Allan H. Clark, and Sarah Adams. “Swelling and Mechanical Properties of Biopolymer Hydrogels Containing Chitosan and Bovine Serum Albumin”. In: *Biomacromolecules* 7.11 (Nov. 1, 2006), pp. 2961–2970. ISSN: 1525-7797, 1526-4602. DOI: `10.1021/bm060133y`.

[4] Dvin Artashes-Boghos Adalian. “Development and Dynamics of Microfabricated Enzymatic Biosensors”. PhD thesis. California Institute of Technology, 2019. DOI: `10.7907/7GHS-NX49`.

[5] Dvin Adalian et al. “Patterned Thin Film Enzyme Electrodes via Spincoating and Glutaraldehyde Vapor Crosslinking: Towards Scalable Fabrication of Integrated Sensor-on-CMOS Devices”. In: *Lab on a Chip* 24.17 (2024), pp. 4172–4181. ISSN: 1473-0197, 1473-0189. DOI: `10.1039/D4LC00206G`.

[6] J. W. Parker and C. S. Schwartz. “Modeling the Kinetics of Immobilized Glucose Oxidase”. In: *Biotechnology and Bioengineering* 30.6 (Oct. 20, 1987), pp. 724–735. ISSN: 0006-3592, 1097-0290. DOI: `10.1002/bit.260300605`.

Chapter 6

CHEMICAL AND ELECTROCHEMICAL INTERFERENCE

6.1 Overview

Interference with oxidase-based biosensors by electrochemically active compounds is well documented. Two compounds of particular interest are acetaminophen (the common antipyretic and analgesic drug [1]) and ascorbic acid (Vitamin C), due to their electrochemical activity[1, 2, 3, 4, 5] and common presence in the human body. We studied interference with our sensors by both acetaminophen and ascorbic acid.

Acetaminophen is expected to increase sensor current (which would correspond to an erroneously high glucose reading) in the potential range typically used to detect hydrogen peroxide in implanted CGMs[5]. We found the expected increase at a measurement voltage of 0.4 V with respect to the platinum reference electrode. However, upon additional testing, we found that reducing the measurement voltage to 0.2 V effectively gets rid of this interference while maintaining a high degree of precision in the glucose measurement. At an intermediate measurement potential of 0.3 V, there is reduced interference from acetaminophen with no drop in glucose currents.

These findings suggest an effective strategy either of reducing the measurement potential to get rid of interference from acetaminophen or of using a mixed-voltage switching measurement regimen if measurements at the standard measurement potential are desired for the higher currents and signal-to-noise ratio. Such a strategy would involve making the bulk of measurements at the higher voltage to maintain a higher degree of precision, with occasional measurements at the reduced voltage to detect interference by acetaminophen. Detection of such interference could result in a temporary switch to the lower measurement potential until the interference is no longer a factor, a warning to the patient, or be used for algorithmic correction.

Such strategies would allow the fabrication of a sensor without the need for additional membranes to filter out acetaminophen as is otherwise suggested [5], reducing fabrication cost and complexity.

For ascorbic acid, we observed a negative effect, where the presence of ascorbic acid was found to reduce the observed current, corresponding to an erroneously low glucose reading if left uncorrected. This suggests the interference is via hydrogen peroxide depletion rather than an direct electrochemical reaction at the electrode. We found the effect to be relatively small (-4.2%, 95% CI:[-6.0%, -2.5%]) at physiological concentrations.

The interference due to ascorbic acid typically occurs due to electrochemical oxidation of ascorbic acid at the electrode. We hypothesize that, in our case, we observe the opposite effect due to oxidation of ascorbic acid by the hydrogen peroxide produced by the glucose oxidase and sensed by the sensor. By reducing part of the generated hydrogen peroxide, ascorbic acid reduces the hydrogen peroxide that ultimately reaches the sensor, lowering sensor current. At the higher hydrogen peroxide concentrations present in the enzyme matrix in our sensors, the ascorbic acid is depleted by reaction with hydrogen peroxide, being unable to reach the electrochemical sensor to cause electrochemical interference.

6.2 Acetaminophen

Introduction

Acetaminophen (N-(4-hydroxyphenyl)acetamide, APAP) undergoes a quasi-reversible redox reaction primarily involving the conversion to N-acetyl-p-benzoquinone imine (NAPQI).

$$APAP \rightarrow NAPQI + 2e^- + 2H^+ \tag{6.1}$$

This is a two-electro two-proton reaction that generally occurs around +0.4 to +0.6V vs. Ag/AgCl at physiological pH. This has been problematic for many commercial glucometers. Oral administration of 1g acetaminophen has been reported [6] to cause glucometer measurements to vary from 85 to 400 mg/dL despite plasma glucose concentrations remaining constant at approximately 90 mg/dL (approximately 5 mM). This interference was measured using FDA-approved commercially available CGM systems from Dexcom and Medtronic, among others. Furthermore, oral administration of acetaminophen has been shown to continue to cause interference for up to eight hours [7].

Strategies to mitigate this interference have included permselective membranes such as in the Decon G6 CGM system. With the permselective membrane, the bias in glucose readings after the third acetaminophen dose of the day is reduced to 14.0 mg/dL [8]. Therapeutic concentrations of acetaminophen are 66-132 μM [9].

We tested acetaminophen interference at a concentration of 200 µM with glucose concentrations of 1mM and 5mM at voltages of 0.2-0.4V.

Methods

Preparations were made of 0mM, 1mM, and 2mM glucose in 1x phosphate-buffered saline. Half of each solution was separated out and spiked with acetaminophen to a concentration of 200 µM. Chronoamperometry was performed with ten sensors, fabricated as described elsewhere in this thesis, at 0.2, 0.3, and 0.4V. Settling current was reached within ten seconds, and the average current in the tenth second of measurement was used as the sensor current at that voltage and concentration. The sensor current was sampled at a rate of 10 measurements per second. To avoid bias due to any temporal variables, each subsequent measurement was in a different solution concentration, chosen at random using a random number generator. Several measurements were taken in each concentration, for a total of 40 measurements. Overall, the sensors behaved similarly to each other and data from an exemplar sensor was analyzed and is presented below.

Results and Analysis

Chronoamperometry Curves

The raw chronoamperometry curves showed a high level of agreement between successive measurements for each concentration, indicating low sensor drift. After the initial transient, the curves for glucose with acetaminophen (dotted) are vertically offset from the curves for glucose (solid), indicating a constant additional signal due to acetaminophen. The offset is largest at 0.4 V, reduced at 0.3 V, and virtually negligible at 0.2 V, at which point the dotted and solid lines merge with each other. The exceptions are the curves with a glucose concentration of 0.0 mM, where the acetaminophen-spiked curves continue to maintain an offset even at a measurement potential of 0.2 V. Each time-current graph shown plots raw unaveraged data from a total of 40 time-current curves overlaid on top of each other.

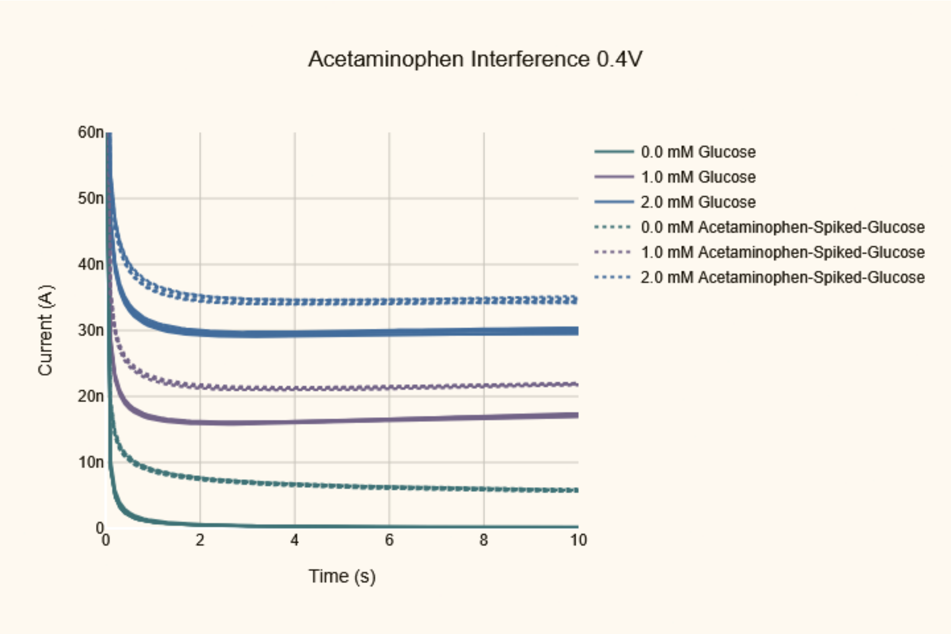

Figure 6.1: Chronoamperometry curves for glucose preparations of 0.0, 1.0, and 2.0mM (solid lines) and the same preparations spiked to an acetaminophen concentration of 200 µM (dotted lines), measured at 0.4 V. n=40 (6-7 per concentration). All 40 curves plotted.

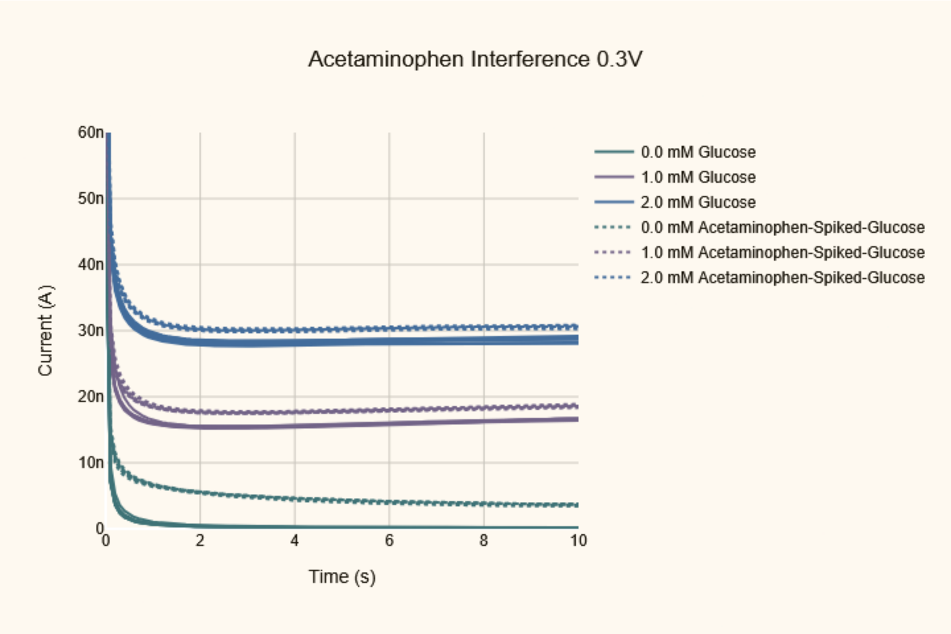

Figure 6.2: Chronoamperometry curves for glucose preparations of 0.0, 1.0, and 2.0mM (solid lines) and the same preparations spiked to an acetaminophen concentration of 200 µM (dotted lines), measured at 0.3 V. n=40 (6-7 per concentration). All 40 curves plotted.

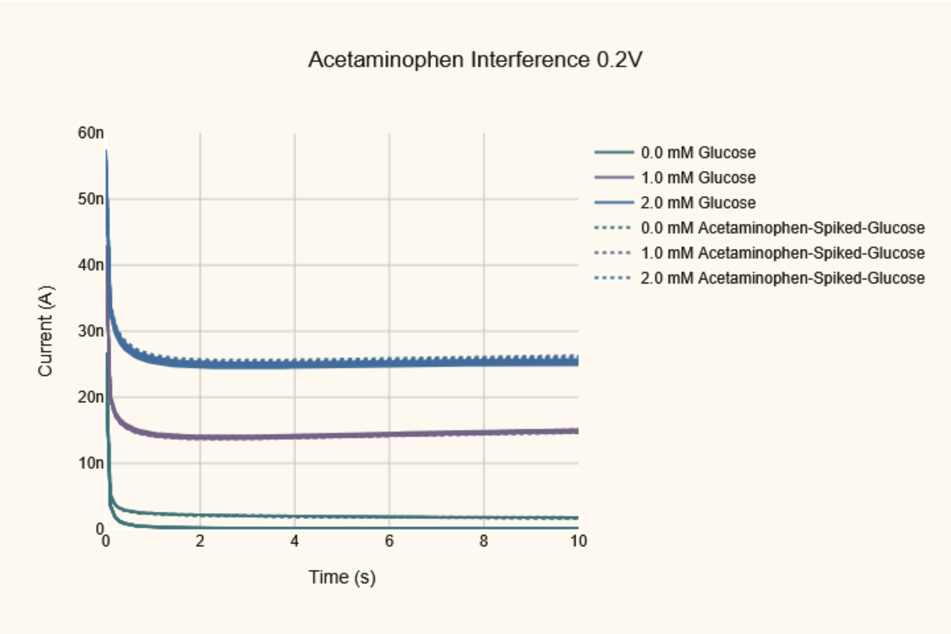

Figure 6.3: Chronoamperometry curves for glucose preparations of 0.0, 1.0, and 2.0mM (solid lines) and the same preparations spiked to an acetaminophen concentration of 200 µM (dotted lines), measured at 0.2 V. n=40 (6-7 per concentration). All 40 curves plotted.

Concentration-Current Curves

The concentration-current curves show a vertical offset between the current with glucose at 1.0 or 2.0 mM (green line) and the current with glucose at those concentration and 200μM acetaminophen (purple line). There is a greater offset in the absence of glucose. The offset is smaller at 0.3 V than at 0.4 V, and virtually gone at 0.2 V (except when glucose is not present).

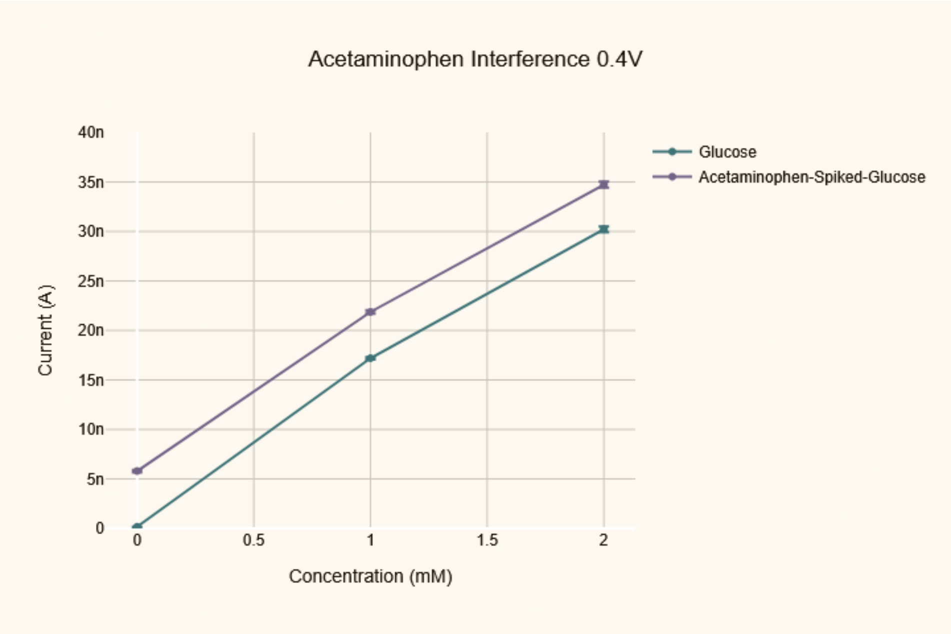

Figure 6.4: Glucose concentration vs. current plots with (green) and without (purple) acetaminophen at 0.4 V. Standard deviation error bars shown. Current is mean current between 9.0 and 10.0 s. Acetaminophen concentration 200μM.

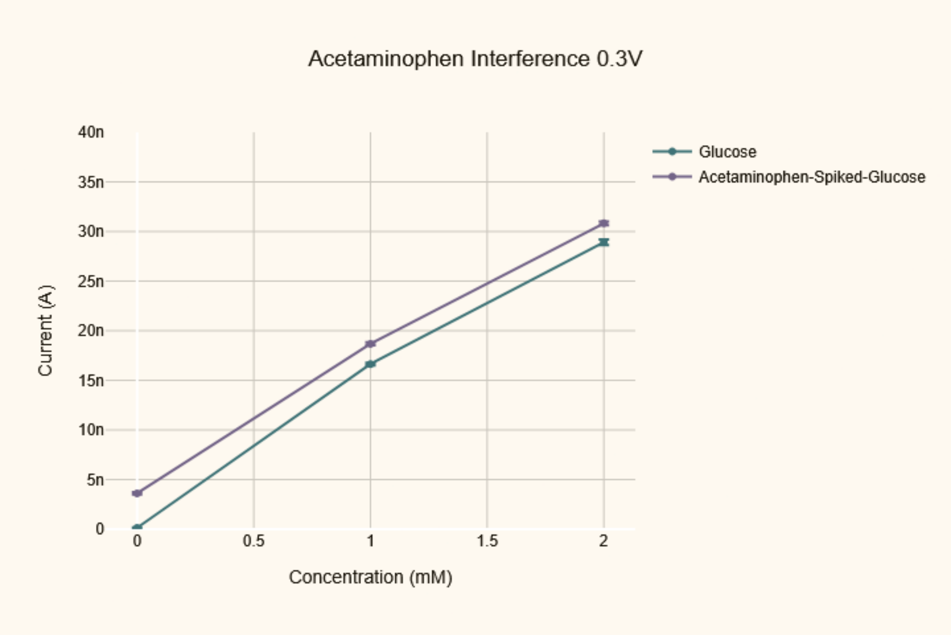

Figure 6.5: Glucose concentration vs. current plots with (green) and without (purple) acetaminophen at 0.4 V. Standard deviation error bars shown. Current is mean current between 9.0 and 10.0 s. Acetaminophen concentration 200μM.

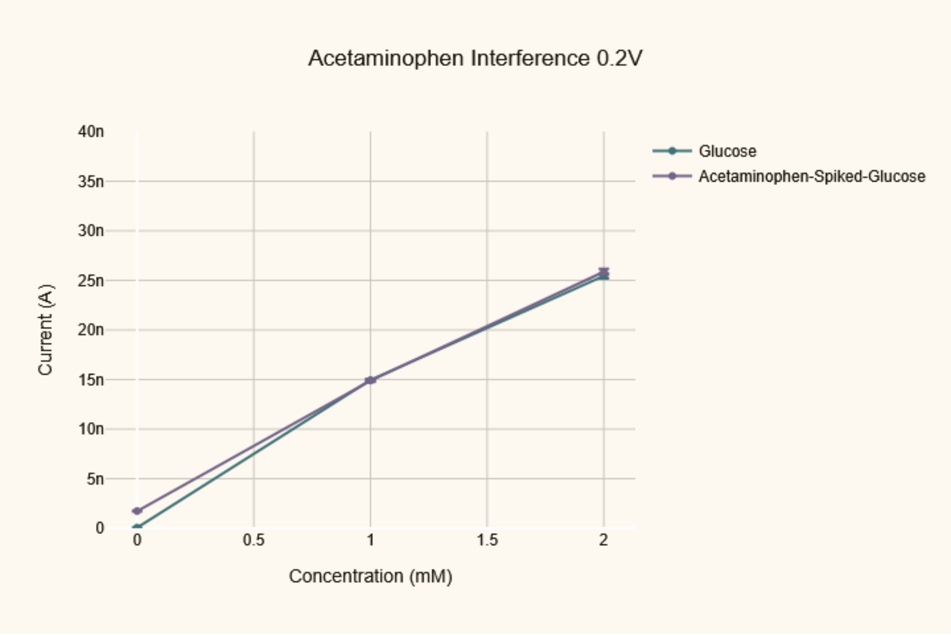

Figure 6.6: Glucose concentration vs. current plots with (green) and without (purple) acetaminophen at 0.4 V. Standard deviation error bars shown. Current is mean current between 9.0 and 10.0 s. Acetaminophen concentration 200μM.

Statistical Summary and Discussion

The tables presented here show a statistical summary of the data measured for this sensor. In the presence of glucose, while interference from acetaminophen is clearly present at a measurement potential of 0.4 V (adding on average 4.5 nA to an average signal of 30.2 nA at 2.0 mM glucose), it is significantly reduced at a measurement potential of 0.3 V without significant reduction in the glucose current signal (adding on average 1.9 nA to an average signal of 28.9 nA at 2.0 mM). At a measurement potential of 0.2 V, there is no statistically significant interference due to acetaminophen and the signal due to glucose, while lower than at 0.4 V, is still high enough for precise measurement. Each sensor tested showed a similar result, with a statistically significant interference current from acetaminophen at 0.3 and 0.4 V but not at 0.2 V.

Glucose Concentration (mM)	Mean Current (nA)	Mean Additional Current with Acetaminophen (nA)	95% Confidence Interval (nA)
0.0	0.2	5.6	5.5 - 5.7
1.0	17.2	4.7	4.5 - 4.9
2.0	30.2	4.5	4.1 - 4.9

Table 6.1: Acetaminophen interference at 0.4V

Glucose Concentration (mM)	Mean Current (nA)	Mean Additional Current with Acetaminophen (nA)	95% Confidence Interval (nA)
0.0	0.1	3.5	3.3 - 3.6
1.0	16.6	2.0	1.8 - 2.2
2.0	28.9	1.9	1.6 - 2.2

Table 6.2: Acetaminophen interference at 0.3 V

Glucose Concentration (mM)	Mean Current (nA)	Mean Additional Current with Acetaminophen (nA)	95% Confidence Interval (nA)
0.0	0.0	1.7	1.6 - 1.7
1.0	14.9	-0.1*	-0.2 - 0.0
2.0	25.9	0.2*	0.0 - 0.4

Table 6.3: Acetaminophen interference at 0.2 V. Numbers marked with * are statistically insignificant.

In the absence of glucose, a signal due to acetaminophen is detectable even when we reduce the voltage to 0.2 V. We believe this is due to instability of the platinum reference electrode in the absence of hydrogen peroxide, causing the true electrochemical potential at the working and counter electrodes to vary from their values when the reference electrode is stable. This is not too concerning because, while realizable in vitro, the complete absence of glucose is unlikely to be encountered in vivo in an alive patient.

6.3 Ascorbic Acid

Introduction

Ascorbic acid (vitamin C) is another source of potential interference with continuous glucose monitors. Vitamin C is among the most commonly used antioxidant dietary supplements and can cause both overestimation and underestimation of glucose levels. Vitamin C is a strong reducing agent which can be oxidized at the electrode surface of electrochemical glucometers, adding to the total signal generated, which is interpreted as falsely high glucose readings. This mechanism has been reported [10] to cause false indications of hyperglycemia in patients undergoing Vitamin C therapy with Abbott Precision Xceed Pro and Roche Inform II glucometers whereas the Nova StatStrip was reported to detect the ascorbic acid present and display an error message instead.

Meanwhile, pseudohypoglycemia indications have been reported with glucose oxidase based laboratory assays [11] as well as in peroxidase-based assays [12], where peroxide depletion is considered to be the main mechanism of interference. Due to the principle of operation of our sensors, we are potentially susceptible to either mechanism of interference, depending on whether ascorbate or hydrogen peroxide are present in excess in the immobilized glucose oxidase layer.

The assumed optimal plasma concentration of Vitamin C is 50 µM [13]. We tested interference at a concentration of 60 µM and found that in this concentration range, we are susceptible to a small reduction (≈ 4.2%) in sensor current and underestimation of glucose level. Due to this being an underestimation, we conclude that the chemical interference pathway must be the dominant one at this concentration range.

Being chemical rather than electrochemical in nature, this interference is not amenable to mitigation by strategies similar to those shared for acetaminophen above and we present this information here for consideration in the overall design process of any final product proceeding on the basis of this technology. However, since the effect size is small at physiological concentrations, there may be limited benefit from increasing device complexity to reduce ascorbic acid interference.

Methods

A preparation was made of 1.0 mM glucose in phosphate buffered saline. This was divided into two equal volumes, one of which was spiked with ascorbic acid to a final concentration of 60 µM. Nine sensors were tested five times each in both the neat and spiked solutions, for a total of 45 measurements per solution. The currents with and without ascorbic acid were compared to each other to determine the interference caused by ascorbic acid.

Results and Analysis

Sensor ID	Mean current Glucose (nA)	Standard error Glucose (nA)	Mean current AA + Glucose (nA)	Standard error AA + Glucose (nA)
A	39.1	2.1	37.8	1.6
B	26.0	1.2	24.7	0.5
C	34.5	2.4	33.1	1.3
D	35.7	1.8	33.4	0.8
E	38.5	2.5	36.9	1.2
F	28.9	1.7	28.0	0.9
G	42.9	2.6	41.4	1.4
H	30.9	1.6	30.0	0.6
I	32.1	1.8	30.2	1.3

Table 6.4: Currents recorded for glucose with and without ascorbic acid. "Glucose" values are for 1.0 mM glucose and "AA + Glucose" values are for 1.0 mM glucose with 60μM ascorbic acid.

The sensors used for this analysis had high drift resulting in high standard error (2.6 nA in the worst case), and the effect size of ascorbic acid interference was small, so results were aggregated across all sensors to make a statistically justified conclusion. Each sensor's currents were normalized to its sensitivity (measured by its mean current with 1.0 mM glucose) and the percentage change caused by ascorbic acid doping was used. On average, the ascorbic acid reduced the measured current by 4.2% (95% CI: [-6.0%, -2.5%]).

Due to this being a net reduction in measured signal, we conclude the interference must predominantly be via the route of depletion of hydrogen peroxide rather than the route of direct reaction at the electrode.

References

[1] Raja Ram Pandey et al. "Electrochemical Detection of Acetaminophen with Silicon Nanowires". In: *Electroanalysis* 30.5 (2018). ISSN: 1040-0397. PMID: `32999580`.

[2] Afef Dhaffouli et al. "Electrochemical Detection of Paracetamol in Real Samples Using Sensor Based on a Glassy Carbon Electrode Modified with Chitosan@SiO2-APTES Composite: Synthesis, Characterization and Analytical Applications". In: *Journal of The Electrochemical Society* 172.1 (Jan. 2025), p. 017521. ISSN: 1945-7111. DOI: `10.1149/1945-7111/ada97d`.

[3] Asmamaw Taye and Assefa Sergawie. "Determination of Ascorbic Acid Content of Wine & Soft Drinks by Voltammetric Techniques at Glassy Carbon Electrode". In: *JSM Chemistry* 7.1 (1 Jan. 21, 2019), pp. 1–11. ISSN: 2334-1831. DOI: `10.47739/1054`.

[4] S. P. Perone and W. J. Kretlow. "Application of Controlled Potential Techniques to Study of Rapid Succeeding Chemical Reaction Coupled to Electro-Oxidation of Ascorbic Acid". In: *Analytical Chemistry* 38.12 (Nov. 1, 1966), pp. 1760–1763. ISSN: 0003-2700. DOI: `10.1021/ac60244a034`.

[5] D. Moatti-Sirat et al. "Reduction of Acetaminophen Interference in Glucose Sensors by a Composite Nafion Membrane: Demonstration in Rats and Man". In: *Diabetologia* 37.6 (June 1, 1994), pp. 610–616. ISSN: 1432-0428. DOI: `10.1007/BF00403381`.

[6] Ananda Basu et al. "Direct Evidence of Acetaminophen Interference with Subcutaneous Glucose Sensing in Humans: A Pilot Study". In: *Diabetes Technology & Therapeutics* 18 Suppl 2 (Suppl 2 Feb. 2016), S243–247. ISSN: 1557-8593. DOI: `10.1089/dia.2015.0410`. PMID: `26784129`.

[7] David M. Maahs et al. "Effect of Acetaminophen on CGM Glucose in an Outpatient Setting". In: *Diabetes Care* 38.10 (Oct. 2015), e158–e159. ISSN: 0149-5992. DOI: `10.2337/dc15-1096`. PMID: `26269199`.

[8] Douglas Denham. “Effect of Repeated Doses of Acetaminophen on a Continuous Glucose Monitoring System with Permselective Membrane”. In: *Journal of Diabetes Science and Technology* 15.2 (Mar. 2021), pp. 517–518. ISSN: 1932-2968. DOI: `10.1177/1932296820948544`. PMID: `32865043`.

[9] D. H. Beck et al. “The Pharmacokinetics and Analgesic Efficacy of Larger Dose Rectal Acetaminophen (40 Mg/Kg) in Adults: A Double-Blinded, Randomized Study”. In: *Anesthesia and Analgesia* 90.2 (Feb. 2000), pp. 431–436. ISSN: 0003-2999. DOI: `10.1097/00000539-200002000-00035`. PMID: `10648334`.

[10] Brooke M. Katzman et al. “Unintended Consequence of High-Dose Vitamin C Therapy for an Oncology Patient: Evaluation of Ascorbic Acid Interference With Three Hospital-Use Glucose Meters”. In: *Journal of Diabetes Science and Technology* 15.4 (July 2021), pp. 897–900. ISSN: 1932-2968. DOI: `10.1177/1932296820932186`. PMID: `32506941`.

[11] Javaughn Corey R Gray. “Pseudohypoglycemia in a Patient on High Dose Intravenous Ascorbate for Metastatic Castration-Resistant Prostate Cancer”. In: 4.1 (2021).

[12] Flávia Martinello and Edson Luiz da Silva. “Mechanism of Ascorbic Acid Interference in Biochemical Tests That Use Peroxide and Peroxidase to Generate Chromophore”. In: *Clinica Chimica Acta; International Journal of Clinical Chemistry* 373.1–2 (Nov. 2006), pp. 108–116. ISSN: 0009-8981. DOI: `10.1016/j.cca.2006.05.012`. PMID: `16806141`.

[13] D. Brubacher, U. Moser, and P. Jordan. “Vitamin C Concentrations in Plasma as a Function of Intake: A Meta-Analysis”. In: *International Journal for Vitamin and Nutrition Research. Internationale Zeitschrift Fur Vitamin- Und Ernahrungsforschung. Journal International De Vitaminologie Et De Nutrition* 70.5 (Sept. 2000), pp. 226–237. ISSN: 0300-9831. DOI: `10.1024/0300-9831.70.5.226`. PMID: `11068703`.

Appendix A

IMPEDANCE SPECTRA

Impedance spectra for nine sensors with spin-coated and lithographically patterned enzyme. Impedance data were collected at the Molecular Materials Research Center in the Beckman Institute of the California Institute of Technology and fit using ZView software to the circuit model in Figure A.1. Fit results are shown in table A.1.

Figure A.1: The circuit model fit to impedance spectrum data. CPE indicates a Constant Phase Element.

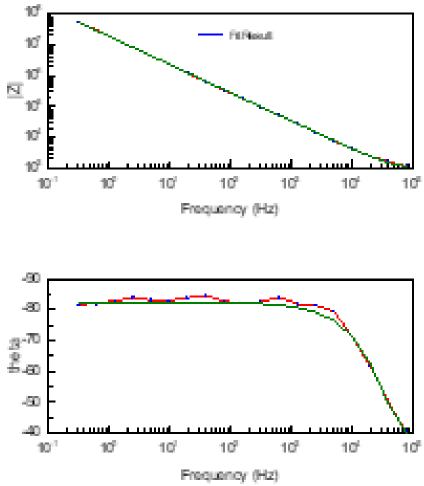

Figure A.2: Example of impedance spectrum collected.

Sensor	Element	Value	Error	Error %
A	R	830.9	25.815	3.1069
	CPE-T	9.70E-09	1.39E-10	1.4334
	CPE-P	0.91643	0.0019282	0.2104
B	R	1854	107.15	5.7794
	CPE-T	1.81E-08	3.19E-09	17.69
	CPE-P	0.91544	0.01989	2.1727
C	R	965.2	60.661	6.2848
	CPE-T	1.04E-08	1.36E-09	13.023
	CPE-P	0.91714	0.013622	1.4853
D	R	1650	82.984	5.0293
	CPE-T	5.41E-09	6.16E-10	11.395
	CPE-P	0.94106	0.011975	1.2725
E	R	1593	80.128	5.03
	CPE-T	5.37E-09	5.74E-10	10.686
	CPE-P	0.93019	0.011141	1.1977
F	R	967.4	40.559	4.1926
	CPE-T	3.20E-08	2.87E-09	8.9714
	CPE-P	0.84121	0.0095478	1.135
G	R	1525	73.942	4.8487
	CPE-T	6.69E-09	7.14E-10	10.679
	CPE-P	0.92474	0.011199	1.211
H	R	1040	38.443	3.6964
	CPE-T	7.73E-09	6.35E-10	8.2171
	CPE-P	0.94294	0.0085715	0.90902
I	R	1525	67.389	4.419
	CPE-T	7.35E-09	7.24E-10	9..8411
	CPE-P	0.91772	0.010337	1.1264

Table A.1: Values fit for imedance spectra for 9 sensors

Appendix B

EXAMPLE SIMULATION INPUT FILE

This appendix shows an example input file to use for using the FEA simulation. While the input files used for the simulations in this work typically comprised of multiple files, each representing a related group of dynamics, a combined input file is shown here for easier illustration. The Mesh file used must define the enzyme and solution subdomains, the interface boundary, the external ('extended') boundaries, and the inactive sensor surface.

```
# MESH

MESH_FILE = '/path/to/mesh.e'

# OUTPUT

OUTPUT_FILE_BASE = '/path/to/output_file'

# PARTITION AND HINDERED DIFFUSION

ALPHA_PARTITION = 0.9                # Dimensionless
GLUCOSE_BETA = 0.06                  # Dimensionless
SMALLMOLECULE_BETA = 0.2             # Dimensionless

# ENZYME KINETICS

RMAX = 100                           # mM/s
GLUCOSE_KM = 71                      # mM
OXYGEN_KM = 0.85                     # mM

# CONCENTRATIONS

GLUCOSE_CONC = 1                     # mM
OXYGEN_CONC = 0.26                   # mM
```

```
PEROXIDE_CONC = 0                    # mM

# TIME

SENSOR_ON_TIME = 30.0                # s
MEASUREMENT_DURATION = 20.0          # s

# FREE DIFFUSIVITY

GLUCOSE_FREE_DIFFUSIVITY = 720       # um^2/s
OXYGEN_FREE_DIFFUSIVITY = 1930       # um^2/s
PEROXIDE_FREE_DIFFUSIVITY = 1430     # um^2/s

# CALCULATED

GLUCOSE_ENZYME_DIFFUSIVITY  = ${fparse
                                GLUCOSE_BETA
                              * GLUCOSE_FREE_DIFFUSIVITY}
                                (# um^2/s)

OXYGEN_ENZYME_DIFFUSIVITY   = ${fparse
                                SMALLMOLECULE_BETA
                              * OXYGEN_FREE_DIFFUSIVITY}
                                (# um^2/s)

PEROXIDE_ENZYME_DIFFUSIVITY = ${fparse SMALLMOLECULE_BETA
                              * PEROXIDE_FREE_DIFFUSIVITY}
                                (# um^2/s)

END_TIME = ${fparse SENSOR_ON_TIME + MEASUREMENT_DURATION}  # s

[Problem]
    type = FEProblem
[]

[Variables]
```

```
    [glucose_e]
        block = 'enzyme'
    []

    [oxygen_e]
        block = 'enzyme'
    []

    [peroxide_e]
        block = 'enzyme'
    []

    [glucose_s]
        block = 'solution'
    []

    [oxygen_s]
        block = 'solution'
    []

    [peroxide_s]
        block = 'solution'
    []
[]

[Kernels]
    [glucose_diffusion_e]
        type = ADMatDiffusion
        variable = 'glucose_e'
        block = 'enzyme'

        diffusivity = ${GLUCOSE_ENZYME_DIFFUSIVITY}
    []

    [oxygen_diffusion_e]
        type = ADMatDiffusion
```

```
    variable = 'oxygen_e'
    block = 'enzyme'

    diffusivity = ${OXYGEN_ENZYME_DIFFUSIVITY}
[]

[peroxide_diffusion_e]
    type = ADMatDiffusion
    variable = 'peroxide_e'
    block = 'enzyme'

    diffusivity = ${PEROXIDE_ENZYME_DIFFUSIVITY}
[]

[glucose_diffusion_s]
    type = ADMatDiffusion
    variable = 'glucose_s'
    block = 'solution'

    diffusivity = ${GLUCOSE_FREE_DIFFUSIVITY}
[]

[oxygen_diffusion_s]
    type = ADMatDiffusion
    variable = 'oxygen_s'
    block = 'solution'

    diffusivity = ${OXYGEN_FREE_DIFFUSIVITY}
[]

[peroxide_diffusion_s]
    type = ADMatDiffusion
    variable = 'peroxide_s'
    block = 'solution'

    diffusivity = ${PEROXIDE_FREE_DIFFUSIVITY}
```

```
[]

[glucose_reaction]
    type = TwoSubstrate
    block = 'enzyme'
    variable = 'glucose_e'

    variable_coupled = 'oxygen_e'
    r_max = ${RMAX}
    k_m = ${GLUCOSE_KM}
    k_m_coupled = ${OXYGEN_KM}
[]

[oxygen_reaction]
    type = TwoSubstrate
    block = 'enzyme'
    variable = 'oxygen_e'

    variable_coupled = 'glucose_e'
    r_max = ${RMAX}
    k_m = ${OXYGEN_KM}
    k_m_coupled = ${GLUCOSE_KM}
[]

[peroxide_reaction]
    type = TwoSubstrateProduct
    block = 'enzyme'
    variable = 'peroxide_e'

    variable_coupled_1 = 'glucose_e'
    variable_coupled_2 = 'oxygen_e'
    r_max = ${fparse -RMAX}
    k_m_coupled_1 = ${GLUCOSE_KM}
    k_m_coupled_2 = ${OXYGEN_KM}
[]
```

```
    [glucose_timederivative_e]
        type = ADTimeDerivative
        block = 'enzyme'
        variable = 'glucose_e'
    []

    [oxygen_timederivative_e]
        type = ADTimeDerivative
        block = 'enzyme'
        variable = 'oxygen_e'
    []

    [peroxide_timederitative_e]
        type = ADTimeDerivative
        block = 'enzyme'
        variable = 'peroxide_e'
    []

    [glucose_timederivative_s]
        type = ADTimeDerivative
        variable = 'glucose_s'
        block = 'solution'
    []

    [oxygen_timederivative_s]
        type = ADTimeDerivative
        variable = 'oxygen_s'
        block = 'solution'
    []

    [peroxide_timederitative_s]
        type = ADTimeDerivative
        variable = 'peroxide_s'
        block = 'solution'
    []
[]
```

```
[InterfaceKernels]
    [glucose_interface_kernel]
        type = InterfaceDiffusion
        variable = 'glucose_s'
        neighbor_var = 'glucose_e'
        boundary = 'interface'

        D = ${GLUCOSE_FREE_DIFFUSIVITY}
        D_neighbor = ${GLUCOSE_ENZYME_DIFFUSIVITY}
    []

    [oxygen_interface_kernel]
        type = InterfaceDiffusion
        variable = 'oxygen_s'
        neighbor_var = 'oxygen_e'

        boundary = 'interface'
        D = ${OXYGEN_FREE_DIFFUSIVITY}
        D_neighbor = ${OXYGEN_ENZYME_DIFFUSIVITY}
    []

    [peroxide_interface_kernel]
        type = InterfaceDiffusion
        variable = 'peroxide_s'
        neighbor_var = 'peroxide_e'

        boundary = 'interface'
        D = ${PEROXIDE_FREE_DIFFUSIVITY}
        D_neighbor = ${PEROXIDE_ENZYME_DIFFUSIVITY}
    []
[]

[BCs]
    [glucose_interface_bc]
        type = ADMatchedValueBC
```

```
    variable = 'glucose_s'
    v = 'glucose_e'
    boundary = 'interface'

    u_coeff = ${ALPHA_PARTITION}
[]

[oxygen_interface_bc]
    type = ADMatchedValueBC
    variable = 'oxygen_s'
    v = 'oxygen_e'
    boundary = 'interface'

    u_coeff = ${ALPHA_PARTITION}
[]

[peroxide_interface_bc]
    type = ADMatchedValueBC
    variable = 'peroxide_s'
    v = 'peroxide_e'
    boundary = 'interface'

    u_coeff = ${ALPHA_PARTITION}
[]

[extended_noflux_glucose]
    type = ADNeumannBC
    variable = 'glucose_s'
    boundary = 'extended'
    value = 0
[]

[extended_noflux_oxygen]
    type = ADNeumannBC
    variable = 'oxygen_s'
    boundary = 'extended'
```

```
    value = 0
[]

[extended_noflux_peroxide]
    type = ADNeumannBC
    variable = 'peroxide_s'
    boundary = 'extended'
    value = 0
[]

[inactive_noflux_glucose]
    type = ADNeumannBC
    variable = 'glucose_s'
    boundary = 'inactive'
    value = 0
[]

[inactive_noflux_oxygen]
    type = ADNeumannBC
    variable = 'oxygen_s'
    boundary = 'inactive'
    value = 0
[]

[inactive_noflux_peroxide]
    type = ADNeumannBC
    variable = 'peroxide_s'
    boundary = 'inactive'
    value = 0
[]

[peroxide_consumption]
    type = ADDirichletBC
    variable = 'peroxide_e'
    boundary = 'sensor'
    value = 0
```

```
    []

    [oxygen_recycling]
        type = ADCoupledFluxBC
        variable = 'oxygen_e'
        boundary = 'sensor'
        coupled_variable = 'peroxide_e'
        alpha = -${PEROXIDE_ENZYME_DIFFUSIVITY}
    []
[]

[ICs]
    [glucose_initial_s]
        type = ConstantIC
        variable = 'glucose_s'

        block = 'solution'
        value = ${GLUCOSE_CONC}
    []

    [oxygen_initial_s]
        type =  ConstantIC
        variable = 'oxygen_s'

        block = 'solution'
        value = ${OXYGEN_CONC}
    []

    [peroxide_initial_s]
        type =  ConstantIC
        variable = 'peroxide_s'

        block = 'solution'
        value = ${PEROXIDE_CONC}
    []
```

```
    [glucose_initial_e]
        type = ConstantIC
        variable = 'glucose_e'

        block = 'enzyme'
        value = 0
    []

    [oxygen_initial_e]
        type =  ConstantIC
        variable = 'oxygen_e'

        block = 'enzyme'
        value = 0
    []

    [peroxide_initial_e]
        type =  ConstantIC
        variable = 'peroxide_e'

        block = 'enzyme'
        value = 0
    []
[]

[Controls]
    [sensor_on]
        type = TimePeriod
        start_time = ${SENSOR_ON_TIME}
        enable_objects = 'BCs/peroxide_consumption BCs/oxygen_recycling'
    []
[]

[Functions]
    [max_timestep]
        type = PiecewiseConstant
```

```
        xy_data = '0.0                              1.0
                   ${fparse SENSOR_ON_TIME - 1.0}   0.05'
    []
[]

[Executioner]
    type = Transient
    solve_type = NEWTON
    line_search = 'none'

    l_max_its = 30
    nl_max_its = 10

    l_tol = 1.0e-5
    nl_rel_tol = 1.0e-5

    start_time = 0.0
    end_time = ${END_TIME}
    steady_state_detection = true
    steady_state_start_time = ${fparse SENSOR_ON_TIME + 5.0}

    automatic_scaling = true

    [TimeSteppers]
        [function]
            type = FunctionDT
            function = max_timestep
        []

        [adaptive]
            type = IterationAdaptiveDT
            dt = 0.1
            cutback_factor = 0.8
            growth_factor = 1.5
            optimal_iterations = 7
        []
```

```
    []
[]

[Postprocessors]
    [oxygen_generation]
        type = ADSideDiffusiveFluxIntegral
        boundary = sensor
        variable = 'oxygen_e'

        diffusivity = ${OXYGEN_ENZYME_DIFFUSIVITY}
        execute_on = NONLINEAR_CONVERGENCE
    []

    [peroxide_consumption]
        type = ADSideDiffusiveFluxIntegral
        boundary = sensor
        variable = 'peroxide_e'

        diffusivity = ${PEROXIDE_ENZYME_DIFFUSIVITY}
        execute_on = NONLINEAR_CONVERGENCE
    []
[]

[Mesh]
  type = FileMesh
  file = ${MESH_FILE}
  coord_type = 'RZ'
[]

[Outputs]
    [exodus]
        type = Exodus
        file_base = ${OUTPUT_FILE_BASE}
    []

    [csv]
```

```
        type = CSV
        file_base = ${OUTPUT_FILE_BASE}

    []

    [console]
        type = Console
        execute_on = 'FINAL'
        enable = false
    []
[]
```